Modelling of a Solar Stove: Small Scale Concentrating System With Heat Storage

(Potential For Cooking In Rural Areas, Zimbabwe)

Actor Chikukwa

Doctoral thesis in partial fulfillment of the Dr Scientiarium degree.

Trondheim, October 2007

Norwegian University of Science and Technology
Faculty of Natural Sciences and Technology
Department of Physics

NTNU

Dedication:

This humble research is dedicated to my godparents: Bente and Per Solberg

Acknowledgements

Firstly, I would like to express my heart-felt and most profound gratitudes to my Supervisor, Professor Jørgen Løvseth, for his priceless support (across the spectrum) and indispensable guidance throughout the course of this work. His vast and in-depth experience in Solar Energy, Heat Transfer and Computer Programming has been a unique resource which I couldn't do without. Discussions with him always left me refreshed with new energy and inspiration to put into further work. I have no complaint whatsoever. May God Bless you!

Secondly, to the co-supervisor Professor Berit Kjeldstad: You have always been there for me when I needed you. Sincerely, I don't remember coming out of your office without a broad smile. I am forever thankful.

To my godparents, Per and Bente Solberg: It is a matter of fact that I wouldn't have come this far without your love and support. Words simply fall short to express the degree of my gratitudes to both of you. You have been my backbone in everything across the board. I dedicate this humble research to your honor, please accept it; only then can my happiness in regards to this work be fulfilled!

To Eli Snekkvik and Torbjrn Hallan: I don't see how I could have lived in Trondheim without your support in many ways. *Gogo* Eli, the countless hours you have spent baby-sitting Lille-Per on my behalf will never be forgotten. Sincerely, the two of you have been a special blessing to my family.

This work would not have been possible without financial support from The Norwegian Research Council's Quota Programme. My sincere thanks especially to Ragnhild Brakstad, the coordinator, for all her administrative support throughout. Mam, you did your best to see me through. Thank you. Valuable gains from interacting with my colleagues in the department, especially Binod Bhattarai on PCTex and MATLAB cannot go unmentioned. To all colleages I say: thanks for everything. Also, last minute contributions from my friends: Denis Okello and Drani Nyeinga, were very useful. Thank you guys.

Special thanks to my dear wife Pauline for her love, patience and encouragement over the years. It couldn't be any better *mai mwana*! Also, to my son Lille-Per (Ebenezer), though still a toddler, your ever-cheerful mood has been a great source of inspiration. And to my distinguished right-hand-person: Mainini-Pure, thanks for being there and ready-to-go when ever I needed your input.

Finally, I am so thankful to my mother for all her support and love. She gave me a dream when I was young, and then did her best to nurture its realization. Today, I am happy to be holding part of that dream. What else can one ask from a mother?

Thesis Outline

The central objective of the present research is to serve as an in-depth technical introduction to small-scale concentrating systems tailored for application especially in rural areas in Africa located outside the national electricity grids. For example, MSc- and doctoral-students recently matriculated on NUFU-sponsership at some universities in Africa (i.e Mozambique, Uganda, Tanzania, South Africa and Ethiopia) for research in solar-concentrator technologies will find most of the material in this work quite useful.

Therefore, it has been deemed convenient to write the present thesis in monographic form, and it consists of a total of 7 chapters. The gist of the discussions in individual chapters is centered around an important aspect or component of the concentrating system. The general flow of ideas then traces solar energy from its availability, to how it could be harnessed by means of a specially designed solar-oven with heat storage, to meet (fundamental) domestic high-temperature-heat needs, i.e mainly cooking, boiling and heating.

Chapter 1 discusses the premise on which this research is based. It essentially highlights the gravity of the energy crisis as experienced by the impoverished masses living in most parts of Africa. The situation in Zimbabwe was discussed in detail (for case-studies[1]) because it is a suitable example added to the convenience of being the country of the author's origin.

The second chapter is thus a detailed study on the solar energy resource situation in Zimbabwe. It describes the availability and patterns of solar energy based on the existing solar radiation data obtained from meteorological stations scattered throughout the country. These results were necessary for assessing the potential of the proposed system in Zimbabwe, and can also be extended for use in other solar energy projects.

[1]The situation in Zimbabwe in terms of: the scarcity of wood-fuel, deforestation problems, the standard and way of life in rural communities etc, can be regarded as moderately representative of the prevalent situation in most countries in Southern Africa.

Chapter 3 focuses on the collection of solar radiation using parabolic concentrators. Major determinants that include errors and optical sensitivity of parabolic solar collectors, the correlation between receiver configuration and the parabolic collector are expounded. Arguments for and the main principle on how-to incorporate a mechanical solar tracking device are also laid-out in this part of the thesis.

A very critical component of the concentrating system: the volumetric fibrous receiver, is described in the 4th chapter. Here, the theory on which one of the major computer programmes developed in this research, is given an in-depth treatment. The gist of this programme is to simulate the heat transfer mechanisms taking place within the fibrous receiver during operation. The predicted results are then presented and discussed in detail.

The transportation of the hot air from the receiver, the ceding of its sensible energy to rockbed thermal storage and insulation are deliberated in chapter 5. Another major computer programme that models these processes is written, in which case, results for different inputs are discussed and compared. The need to devise an air-pump capable of adjusting the mass flow rate in order to sustain a constant inlet air temperature to the storage is highlighted.

Chapter 6 describes the design of the hotplates and their incorporation to the storage unit. The premise on which the third major computer model in this work is discussed in detail. This simulation programme attempts to model a cooking process, in which case, the thermal storage is simultaneously discharged. The results are presented and an overview of the merits of a successful system are briefly discussed .

Finally, major conclusions, recommendations and areas for further study are given in chapter 7.

Contents

Chapter 1

General Introduction

1.1 Background

The sun's energy, in its different forms, either direct or indirect (e.g wind and biomass), was the main energy source that inspired and facilitated the development of human societies until the discovery of fossil fuels which marked the beginning of the industrial revolution. Since then, an energy infrastructure that now covers practically the entire globe, has been built. It is largely based on fossil fuels and to a lesser extent on the remaining alternatives. Today, the world consumes an estimated average of 9 G*toe*[1] per year. While fossil fuel helps us live more comfortably than past generations, its use inevitably incurs the risk of irreversibly altering our planet's natural balances, both locally and globally.

The world's population has been growing rapidly over the last century and continues to grow, an estimated 1.6 billion in 1900, which has of late gone past 6 billion [1]. If this trend continues, a staggering 9 billion human population is expected by 2050. On the other hand, our increasingly crowded world has also become a world of cities, in which case, approximately 50% of the population is understood be living in cities already. This fraction is steadily (but surely) rising, and expected to be to the order of 75% by the year 2050, as is evidenced by the increase of the number of cities across the world that is populated in excess of 10 million people.

Though a lamentable reality, the dramatic contrast between wealth and poverty has become part of this modern world. There is excessive energy consumption among the richer segments while scarcity characterizes the poorer segments. Failure to meet the most basic needs: decent homes, clean water, health care, education, etc; is pro-

[1]The *toe* is a unit of energy used in the international energy industry. 1 toe represents the energy available from burning one tonne (metric ton) of oil or 1.4 tonnes of coal. 1 toe is also equivalent to 41.868 GJ

found in the Third World, especially Africa, South America and parts of Asia. If these legitimate and ever-growing needs are to be met, energy consumption must surely increase in order to mitigate the severity of abject poverty in the remote, and usually neglected parts of the world [2].

Most of the countries in the world now include renewable energy resources as part of their strategy for clean and sustainable energy supplies for the future. In any case, the development of new technologies that can harness energy resources in a practical and cost-effective way, essentially require an assessment of the availability and limitations of the sources [3, 4].

With the progress of industrialization, the development of new technologies, the discovery of new fossil fuels (coal has been used since ancient times) and eventually nuclear power, the role of wood as a source of energy started to decrease only a few centuries ago [5] in developed countries. Today, solar sources provide around 10% of the energy used worldwide, but that share is still much higher in developing countries.

The fossil sources cannot cope with demand, which is in part, due to increased use in the Third World. Resultantly, the sustainability of the world's energy supplies by means of fossil fuels is arguably doubtful beyond 2050, if not much earlier. However, the sun with an estimated 5 billion more years according to astrophysists [6], can be considered as an inexhaustible energy source from the human perspective. All the same, the main question is: Can technological developments and the transition to a culture that is more aware of the need to safeguard the environment help us create a world largely powered by 'green' energy?

1.2 Availability of Solar Power and Current Technologies

1.2.1 General

Solar energy exists everywhere, but has stronger concentration in some parts of the world compared to others. As such, some regions receive high insolation and will thus produce higher amounts of energy from a specific collector field size. Nevertheless, solar energy is available over the entire globe, and one could argue that only the size of the collector field is what matters. Hence, it is up to the engineer to determine the feasibility of any solar-based project depending on the amount, quality and timing of the solar energy available at the chosen site. However in practice, quite a number of factors, other than the size of the collector-field are considered in order to evaluate

the feasibility of any such undertakings.

The flow of renewable solar energies on earth is essentially a direct function of the solar radiation flux. Every year, the sun irradiates the earth's land masses with an equivalent of 19×10^3 Gtoe. Just a tiny fraction (0.00047) of this quantity, estimated to be around 9 Gtoe per year, could satisfy the world's energy requirements [7, 8].

To date, there a is varied number of technologies that have been developed to exploit solar energy. Solar power can be used in both large- and small-scale applications, with smaller systems best suited for off-the-grid power supplies. The sun, as an energy resource, has the potential to mitigate growing energy needs, provide diversity and reliability in energy supplies for regions within the Sunbelt. The technology include: concentrating solar power (CSP) systems, passive solar heating and daylighting, photovoltaic systems, solar hot water, solar process heat, space heating and cooling, etc. Some selected systems, which are considered to have relevance to the present work, are briefly discussed in the next sections.

1.2.2 Electricity Generation

Concentrating Solar Power (CSP) Technologies

It appears little research and development capacity[2] have been given to advanced solar thermal systems, although these seem to hold better prospects for the energy industry and homes in the majority of the countries with high insolation. Even though maximum efficiencies achieved so far are only to the order of 30%, CSP systems allow power plants to produce electricity from the sun on a larger scale, which in turn allows consumers to take advantage of solar power without making the investment in personal solar technology systems. Based on advancements in the technology, CSP systems are expected to provide energy at costs comparable (in the next decade or two) to that obtained by conventional technologies, see figure 1.1.

There are three main types of concentrating solar power systems: parabolic-trough, parabolic dish collector, and power tower; all of which can be applied to generate electricity. Reference is given to [10] for detailed descriptions. The National Renewable Energy Laboratory (NREL), estimates that by the year 2015 [11], electricity from solar thermal stations could be competitive enough to substitute conventional technology in at least some parts of the USA and or other parts of the world where the technology is applicable. To mention just but a few, examples of CSP major projects include: stirling engines, the solar field in the Mojave desert, the Almeria solar tower in Spain and Solar-II in California [12, 13].

[2]Especially in the developing economies.

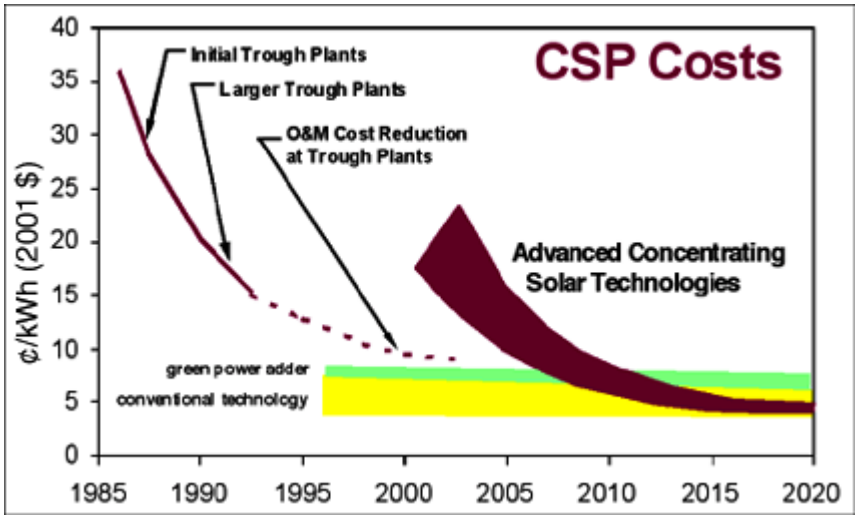

Figure 1.1: Advancements in the technology and the use of low-cost thermal storage will allow concentrating solar power plants to operate for more hours during the day and shift solar power generation to evening hours. This is expected to reduce energy costs significantly as shown. Adapted from [11].

Photovoltaic Cells

PV technology has been around since the 1950s, but the effect on our lives is sometimes not very obvious to the common man. However, photovoltaic cell technology enabled the development of a whole series of otherwise unthinkable developments. For example, photovoltaic cells generate the power that runs space satellites. Without telecommunication satellites, many of our now-routine activities: from watching internationally broadcast entertainment to using cell phones, would still be in the realm of science-fiction. Space exploration and research might have continued to be far-fetched cosmic imaginations by astrophysists.

On the ground, common PV technology applications may include: domestic lighting, village electrification, water pumping, powering of remote telecommunication repeater stations, railway signals, etc. Nevertheless, PV technology is still expensive, and therefore, extensive use in the Third World may not be feasible due to economic constraints in the immediate future.

1.2.3 Technologies for Domestic High Temperature Heat Production

Solar Cookers - General

A solar cooker, or solar oven is a way of using the sun's power to cook. The simplest solar cooker consists of a foil-lined cardboard reflector and a dark pot placed at the focal point. With proper focusing of beam radiation, this simple mechanism converts sunlight into heat and can cook one or two pots of food at a time. To date, a variety of versions exist and are currently in use in different parts of the world, see [14].

Apart from the obvious need for sunlight and the need to aim the solar oven before use, using a solar oven is not substantially different from a regular oven. Solar cookers are a win-win technology in sun-rich, fuel-scarce areas: they reduce smoke and lung diseases, pasteurize unsafe drinking water, and spare women and children the burdens and hazards of collecting ever-scarcer firewood for cooking.

Humanitarian organizations (e.g Solar Cookers International (SCI), KoZon Foundation, Jewish World Watch, Refugee Foundation Netherlands and CARE International) are promoting their use worldwide to help slow deforestation and desertification caused by the need for wood-fuel. For example, SCI spreads solar cooking awareness and skills worldwide and has enabled over 30,000 families in Africa alone to cook with the sun's energy. It should be noted that this simple technology has provided great relief in meeting water pasteurization and cooking needs in refugee camps. Nevertheless, the main weakness with this technology is lack of storage, its applicability is synchronous and limited to the moment the sun is shinning.

Scheffler's Community Solar Cooker

The German scientist, W. Scheffler developed a heliostat type solar cooker, whose application or purpose approximates (in many respects) the prototype proposed in this work. It outweighs the solar cookers discussed previously in that it is a more permanent structure with an option for thermal energy storage. The first system was built in 1986 and by now several hundreds are being used mainly in India and Africa.

The heliostat of Scheffler's cooker comprises of a primary reflector, a secondary reflector, and a clockwork powered either by gravity or by photovoltaic panels. The primary reflector is in fact part of an (imaginary) paraboloid, such that, it produces a converging beam of sunlight aligned with an axis of rotation which is parallel to the axis of the earth, and which passes through the centers of both reflectors, as shown in figure 1.2. However, the major problem with scheffler-system is that: the seasonal variation in the declination angle requires changing not only the angle be-

tween the primary reflector and its axis of rotation, but also the shape of the reflector.

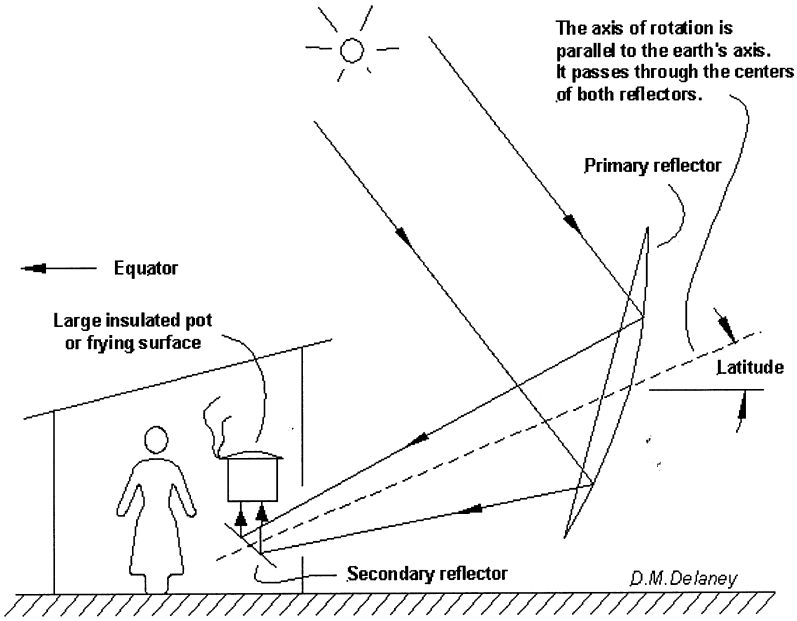

Figure 1.2: Scheffler's Community Solar Cooker. The primary reflector tracks the sun about the axis shown. Once aligned in the morning, the reflector remains synchronous to the sun's motion. Adapted from [15].

The clockwork rotates the primary reflector around its axis of rotation at a rate synchronous to the sun's motion, i.e solar tracking. The fixed secondary reflector reflects the beam from the primary reflector onto a cooking pot or frying surface. The heat storage system consists of an iron mass in an insulated container. One end of the iron mass is exposed to the focus of the heliostat during the day, then capped with an insulated lid to save the collected heat. It is reported to retain heat that can suffice for cooking or frying up to 24 hours later.

1.3 Zimbabwe: Brief Discussions on Pertinent Issues

1.3.1 Location and Geography

Zimbabwe is a landlocked country located in South Central Africa, luckily in this case, lying completely inside a high insolation zone. Its regional location is shown in figure 1.3 and is just north of the Tropic of Capricorn, which is approximately 23° south of the equator. It is bound by South Africa to the south, Botswana to

the southwest, Zambia to the northwest and Mozambique to the northeast, east and southeast..

Figure 1.3: Regional map showing the location of Zimbabwe.

The country is located principally on three high rolling plateaus known as the 'velds'. For convenience, local meteorologists have named these topographical platforms: *The High-Veld*, with an elevation in the range of 1200 m and 1600 m. *The Middle-Veld*, which has an elevation of between 900 m and 1200 m, and finally, *The Low-Veld*, which is below 900 m. Major Cities and towns include Harare, Bulawayo, Chitungwiza, Mutare, Masvingo and Gweru.

1.3.2 Climate and Agriculture

Zimbabwe has a sub-tropical climate that is principally moderated by altitude. There are four somewhat distinct seasons: a warm wet season roughly from late November to early March, followed by a transitional season that stretches to mid-May, then a cool dry winter that usually lasts until early August and finally, a warm dry period from August to late October. Rainfall is the major factor that influences the performance of the agriculture, forestry and wildlife sectors in Zimbabwe. Largely based on the correlation between altitude and mean annual rainfall of the prevailing weather patterns, the country is divided into five climatological regions, see figure 1.4.

Regions marked I and II, on average receive 750 - 1000 mm of rainfall per annum, while the more arid regions III - V, usually get less rainfall and frequently experience severe droughts during the wet season. Of interest to this study is the influence of

climate on the resultant availability of wood-fuel. In essence, the bushes in regions IV and V are savanna-type grasslands with scantly populated trees, while region III is seen as a transitional zone, occurring between the almost sub-tropical wood lands common (but rapidly shrinking) in regions I and II.

The settlement pattern in the rural areas is connected to the social and political imbalances that were prevalent in the colonial era. The majority of the rural folks live in the arid regions, since the arable (agriculture) area, principally regions I and II, were reserved for large-scale commercial farming. Implied is the fact that, a greater part of the rural folks (approximately 70% of the total population) is located in regions III - V, i.e the wilderness[3] in more than 80% of the country is essentially characterized by widely spaced trees. With this background, and also considering the continued exploitation of these bushes over the years, it becomes easier to have a clear insight of the severity and gravity of the energy crisis (as in wood-fuel) in Zimbabwe.

1.3.3 Human Population and The Economy

The 2001 census estimated the population to be 12.8 million and growing at a rate of 2.8% per annum [16]. Slightly over 70% of the people reside in the rural areas where they largely, in most cases entirely, depend on agriculture to meet their food and cash needs. Therefore, the agricultural sector plays a pivotal role as it provides a livelihood for such a substantial percentage of the total population. In addition, agriculture provides raw materials for the majority of the country's manufactured goods.

Before the chaotic agrarian reform, now widely known and understood to be a dismal failure, agriculture used to contribute on average 30% of the GDP, $40 - 50\%$ of the exports and 60% of industrial raw materials [17]. As such, agricultural production was the backbone of the Zimbabwean economy. The disruption of productive agricultural activities have seen the economy shrinking since about 2000, with annual inflation figures well in excess of 8000% at the time of writing.

By the end of 2004, the National AIDS Coordination Programme estimated that over 2 million Zimbabweans had been infected with HIV and that the adult prevalence rate was over 30%. Most of the AIDS cases are among the productive age group ($20 - 39$ year-olds). The epidemic has reduced the life expectancy from 62 for women and 58 for men in 1990 to slightly below 40 for both sexes [18]. As a consequence, the projected population growth rate by 2015 is 0.2% or even negative, largely due to

[3] Regions III, IV and V cover approximately 84% of Zimbabwe.

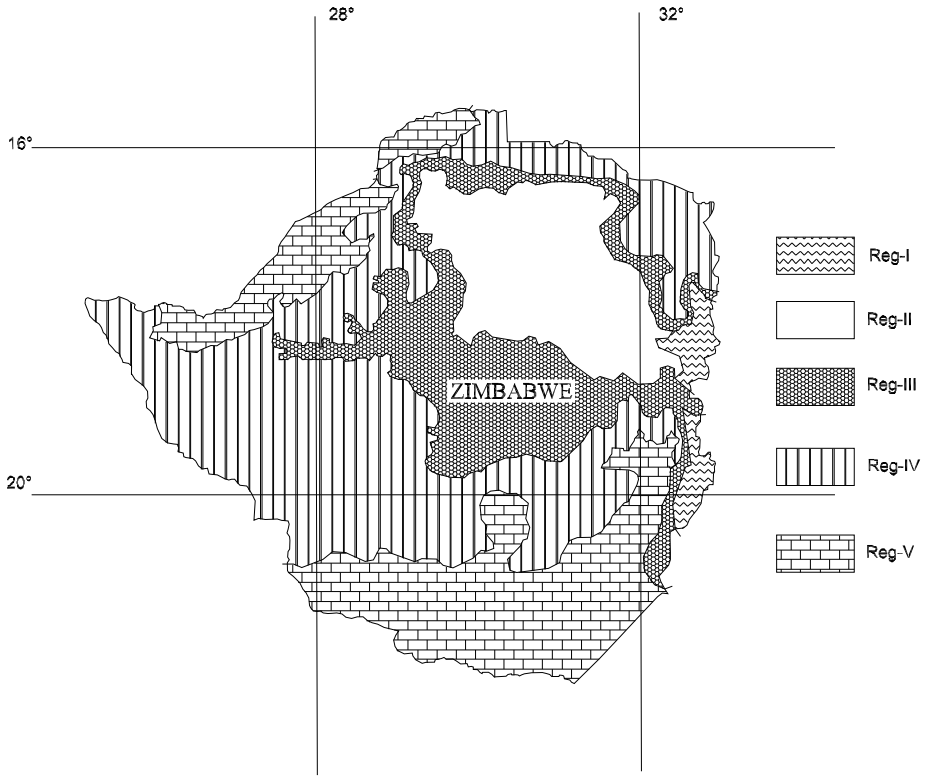

Figure 1.4: A map illustrating the climatological zones in Zimbabwe.

the HIV/AIDS pandemic. As such, the AIDS scourge poses a serious threat to the country's development and future.

1.3.4 Demand for Wood-fuel Versus Available Resources

Zimbabwe relies mainly on coal for thermal energy in industry and thermal power generation. Electricity is produced from hydro-resources of the Zambezi. However, a substantial 35% has to be imported from the neighboring countries in order to meet the country's needs. Biomass is the main source of energy for rural household which represent over 70% of total households in the country [19].

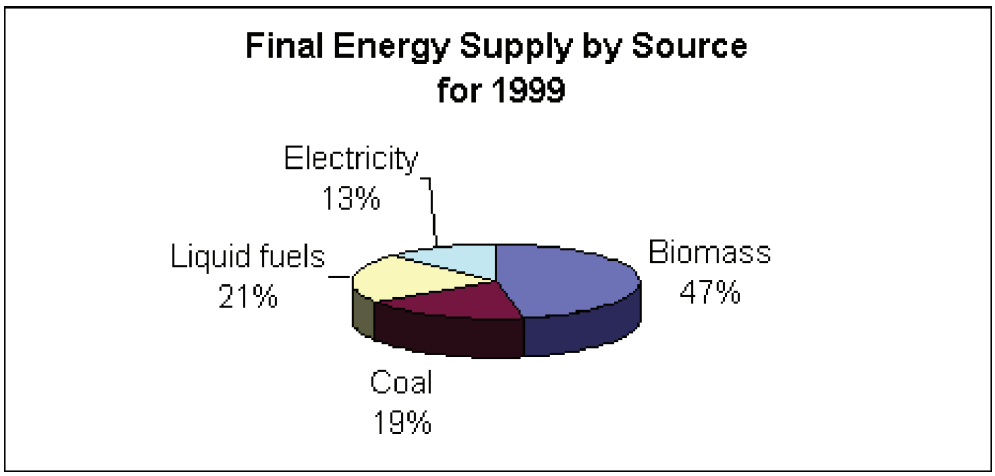

Figure 1.5: Biomass, which is essentially wood-fuel for Zimbabwe, is the major source of energy for cooking, lighting and heating for over 70% of the population. Adapted from [20].

As illustrated by figure 1.5, wood is the single largest source of energy in Zimbabwe, supplying quite close to 50% of total energy consumed in the country [20]. Depending on the region, a moderate family in Zimbabwe would require 8-10 cords[4] of firewood annually to meet their needs [21, 22]. Already, demand for wood-fuel exceeds supply in most parts of the country, with profound scarcity in Region IV and V, see figure 1.4.

Basically, over-grazing, excessive cutting down of trees with no reforestation schemes, poor farming methods, combined with the soil erosion, have caused and continue to aggravate desertification (now a major cause of concern) in most parts of the country [23]. Between 1990 and 2005, Zimbabwe is reported to have lost 21 percent of its forest cover with no primary forests left [24]. As a result, forest fronts have been driven further and further away from the populated villages. Consequently, rural

[4] One cord of neatly packed firewood will occupy $\simeq 3.62$ m^3.

Figure 1.6: A picture showing children carrying firewood in a rural area located on the outskirts of Harare, Zimbabwe. The two girls in the picture report of having to routinely endure covering on average, distances of up to 9 km (to and fro), at least twice a week to fetch firewood.

folks now have to cover toilsome distances of up to 5 km or more one-way, only to come back carrying a grueling load of firewood, under a scorching sun most of the time.

It is important to note that all the firewood for household consumption in rural areas is cut using rudimentary tools (e.g a simple axe) due to lack of resources. Even worse, the transportation is usually done manually as illustrated in figure 1.6. And quite sadly, due to an unjustified and still largely uncorrected cultural heritage, the burden of fetching firewood for household consumption is mostly done by women and children, even to date. For a greater majority, fetching wood-fuel this way is an almost daily challenge, unfortunately worsening, but apparently there to stay.

1.3.5 Solar Energy Projects in Zimbabwe

Zimbabwe went through a period characterized by vigorous rural development efforts after attaining its independence in 1980. Officially documented solar-related projects implemented in the 1990s were largely sponsored by Global Environmental Facility - United Nations Development Programme (GEF-UNDP) and the government of Zimbabwe, through the Energy Technology Institute (ETI) of the Scientific and Industrial Research and Development Centre (SIRDC).

An overview of the major solar power dissemination projects in Zimbabwe as documented by Mulugetta et al., Mupako and Maboyi [25, 26, 27] reveal that the main focus has been set on photovoltaic technology. Also, the results of a recent study by Batidzirai [28], factually suggest that the use of flat plates for water heating systems (apparently not promoted) in schools, tourism industry, etc; can significantly alleviate energy shortage problems.

It has been estimated that Zimbabwe has a total of 85 000 solar home systems, an applausable figure which would make it one of the countries with the largest number of solar home systems in the region [29, 30]. Even so, this number is insignificant compared to the vast potential that exists for PV as an energy source. Nevertheless, it appears that there is no documented solar concentrator-system initiatives or activities to date, save a 1979 thesis by Rogers mainly discussing the potential of solar cookers without storage [31] in Zimbabwe.

The Government of Zimbabwe views electricity as a critical development factor in increasing literacy, slowing rural-urban migration and improving the overall quality of life for the country's rural population (over 8 million people) outside the national electricity-grid. While this prioritization is understandable, it remains a stubborn

fact that efforts to mitigate the energy crisis (and the associated problems) in the rural areas by means of photovoltaics remain frustrated to date, simply because they have not addressed the more basic high-temperature-heat needs: particularly for food preparation and boiling. However, it is our considered view that this niche can arguably be patched by the use of appropriate cost-effective, small scale solar concentrating systems with storage.

1.4 Chapter Summary and Conclusions

This chapter mainly discusses the energy resource situation in Zimbabwe and how the available solar resources, with the application of appropriate technologies, could mitigate the deepening energy crisis. To asses the potential of the present research in that country, relevant issues (geography, climate, energy needs versus available resources, solar projects, etc) in the solar energy context, have been discussed in some detail.

The majority of the people (approximately 70%) in Zimbabwe depend on wood fuel to meet their cooking needs. Unfortunately the forest resources can no longer cope with demand and are fast diminishing due to recurrent droughts, continued and uncontrolled exploitation over the years, etc. In general, the current energy resources that Zimbabwe is exploiting to meet its energy demands are not adequate. However, taking advantage of Zimbabwe's high solar insolation as demonstrated in the next chapter, a combination of the proposed prototype and direct use of heat (e.g flat plate) has tremendous potential in meeting the rural folk's energy needs throughout the year, with only minimal back-up needed.

References

[1] Survey of Energy Resources, *World Energy Council*.
http://www.worldenergy.org/wec-geis/publications/reports/ser/overview.asp

[2] Van C, Guidi D and Best G, 'Solar Photovoltaics for Sustainable Agriculture and Rural Development', Rome: FAO, 2000.

[3] Twidell W. J and Weir D. A,'Renewable Energy Resources', Spon Press, Taylor and Francis Group, 1986.

[4] Perlin J, 'From Space to Earth: The Story of Solar Electricity', *Ann Arbor: AATEC Publications*, 1999.

[5] Paley Commission, Resources for Freedom, vol. IV, The Promise of Technology: *The Possibilities of Solar Energy*, Washington D.C., 1952.

[6] Planning and Installing Thermal Power Systems: A guide for installers, architects and engineers, James and James (Science Publishers), 2005.

[7] Tyner C. E and Gregory J. K, Geyer M and Romero M, 'Concentrating Solar Power in 2001', *in An IEA/SolarPaces Summary of Present Status and Future Prospects*, January 2001.

[8] Murphy, Pamela, 'IEA Solar Heating & Cooling Programme', *in Morse Associates Inc.,* 2000 *Annual Report*, 2001.

[9] Stine W.B, Harrigan R.W, 'Solar Energy Fundamentals and Design', 1985.

[10] Solar Paces Home Page.
http://www.solarpaces.org/csp_technology.htm

[11] National Renewable Energy Laboratory, in Golden, Colorado, USA. NREL Home page.
http://www.nrel.gov/solar/

[12] United States Department of Energys Office of Energy Efficiency and Renewable Energy.
http://www.personal.psu.edu/users/d/d/ddr121/government.htm

[13] Sandia National Laboratories - Home page.
http://www.sandia.gov/news-center/news-releases/2004/renew-energy-batt/Stirling.html

[14] Solar Cooking International - Home page.
http://solarcooking.org/plans/

[15] Scheffler's Community Solar Cooker - Home page.
http://www.geocities.com/∼ dmdelaney/scheffler-precis/scheffler-precis.html

[16] Central Statistics Office Zimbabwe, 2002, Stats-Flash, 2001.

[17] Central Statistics Office Zimbabwe, Quarterly Digest of Statistics $1990 - 1999$.

[18] Central Statistics Office Zimbabwe, Quarterly Digest of Statistics, $2000 - 2005$.

[19] EC & DBSA & ISES, 2000, Renewable Energy Technologies in SADC- A guide for investors.

[20] GoZ-DoE. 'Energy Bulletin Vol.9, No.1, July 2001'.

[21] UNEP-SCEE. 'Implementation Strategy To Reduce Environment Impact of Energy Related Activities in Zimbabwe'. 1995.

[22] GoZ-Ministry of Mines. 'Environment and Tourism, Environment Impact Assessment Guidelines'. 1997.

[23] Mushaka A and Maruzane D, 'Performance of some multipurpose tree species: the Forestry Commission experience', *Transactions of the Zimbabwe Scientific Association* Vol.72, (Supplement), pp. $10 - 14$, 1998

[24] Mufandaedza E, 'Tropical secondary forest management in Africa: Reality and perspectives, Zimbabwe Country Paper', *Workshop on tropical secondary forest management in Africa*, Nairobi, Kenya, $9 - 13$ December 2002.

[25] Mulugetta Y, Nhete T, and Jackson T, 'Photovoltaics in Zimbabwe: lessons from the GEF Solar project', *Energy Policy*, Vol.28, No. 14 (Nov. 2000).

[26] Mapako M, 'Provision of long-term maintenance support for solar photovoltaic systems. Lessons from a Zimbabwean', *NGO study-Published in the Journal of Energy in Southern Africa*, Vol. 16 No.4, February 2005.

[27] Maboyi B, 'Technology Transfer Overlooked in GEF Solar Project', *Renewable Energy for Development* , Vol. 8, No. 4, December 1995.

[28] Batidzirai B, 'Potential for Solar water heating in Zimbabwe', *Master's Thesis 2004*, Dept of Science, Technology & Society, Utrecht University, The Netherlands.

[29] Zimbabwe-UNDP&GEF Solar Project. 'Annual Report 1997', Project Management Unit, Harare.

[30] JICA, 'Final Report of the Study Phase of the Zimbabwe Electrification Master Plan Study', *JICA* 1999, Tokyo.

[31] Rogers P.M, 'Solar Box Cookers in Zimbabwe:The Introduction of a Radical Innovation in Cooking', *MSc Thesis* 1979, University of California, USA.

Chapter 2

Solar Radiation: Availability in Zimbabwe

2.1 Extraterrestrial Radiation

Solar radiation incident outside the earth's atmosphere is called extraterrestrial radiation or total solar irradiance (TSI), and is in fact, the amount of global radiation that a location on earth would receive in the absence of the atmosphere. In general, the long-term average of the TSI at mean earth-sun distance, at the top of the atmosphere is called the *Solar Constant*. Since literature (see for example ASTM [1]) gives slightly different values of the solar constant, the World Meteorological Organization (WMO) recommendation of 1367 Wm^{-2}, will be used in this work [2] unless stated otherwise. According to Gueymard [3], TSI measurements have an inherent absolute uncertainty to the order of 0.1% or 1.4 Wm^{-2}, an arguably small amount in our case.

Knowledge of the relative amount of energy contained in sunlight of different wavelengths permits the engineer to evaluate the impact of wavelength phenomena on total energy collection. The radiant energy coming from the sun is distributed over a range of wavelengths[1]. Water vapour is largely responsible for the strong absorption bands in the infrared region. The high-altitude atmospheric ozone absorbs practically all the radiation below 0.30 μm. The general picture is that the atmosphere, under normal circumstances, acts as a spectral window 'only' allowing solar radiation in the range $0.30 \leq \lambda \leq 2.5$ μm to reach the earth's surface.

2.1.1 Components of Solar Radiation

As extraterrestrial radiation passes through the atmosphere, some of it is scattered back into space, another part is absorbed by air, aerosols and water vapour. The

[1] A typical spectral distribution of the solar flux is shown in figure 7.7 in the appendix.

part of solar radiation that reaches the surface of the earth with essentially no change in direction is called **direct or beam radiation**. Solar radiation scattered in the atmosphere is referred to as **Diffuse radiation**. The sum of the beam and diffuse radiation on a surface is called **total or global solar radiation**, see figure 2.1.

On a clear day, direct solar irradiance constitutes about 80 to 90 % of the total amount of solar energy reaching the earth's surface. Localized blockage of the direct component of solar irradiance produces shadows. In overcast weather or on a foggy day, 'when we can't see the sun', the direct component of solar irradiance is essentially zero and there are no shadows. Beam radiation is of great interest to designers of high-temperature solar energy systems because it can be concentrated, whereas the diffuse component cannot.

2.2 Instruments for Solar Radiation Measurements

2.2.1 Pyranometers

A pyranometer is used for measurement of the global horizontal solar irradiance. For this purpose, it is placed in a horizontal orientation and sufficiently high above the surroundings so that it has a clear, hemispherical view of the entire sky with no shading or obstructing trees and (or reflecting) buildings within this field of view. In principle, it measures the sun's energy coming from all directions (2π steradian) in the hemisphere above the plane of the instrument. The detectors for these instruments must have a response independent of the incident angle of the solar radiation, and also of the wavelength over the solar energy spectrum.

A properly designed instrument measures radiation in all the solar wavelengths (e.g 0.3 to 2.8μm for Eppley precision pyranometer: Model PSP). Its response to direct radiation should be proportional to the cosine of the angle between the sun and a line normal to the pyranometer absorber surface, commonly known as the *cosine effect*. Most pyranometers are covered with two hemispherical glass domes to protect them from wind and bad weather. Important to stress is that these covers must be very uniform in thickness to avoid causing an uneven distribution of radiation on the detectors. An elaborate characterization of pyranometers may be found in literature that includes Bush et al. [6].

For a horizontally oriented pyranometer, the direct normal solar irradiance is reduced by the cosine of the angle of incidence, which in this case, is the solar zenith angle. In this work subscripts used on hourly and daily solar irradiance, I and H respectively, are as follows : o refers to radiation above the earth's atmosphere, b refer to normal

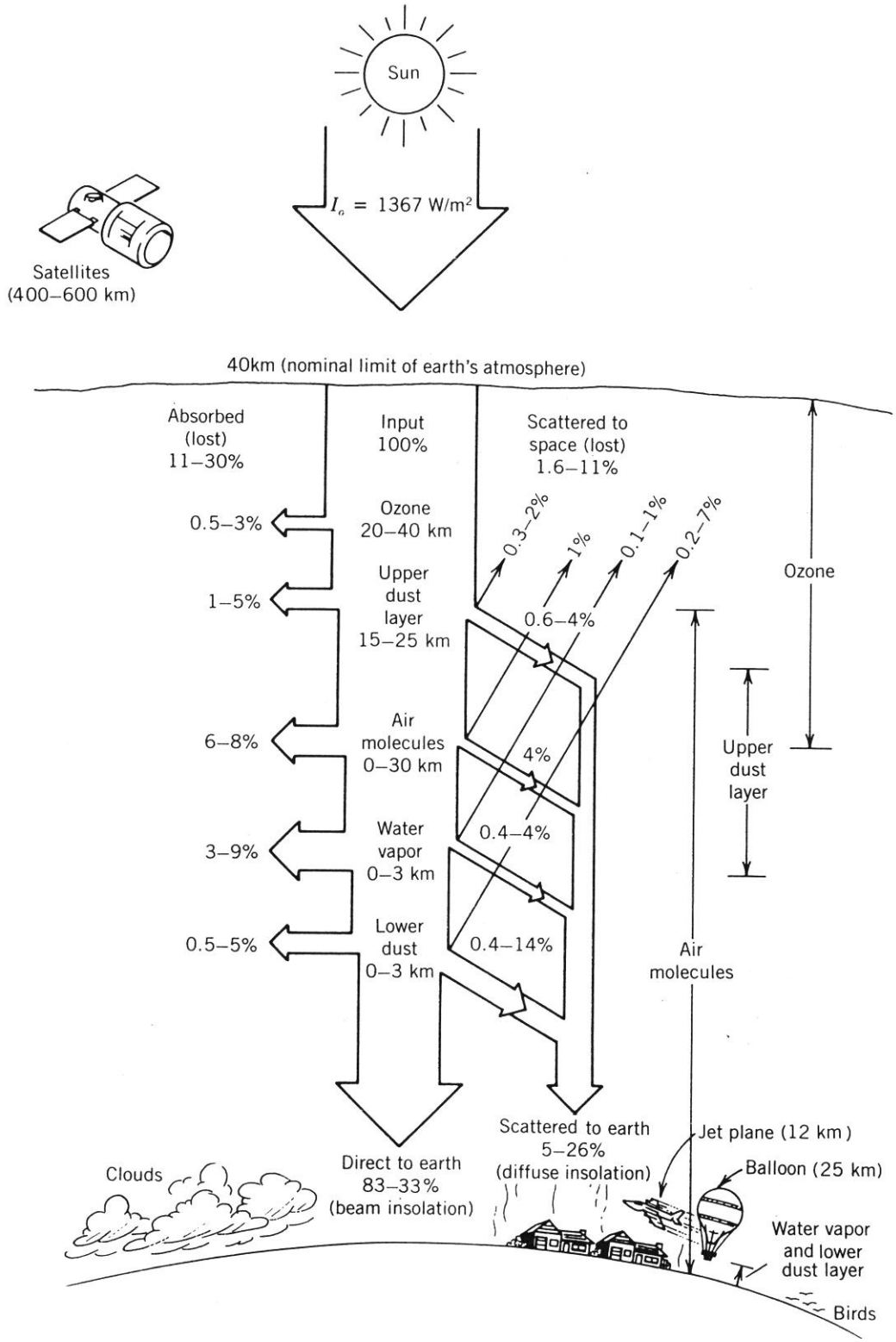

Figure 2.1: Nominal range of clear sky absorption and scattering of incident solar energy. Adapted from: http://www.powerfromthesun.net/chapter2/Chapter2.htm

beam, d diffuse radiation, and h to horizontal orientation. The measured global horizontal solar irradiance is given by:

$$I_h = I_b \cos\theta_z + I_{d,h} \tag{2.1}$$

Pyranometers may also be used to measure the global solar irradiance on inclined surfaces. However, according Stine [3], various studies have indicated the possibility that pyranometer calibration may change with inclination.

2.2.2 Normal Incidence Pyrheliometer

To measure the direct normal component of the solar irradiance only, an instrument called a normal incidence pyrheliometer, popularly abbreviated as NIP is used. Absolute and reference-standard pyrheliometers are used as references in solar radiometer calibrations. Routine measurements of beam radiation are taken by field pyrheliometers because standard pyrheliometers are not easy to use.

The NIP is a broadband instrument that measures the direct (or beam) component of solar radiation at normal incidence. It is always aimed directly at the solar disc. Its spectral sensitivity should accommodate all wavelengths reaching the earth's surface from the sun, e.g a typical range of 0.28 to 3.0 μm for the Eppley type.

The aperture of the NIP is small enough to minimize the registration of circumsolar radiation but large enough to allow for the performance tolerance of the tracker. Resultantly, although the average subtended angle of the sun as viewed from the earth is approximately 0.5°, WMO [8] recommends a 5° full field of view, a 1° slope angle and a 4° limit angle, see figure 2.2 for definitions. Implied is the fact that all pyrheliometers adhering to WMO specifications measure a solar aureole component to the order of 1° or less [9, 10].

Solar irradiance enters the instrument through a crystal-quartz window that is sealed to the aperture. Within the instrument, the irradiance is directed onto a black receiver on which a set of thermocouples (a thermopile) is cemented. The radiation warms the detector and excites the thermopile, which produces an electrical signal. A calibration factor is applied to convert the millivolt signal to an equivalent radiant energy flux in watts per square meter.

Commonly used commercial solar trackers include the Eplab model-ST (which has a pointing accuracy to the order of 0.25°) and the Kipp & Zonen type. Automatic trackers, such as Eplab's SMT-3, EKO'S STR and BRUSAG's INTRA have of late increased in popularity. Generally, they have an accuracy of 0.1° or less because they have what is called an inbuilt active solar positioning feedback mechanism, which

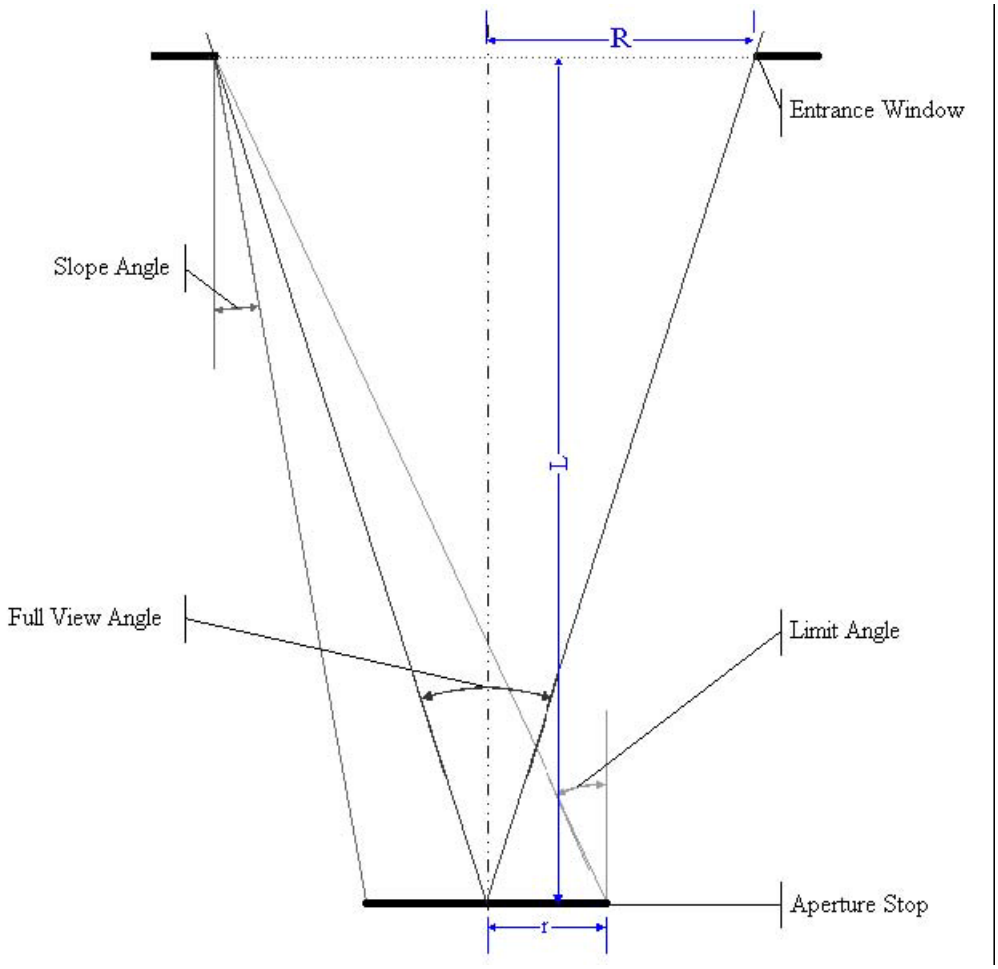

Figure 2.2: A schematic to show the view limiting angles for a typical normal incident solar radiometer. Adapted from [9].

makes the tracking errors quite minimal.

2.2.3 Diffuse Irradiance

Pyranometers may be modified to measure only the diffuse component of the global horizontal radiation $I_{d,h}$. Providing a 'shadowing' device just large enough to block out the direct irradiance coming from the sun's disc does this. To avoid moving a shadowing disc continously throughout the day, a shadow band is often incorporated. This band must be adjusted often during the year to keep it in the ecliptic plane. Adjustments every second day are recommended. However, since the shadow band blocks part of the sky, corrections for this blockage must be considered.

Rotating shadow band pyranometers have been developed in the recent years. Their use is fairly on the increase. With this design, the shadow band rotates slowly about the pyranometer blocking the direct irradiance from the sun at a certain frequency. The signal from the pyranometer reads global horizontal irradiance most of the time, with periodic reductions down to the diffuse irradiance level when the shadow band passes between the sun and the pyranometer.

This design gives the advantage of using a single pyranometer to measure both global horizontal and diffuse horizontal solar irradiance. The rotating shadow pyranometer also avoids the constant adjustment of the plane as in the case of a fixed shadow band. Based on equation (2.1), measurements from the rotating shadow band pyranometer can be used to determine the direct normal irradiance without the need for a tracking pyrheliometer.

2.2.4 Sunshine Recorders

In addition to the pyranometer and the normal incidence pyrheliometer data, there is a traditional measurement oftenly reported in meteorological observations: duration of sunshine hours. The instrument commonly used to measure this parameter is the Campbell-Stokes sunshine recorder. This instrument consists of a glass sphere that focuses the direct solar radiation and burns a trace on a special pasteboard card.

Sunshine recorder measurements seem to be of minimal use to engineers due to the associated limitations: there is no measure of intensity other than a threshold[2] intensity [11] and that they do not respond to low levels of radiation early and late in the day. In addition, the condition of the sunshine cards may depend on the amount

[2]Iqbal suggests a generalized threshold of 210 W/m^2.

of humidity for a given place. However, models have been developed to correlate these data with daily or monthly solar radiation averages as will be applied in a later section.

2.3 Worldwide Solar Radiation Data-base

A comprehensive climatological data-base, called METEONORM, has been developed for solar engineering applications [12, 13]. METEONORM allows calculation of solar radiation data for an arbitrarily oriented surface based on available radiation data. It is essentially a computer program permitting calculation of hourly values of solar radiation data. The same is targeted to cover the whole world, and has thus far been validated at many sites. In order to improve the quality of the results, METEONORM is continually being updated, under the auspices of extensive international research programs [14, 15], to include more weather station data, and therefore reduce the amount of extrapolation necessary between sites.

2.4 Zimbabwe: Solar Radiation Data

In this research, the need to study the feasibility of the proposed prototype (solar oven with storage) in Zimbabwe requires a clear insight regarding the availability of solar energy, i.e instantaneous fluxes of global, diffuse and especially normal beam radiation. Nevertheless, for the purpose of engineering design and the basic assessment of the viability of solar concentrating systems, only the monthly averages of the above quantities will be sufficient to meet the scope of the necessary feasibility studies in our case.

Monthly average pyranometer data from 20 meteorological stations, combined with sunshine measurements from 10 other stations (without pyranometer data) recorded during the 1981-2000 period, were used to develop a long-term monthly average daily global radiant-exposure database over Zimbabwe. This gives a total of 30 locations from which relevant irradiation data could be obtained, and as can be seen on figure 2.3, the said meteorological stations are fairly scattered through-out the country.

2.4.1 Selection of Data

Before the data was incorporated to form the main monthly average daily global insolation data-bank, both the pyranometer and sunshine records were vetted for consistency, in which case, values with a difference in excess of 25% from the monthly mean (of that particular month and location) were regarded as out-liers. Data discarded through this criteria was to the order of 2% or less for a few stations. Readings that

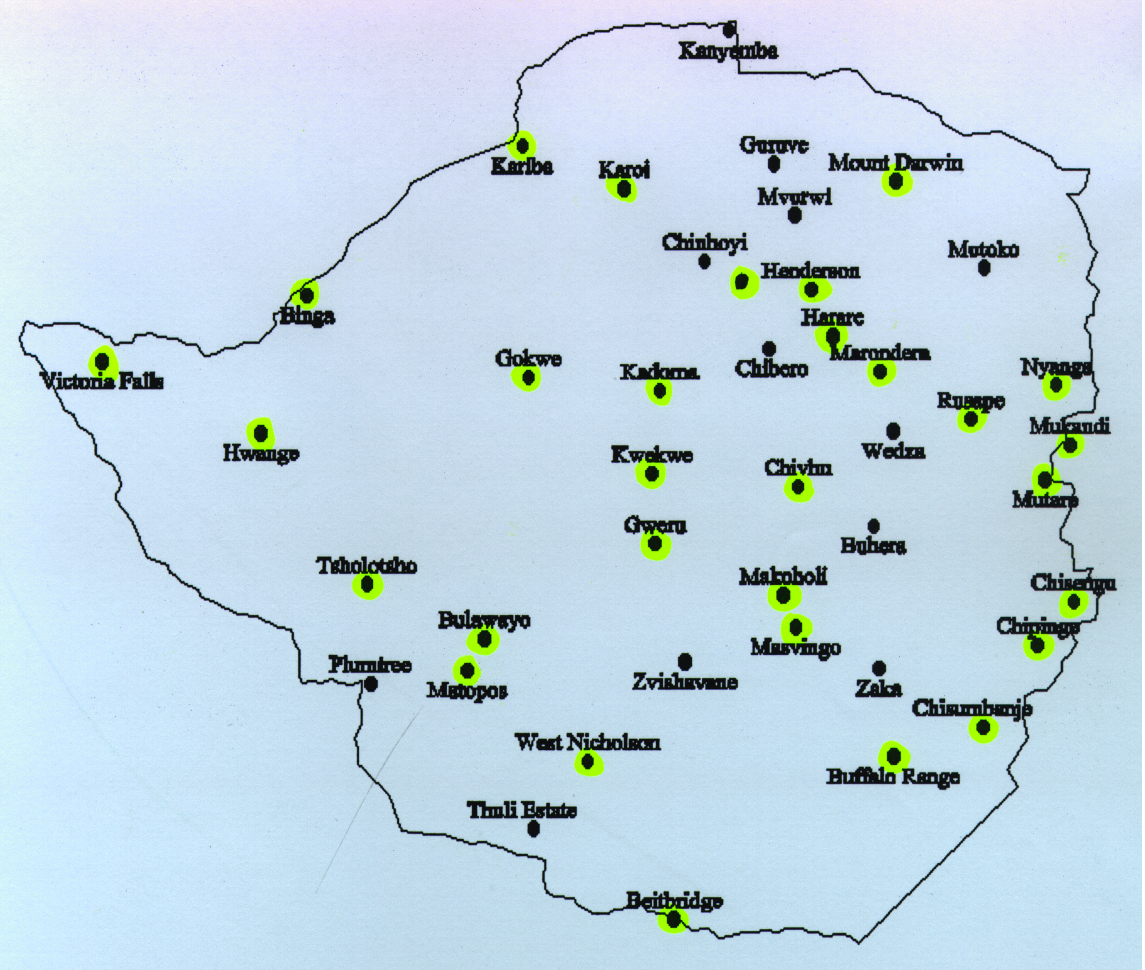

Figure 2.3: Map showing towns and cities in Zimbabwe, some of which include meteorological stations. Stations where radiation measurements were obtained are indicated in green.

passed the screening were then averaged over their respective periods of measurement: ranging from 10 to 20 years depending on the availability of records between 1981 and 2000 for the station in question.

2.4.2 Estimation of Monthly Average Daily Global Radiation from Sunshine Hours

As mentioned earlier, 10 of the 30 stations had sunshine duration records only as data with relevance to this study. The correlation developed by Ångström and later modified by Prescot et al. [11][3], was applied to estimate the monthly average daily global radiant exposure $\bar{H}$ for those stations without pyranometer measurements. The relationship is commonly expressed as:

$$K_T = a + b(\frac{\bar{n}}{\bar{N}_d}) \tag{2.2}$$

where $\bar{n}$ is the monthly average daily duration of sunshine and $\bar{N}_d$ is the astronomic day length. By using the least-squares fit technique, a and b are correlation coefficients which can be determined from the measured sunshine duration and clearness index K_T $(= \bar{H}/\bar{H}_o)$.

Angstrom Regression Coefficients for Zimbabwe

Sub-reg	**One**	**Two**	**Three**	**Four**	**Five**	**Six**	**Seven**	**Eight**
Lat(°)	−18.75	−16.25	−18.75	−21.25	−21.25	−18.75	−17.25	−18.75
Lon(°)	33.75	31.25	31.25	31.25	28.75	28.75	28.75	26.25
a	0.32	0.36	0.27	0.24	0.29	0.32	0.35	0.25
b	0.45	0.43	0.48	0.49	0.46	0.47	0.48	0.58

Table 2.1: The regression coefficients for the sub-regions covering Zimbabwe. **Sub-reg**, **lat** and **lon** are shortcuts for Sub-region, latitude and longitude respectively. Adapted from [16].

The work done by Hove and Götsche [16] in which they determined the local coefficients a and b (see table 2.1) for different parts of Zimbabwe is considered rigorous enough for use in this research, albeit be before adoption, checks were made in each climatological region (discussed in the previous chapter) to validate these coefficient. A comparison of the sky clearness index obtained from equation 2.2 and its counterpart based on pyranometer measurements is presented in figure 2.4 for five stations, each in a different climatological region. The results show that the sunshine derived estimates are essentially confined to within 10% of the measured values, giving

[3]Both Angstrom and Prescot et al. are quoted by Iqbal.

credibility to the adoption of the said coefficients to compute the desired long-term estimates of diffuse acceptable for use in this research.

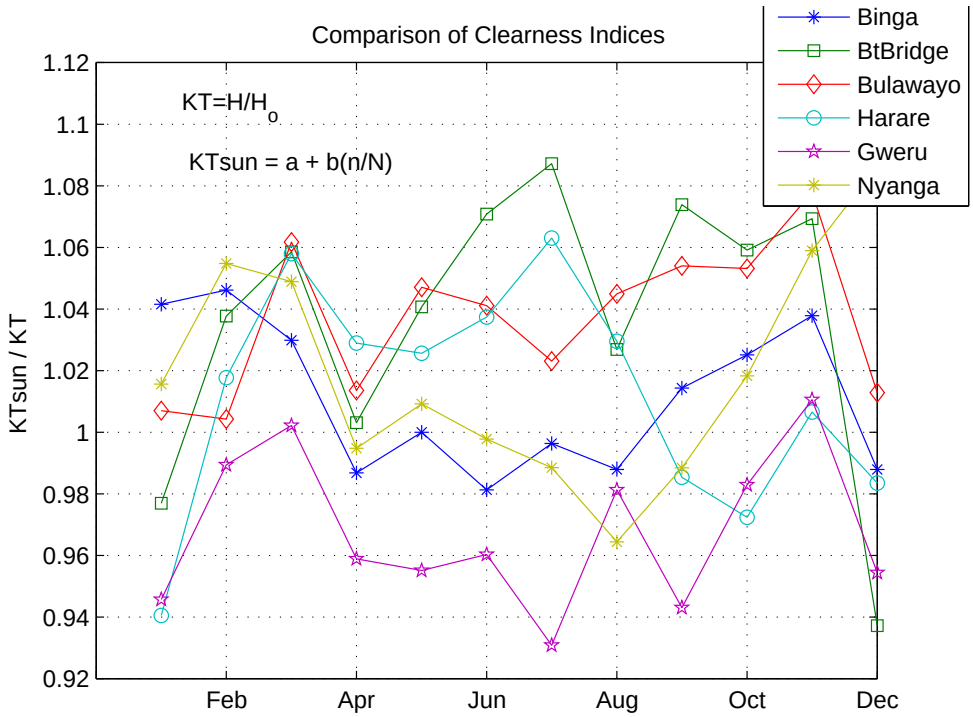

Figure 2.4: Plots showing ratios of KTsun to KT. Gweru had no good record of sunshine hours, so corresponding data from neighboring Kwekwe were used to derive the global radiation estimates. Also, no coefficients were determined for the sub-region containing Beitbridge (BtBridge), so values for Binga (similar climate) were used, albeit the results are within an acceptable margin ($\pm 10\%$) in both cases.

The averages from the pyranometer measurements and those derived from sunshine data are presented as tables 7.1 and 7.2 in Appendix A. To facilitate a quick intuitive assessment of the monthly average daily insolation for the different locations, kWh/m^2 per day, are used instead of the SI-units (MJ/m^2) per day.

2.4.3 Generation of the Monthly Average Daily Diffuse Radiation Estimates

In Zimbabwe, hourly diffuse radiation is recorded at only two sites; Harare and Bulawayo through the shadow-ring technique. Thus said, implied is the need to model the hourly values of diffuse insolation for the rest of the country. Several correlations are available in literature but were as-a-matter-of-factly developed using data for

specific locations. And so, the general validity and applicability of these correlations for application at locations situated elsewhere leaves a lot to be desired unless consistency checks are made with local data.

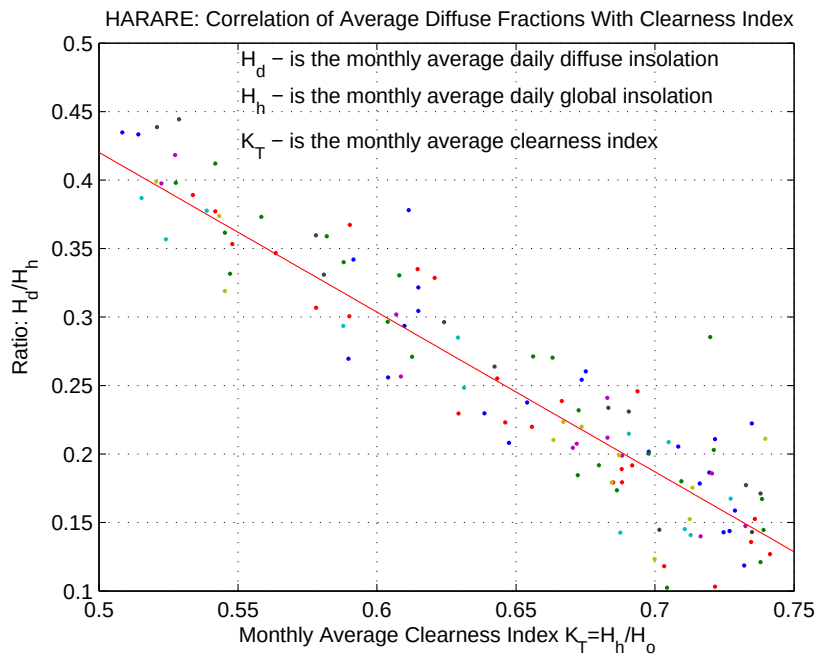

Figure 2.5: Correlation of monthly average daily diffuse fraction with the corresponding monthly average clearness index, based on 1990 - 1999 data from Harare.

As a guide[4] for the purposes of this work, an attempt was made to develop a diffuse correlation based on local data from Harare. The results, which are presented in figure 2.5, yielded the following correlation:

$$\frac{\bar{H}_d}{\bar{H}_h} = 1.0011 - 1.1607\bar{K}_T \qquad for \qquad 0.5 < \bar{K}_T < 0.75$$

with a deviation of nearly 20%. It agrees fairly well with another correlation developed by Götsche and Hove based on local data(1980 - 1992) from Bulawayo. It is suspected that the differences are probably due in part to shading-ring corrections, and possibly in part, due to the criteria used to extrapolate missing data. A comparison is shown in figure 2.6, where another correlation by Page [17], has been selected from literature because it has been found to exhibit an impressing similarity as shown.

[4]A guide because the diffuse irradiance records (1990 – 1999) at our disposal were of mediocre quality i.e a substantial amount of data was missing.

The correlation by Erbs et al. has been included to suggest the need to explore and find out if seasonal dependence exist for the localized correlations in future [18]. The striking congruency (its essentially like a family of curves in this case) among them qualifies the idea that a certain correlation can be applied at other locations lying at the same latitude and of like climatic conditions. All the same, checks for consistency with local data are recommended in all cases to avoid false impressions especially from overestimated and therefore, misleading numbers.

Page's correlation seems to be the obvious choice since it yields moderate results compared to the other two. However, in order to ensure conservative estimates of beam radiation without local measurements, it is our considered view, that a credible and pragmatically 'safe' approach incurs selecting from the available set, a correlation that tends to overestimate the desired diffuse values. Therefore, for the purposes of this work, Götsche's correlation, was adopted for all diffuse modeling over Zimbabwe. It is given by:

$$\frac{\bar{H}_d}{\bar{H}_h} = 1.0294 - 1.144\bar{K}_T \qquad for \qquad 0.47 < \bar{K}_T < 0.75$$

$$\frac{\bar{H}_d}{\bar{H}_h} = 0.75\bar{K}_T \qquad for \qquad \bar{K}_T > 0.75 \tag{2.3}$$

The spatial and seasonal average of the deviation computed by this correlation is reported to be 10%. In our case, we assume the margin of error on diffuse radiation values to be to the same order. As mentioned earlier, the correlation based on Harare-data was only used as a guide (due to the mediocrity in quality of the diffuse records) and was therefore, not taken into account in this matter.

2.4.4 Computation of Normal Beam Estimates

Estimates of long-term beam insolation at normal incidence to the surface for an hour I_b, were generated from the hourly hemispherical irradiation on a horizontal plane I_h, and their respective hourly diffuse irradiation values $I_{d,h}$, by applying a rearranged version of equation (2.1) to get:

$$I_b = \frac{I_h - I_{d,h}}{\cos\theta_z} \tag{2.4}$$

where θ_z is in this case, the angle of incidence of beam radiation on a horizontal surface at the mid-point of the hour of interest (solar time is understood).

The hourly irradiation values for the global and diffuse, were determined using the conversion factors, commonly written as r_t and r_d, developed by Collares-Pereira and Rabl [19]. They can be expressed as:

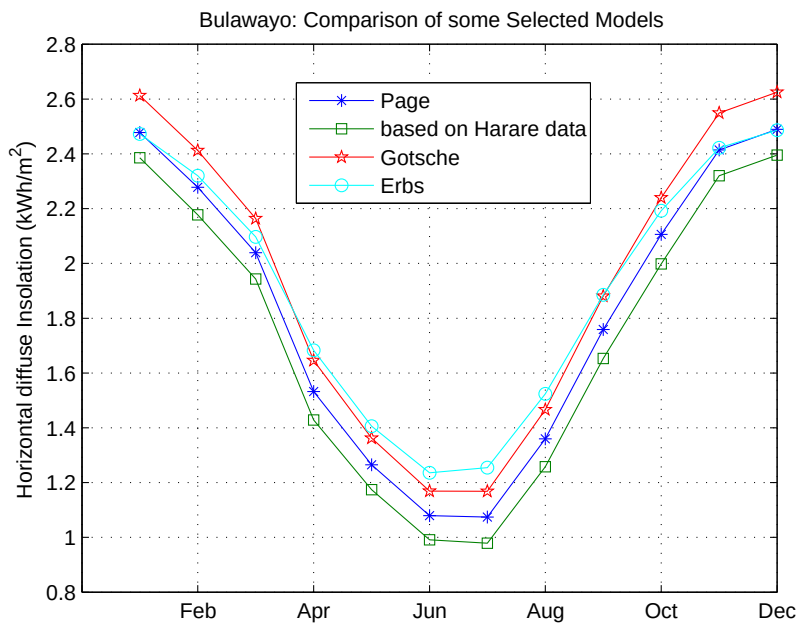

Figure 2.6: Plots comparing results from a selected set of different models using Bulawayo data.

$$r_t = \frac{\bar{I}_h}{\bar{H}_h} = \frac{\bar{I}_o}{\bar{H}_o}(a_r + b_r \cos\omega_i) \tag{2.5}$$

where

$$a_r = 0.409 + 0.5016 \sin(\omega_s - 60^\circ), \qquad b_r = 0.6609 - 0.4767 \sin(\omega_s - 60^\circ)$$

$$r_d = \frac{\bar{I}_{d,h}}{\bar{H}_{d,h}} = \frac{\pi}{24} \frac{\cos\omega_i - \cos\omega_s}{\sin\omega_s - (\omega_s \frac{\pi}{180}) \cos\omega_s} \tag{2.6}$$

In both cases, ω_i and ω_s are the ith hour-angle and the sunset hour-angle respectively, while $\bar{I}_o$ is the hourly extraterrestrial insolation at the average day of the month, the rest have their usual meanings as before.

r_t and r_d were normalized to make them satisfy the condition that their sum over all daylight hours under consideration should be equal to 1. In other words, they were corrected to comply with the requirement that

$$\sum_{i=1}^{n} r_t(t)\bar{H}_h = \bar{H}_h \tag{2.7}$$

$$\sum_{i=1}^{n} r_d(t)\bar{H}_{d,h} = \bar{H}_{d,h} \tag{2.8}$$

where n is the average number of sunshine hours for the month in question. As a conservative measure, the limits to compute normal beam were set at $-82.5° \leq \theta_z \leq 82.5°$. The variation of r_t and r_d with latitude was assumed to be negligible within 5° of latitude, so latitude values for Bulawayo and Harare were used for all stations, with the choice depending on the proximity of the station in question, to either of these reference sites.

2.5 Results and Discussions

2.5.1 Normal Beam Estimates Over Zimbabwe

Depending on the magnitude of the prevalent normal beam insolation estimates across Zimbabwe, it was considered appropriate to divide the country into three 'solar sub-regions' for convenience in describing the findings. In this study, we will call these sub-regions Zim-East, -West and -South, and are illustrated in figure 2.7. The specific definitions adopted to describe these sub-regions are as follows:

Zim-East - north of 20° latitude and east of 30° longitude: Mt.Darwin, Nyanga, Mukandi, Mutare(Grand Beef), Rusape, Chivhu, Marondera, Harare, Henderson.

Zim-West - north of 20° latitude and west of 30° longitude: Binga, Victoria Falls, Hwange, Gweru, Kwekwe, Gokwe, Kadoma, Karoi, Kariba.

Zim-South - south of 20° latitude: Chisengu, Chipinge, Chisumbanje, Masvingo, Makoholi, Tsholotsho, Bulawayo, Matopos, West Nicholson, Beitbridge, Buffalo.

Results of the estimated monthly average daily normal beam insolation, expressed in kWh/m^2 per day for convenience, are presented in table 2.2 and 2.3, while the spatial (as in the solar sub-regions) and temporal (time of the year) aspects are summarized in figures 2.8, 2.9 and 2.10. To enable a practical contribution in solving the energy crisis in Zimbabwe as proposed in this research, detailed temporal normal-beam radiation estimates, for the monthly average daily radiation, and for the individual stations, were computed and presented, see figures 2.14 to 2.18.

A closer analysis shows that normal beam intensity to the order of 600 W/m^2 or stronger can be expected as early as 0800 hours (also, for as late as 1600 hours) in Zim-West, roughly from late March to late October, while monthly average daily peaks of 900 - 1000 W/m^2 are not uncommon for the same period. Summer values are much lower for both cases. The above values can be revised down to 450 W/m^2 (0800 hours & 1600 hours) and peaks to the tune or 700 W/m^2 or less.

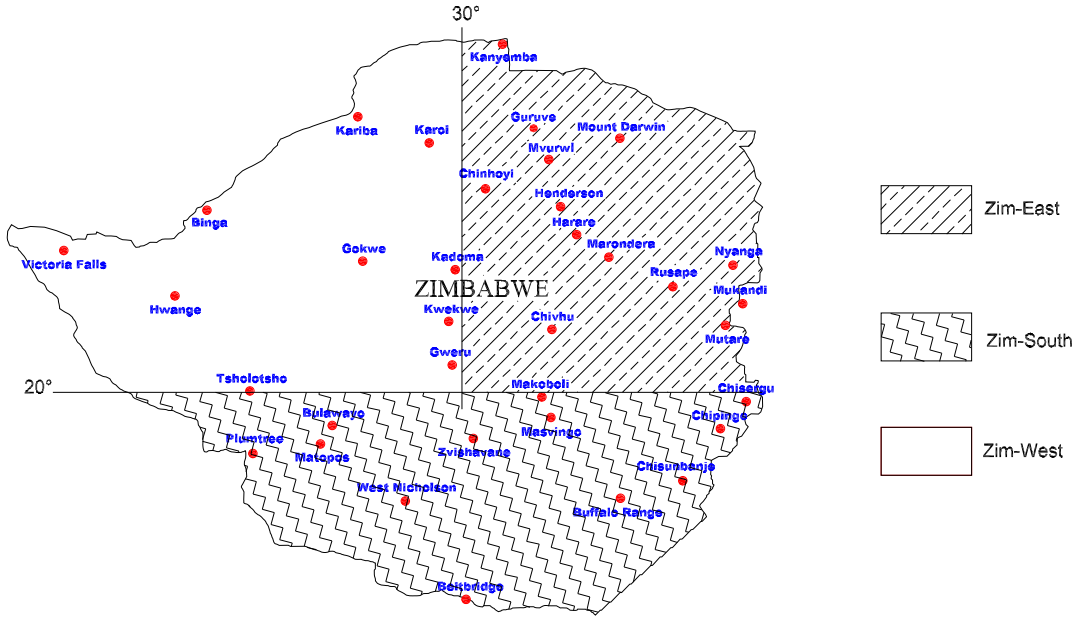

Figure 2.7: **Zim-East** - north of 20° latitude and east of 30° longitude, **Zim-West** - north of 20° latitude and west of 30° longitude and **Zim-South** - south of 20° latitude.

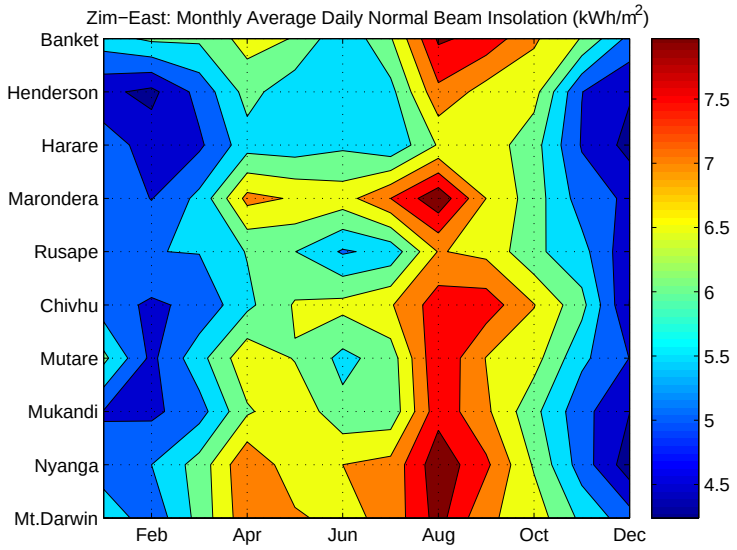

Figure 2.8: **Zim-East**: To approximate a more realistic extrapolation between stations, the arrangement is such that neighboring sites are put next to each other.

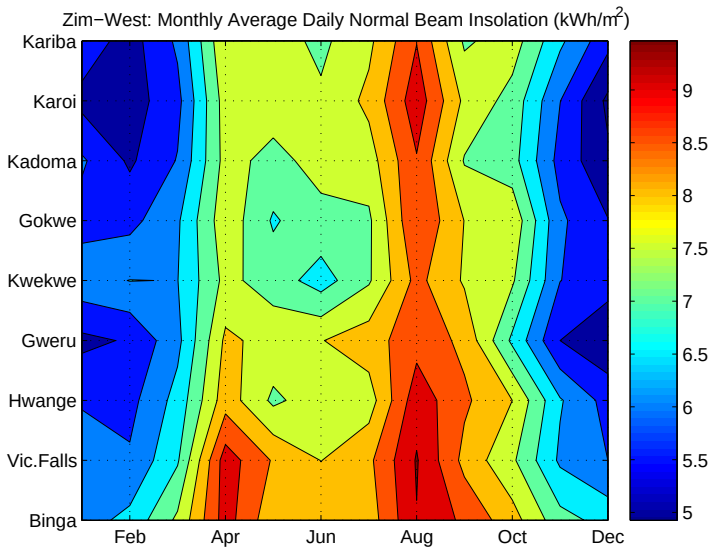

Figure 2.9: **Zim-West**: To approximate a more realistic extrapolation between stations, the arrangement is such that neighboring sites are put next to each other.

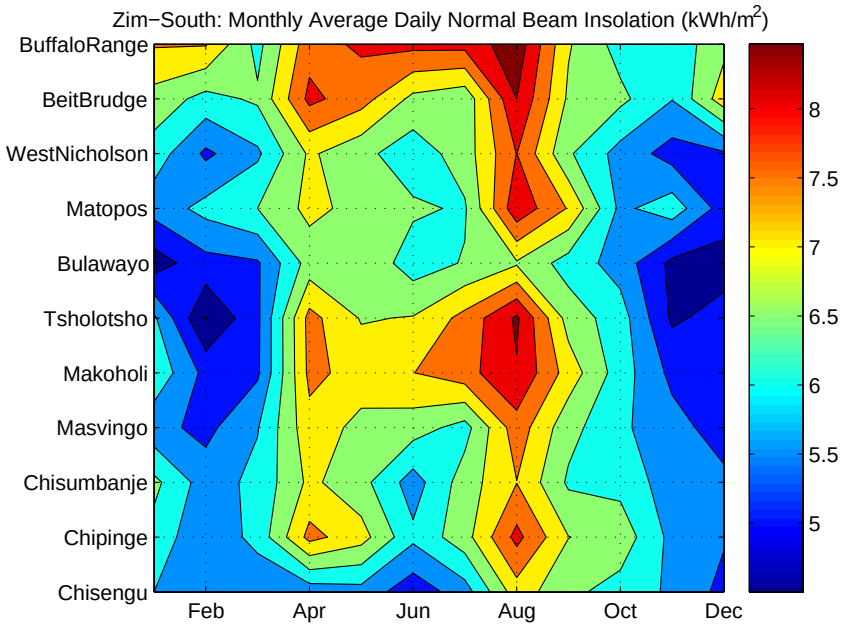

Figure 2.10: **Zim-South**: To approximate a more realistic extrapolation between stations, the arrangement is such that neighboring sites are put next to each other.

According to our findings, as depicted by the obvious trends illustrated in figures 2.8, 2.9 and 2.10, average beam insolation in Zim-West is higher and of a more stable temporal and spatial variation compared to its counterparts in Zim-East and Zim-South, (in that order). Between 0800 hours and 1600 hours, all places can expect at least 300 W/m^2 or stronger in winter, while peaks to the order of 700 - 850 W/m^2 are common during the same season. For these two regions, summer trends appear to be more erratic, a categorical characterization is therefore difficult.

2.5.2 Duration of Sunshine Hours

Apart from solar radiation data as discussed in the previous section, a knowledge on the duration of the average sunshine hours per day through out the year would be useful in our case. With the exception of Harare[5], which had daily recordings of duration of sunshine hours, only monthly average daily sunshine hours were available for the other stations. For consistency, the analysis is done according the 'solar sub-regions' described in section 2.5.1. The results for those stations from which sunshine data could be obtained are presented in figures 2.11, 2.12 and 2.13 i.e grouped according to the solar sub-regions: Zim-East, Zim-West and Zim-South respectively.

In agreement with the general findings in the previous section, it can be seen that Zim-West receives more sunshine than its counterparts. From April to October (i.e for 7 months, which is about 60% of the time), Zim-West is expected to receive at least 9.5 hours of sunshine per day. The rest of the months (Mar, Nov and Dec, equivalent to 25%) except January, receive between 7 and 9 hours of sunshine. In general, Zim-West receives at least 7 hours (or more) of monthly average daily sunshine duration for 90% of the time.

Zim-South and Zim-East exhibit the same trend as seen for Zim-West although the figures are noticeably lower. From April to October, Zim-South receives between 8 and 9 hours of monthly average daily sunshine duration while the same trend seem to extend or last until November for Zim-East. The month of January, which is normally the pick of the rain season in Zimbabwe, receives the lowest amount of sunshine for all three regions.

It is clear that any undertaking dependent on sunshine should be poised for significant back-up during the Dec-Jan-Feb period throughout the country. The results show that Zim-East, which normally receives good rain, is the worst affected especially in January. Based on the available sunshine data, the general statistics show that most areas in Zim-South receive at least 7 hours (or more) of monthly average daily

[5]Plots showing a time series (1991-2000) of the 2-day running average are presented at the end of this chapter, see figure 2.19

sunshine duration for 83% of the time, while the same figure is to the order of 75% for Zim-East.

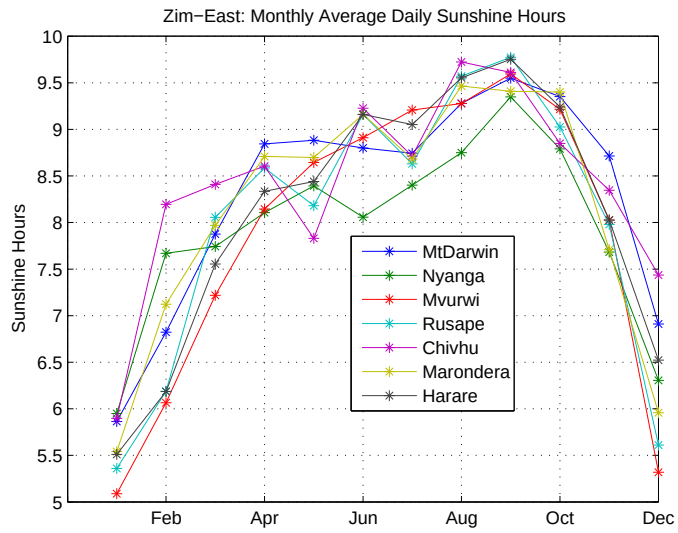

Figure 2.11: **Zim-East**: Plots showing the monthly average daily sunshine hours for some stations located in this solar sub-region. The averages were computed from data records belonging to the period: 1990 - 2000.

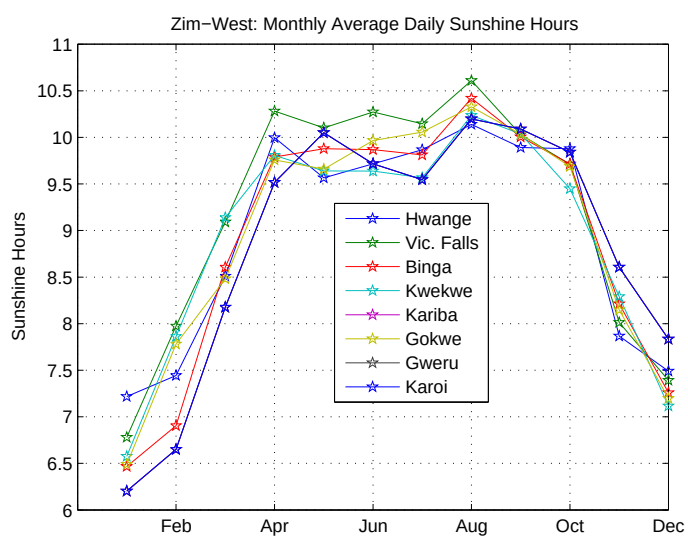

Figure 2.12: **Zim-West**: Plots showing the monthly average daily sunshine hours for some stations located in this solar sub-region. The averages were computed from data records belonging to the period: 1990 - 2000.

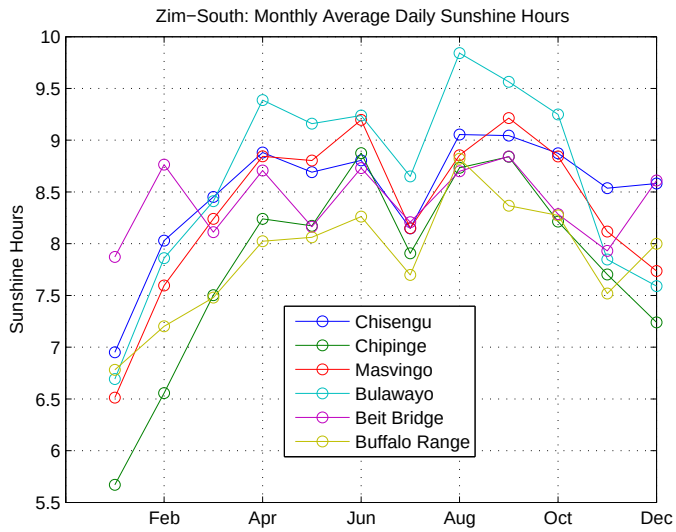

Figure 2.13: **Zim-South**: Plots showing the monthly average daily sunshine hours for some stations located in this solar sub-region. The averages were computed from data records belonging to the period: 1990 - 2000.

2.6 Chapter Summary and Conclusions

The present chapter principally discusses the solar energy resource situation in Zimbabwe based on the measurements obtained from the meteorological stations. Various diffuse models are presented and a comparison, from which one is chosen for the generation of normal beam estimates from global radiation, is done. The results are then presented at the end of this chapter in figures 2.14 to 2.18.

Based on the methodology that was applied to generate them, the normal-beam values treated in this chapter can be regarded as conservative estimates acceptable for feasibility studies in our case. Generally, normal-beam irradiation in Zimbabwe can be expected to lie between 4 and 10 kWh/m^2 per day. The wet season values are closer to the lower limit for a greater majority, while the upper limit for the various sites seem to vary from 7 to 10 kWh/m^2, apparently correlated to the sub-region in which the station in question lies.

In general, Zimbabwe has good exposure to sunshine. The analysis done on the three major solar regions show that: Zim-West receives on average, between 7 to 10 hours of sunshine for more than 90% of the time, the corresponding figures for Zim-South are 7 to 9 hours for more than 83% while Zim-East expects about 7 to 9 hours for more than 75% of the time.

Estimates of Monthly Average Normal-Beam Insolation Over Zimbabwe (kWh/m^2 per day)

Station	lat(°)	lon (°)	Jan	Feb	Mar	Apr	May	Jun	Jul	Aug	Sep	Oct	Nov	Dec
Mt.Darwin	−16.8	31.7	5.93	5.15	6.17	7.34	7.08	6.82	7.18	8.20	7.08	6.78	5.88	5.22
Nyanga	−18.4	32.7	5.13	5.50	6.21	7.43	6.68	7.00	7.16	8.33	7.60	6.44	5.26	4.21
Mukandi	−18.7	32.9	4.97	4.89	5.29	6.43	6.87	6.14	6.16	7.82	7.10	6.14	5.17	4.51
Mutare	−19.0	32.7	6.13	4.88	5.82	6.86	6.47	5.86	6.24	7.94	6.98	6.70	5.61	4.99
Rusape	−18.7	32.4	5.21	4.92	5.12	5.88	6.55	6.65	6.95	7.77	7.78	7.02	6.16	4.48
Chivhu	−19.0	30.9	5.44	5.49	5.52	6.03	6.01	5.44	5.66	7.03	6.87	6.11	5.67	4.63
Marondera	−18.3	31.5	5.44	4.98	5.63	7.15	6.95	6.78	7.50	8.37	7.00	6.24	5.27	4.90
Harare	−17.8	31.1	5.28	4.76	4.91	5.79	5.72	5.91	5.59	6.55	6.78	6.20	4.96	4.33
Henderson	−17.6	31	4.61	4.37	5.17	6.18	5.67	5.82	5.84	7.38	6.78	6.69	5.01	4.56
Banket	−17.3	30.4	5.78	6.10	6.09	6.70	6.47	5.58	6.45	8.08	7.83	7.07	6.47	5.34
Binga	−17.7	27.4	6.29	6.64	7.60	9.23	8.15	8.38	8.24	9.48	8.89	8.21	7.18	6.82
Vic.Falls	−18.1	25.9	6.32	6.07	6.94	9.26	8.45	7.99	8.39	9.54	8.35	7.59	6.41	6.00
Hwange	−18.6	27.0	5.94	5.84	6.68	8.28	7.40	7.77	7.76	9.30	8.59	8.00	6.55	5.81
Gweru	−19.7	29.9	5.38	5.55	6.36	8.10	7.83	7.98	8.27	8.82	8.38	6.90	5.50	5.11
Kwekwe	−18.9	29.8	6.33	6.51	6.49	7.64	7.26	6.77	7.44	8.65	7.94	7.57	6.01	5.71

Table 2.2: These normal beam estimates are based on meteorological data recorded between 1981 and 2000 at 30 stations across Zimbabwe. In the 2nd and 3rd columns, **lat**, **lon** and **Vic.Falls** are shortcuts for latitude, longitude and Victoria Falls respectively.

Estimates of Monthly Average Normal-Beam Insolation Over Zimbabwe (kWh/m^2 per day)

Station	lat(°)	lon (°)	Jan	Feb	Mar	Apr	May	Jun	Jul	Aug	Sep	Oct	Nov	Dec
Gokwe	−18.0	29.9	5.80	5.84	6.43	7.83	6.94	7.34	7.41	8.98	7.99	7.87	6.09	5.52
Kadoma	−18.3	29.9	6.07	5.42	6.03	7.68	7.34	7.69	7.78	8.96	7.46	7.19	5.82	5.09
Karoi	−16.8	29.6	5.35	5.26	5.85	7.74	7.76	7.58	8.12	9.29	7.89	7.31	6.01	4.89
Kariba	−16.5	28.9	5.81	5.28	6.09	7.96	7.71	7.39	7.89	8.98	7.42	7.75	6.60	5.66
Chisengu	−19.9	32.9	6.00	5.97	5.59	5.70	5.81	5.18	5.77	7.27	6.62	6.30	5.91	5.35
Chipinge	−20	32.6	6.32	5.59	6.17	7.66	7.20	6.11	6.80	8.15	7.01	6.80	5.85	5.55
Chisumbanje	−20.8	32.3	6.63	5.75	6.14	7.11	6.67	5.76	6.75	7.49	6.42	6.34	5.73	5.62
Masvingo	−20.1	30.9	5.66	5.36	5.97	7.33	6.83	6.73	6.31	7.79	6.67	6.09	5.69	5.26
Makoholi	−19.8	30.8	6.38	5.35	5.42	7.63	7.31	7.49	7.81	8.46	7.28	6.25	5.37	5.27
Tsholotsho	−19.8	27.7	6.08	4.47	5.40	7.67	6.96	7.03	7.66	8.58	6.79	6.23	4.92	5.18
Bulawayo	−20.2	28.6	4.74	5.33	5.44	6.71	6.90	6.25	6.54	6.94	6.28	5.79	4.87	4.80
Matopos	−20.6	28.7	5.70	6.16	6.50	7.14	6.83	6.58	6.44	8.35	7.46	5.88	6.29	5.26
WestNic	−21.2	29.4	6.28	5.40	5.91	7.08	6.64	6.21	6.75	8.01	6.57	5.81	5.29	5.43
Beitbridge	−22.13	30.0	6.80	6.33	6.58	8.13	7.71	6.87	6.65	8.50	6.91	6.62	6.02	7.29
Buffalo	−21.0	31.7	7.55	7.54	6.34	7.80	8.09	8.15	8.17	8.82	7.05	6.30	6.18	6.85

Table 2.3: These estimates are based on meteorological data recorded between 1981 and 2000 at 30 stations across Zimbabwe. **lat**, **lon**, and **WestNic** are shortcuts for latitude, longitude and West-Nicholson respectively.

Temporal Variations of the Normal-beam Estimates

The filled-contour images in this part give a detailed account of the expected variation of the monthly average daily normal-beam radiation for the individual locations. Such localized information is useful for engineering design and assessment of long-term performance for tracking systems as in our case. W/m^2 are used as units to express the instantaneous normal beam fluxes.

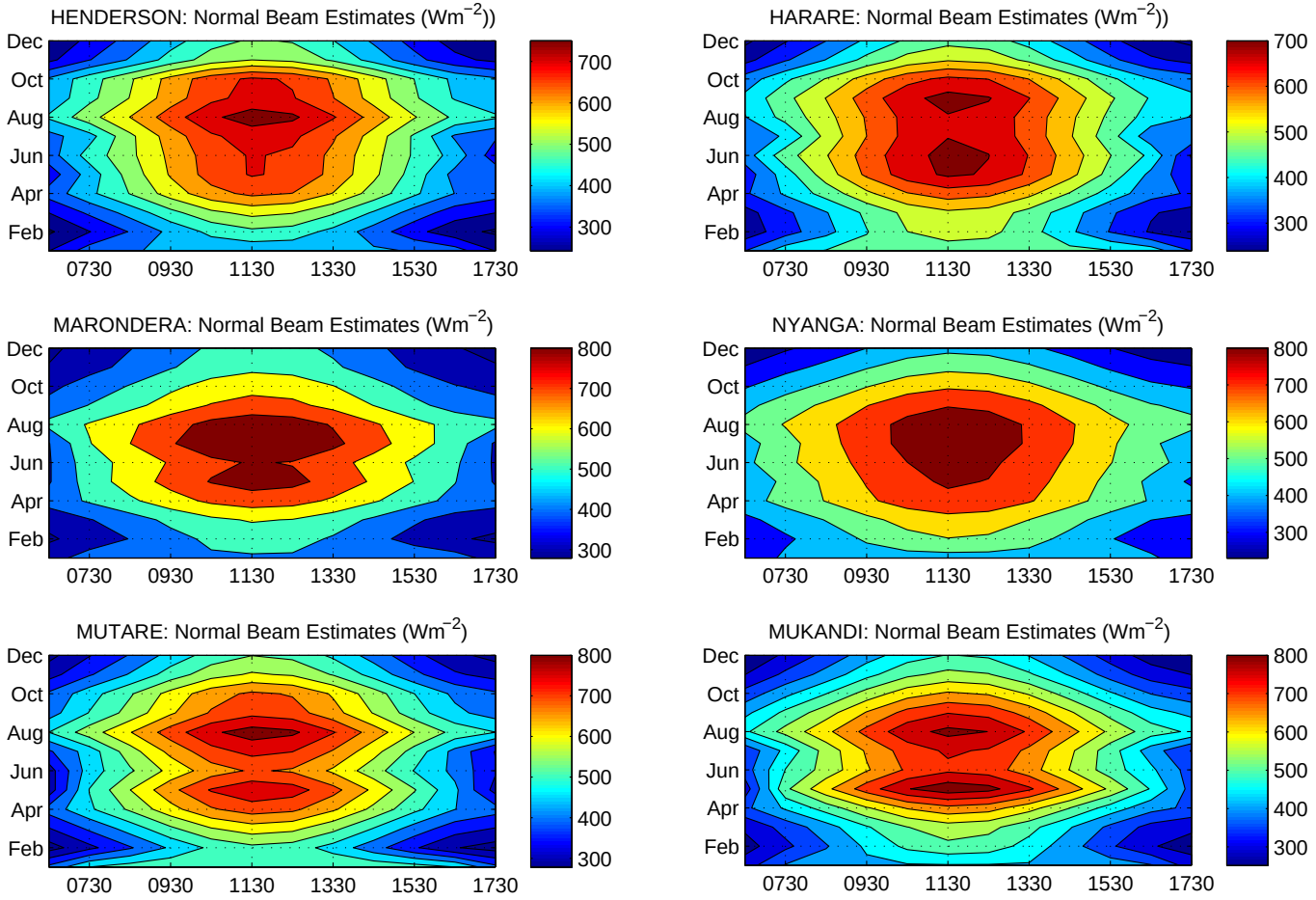

Figure 2.14: Filled contour images to illustrate the variation of the estimated beam radiation with time of the day, through-out the year, for individual locations.

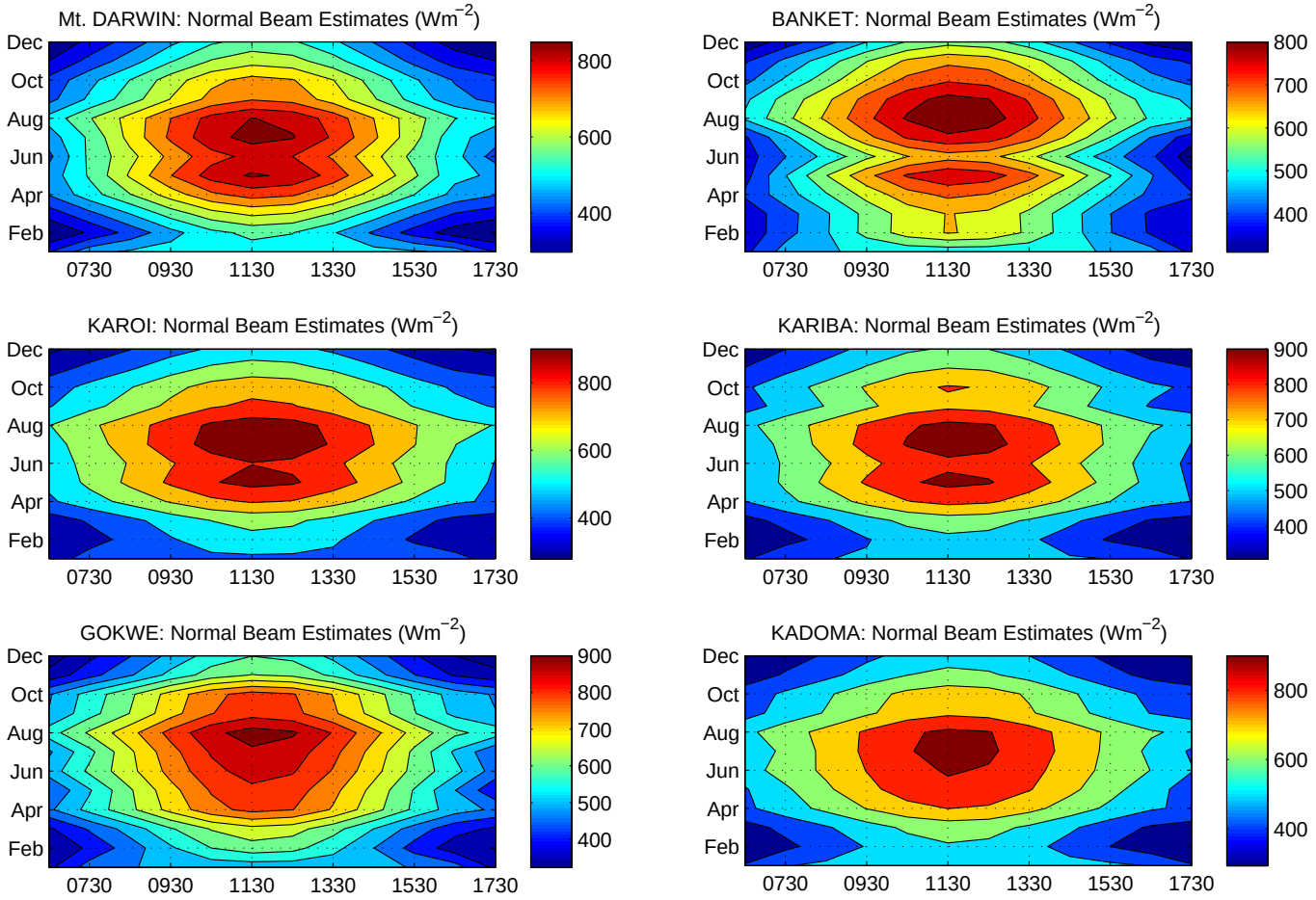

Figure 2.15: Filled contour images to illustrate the variation of the estimated beam radiation with time of the day, through-out the year, for individual locations.

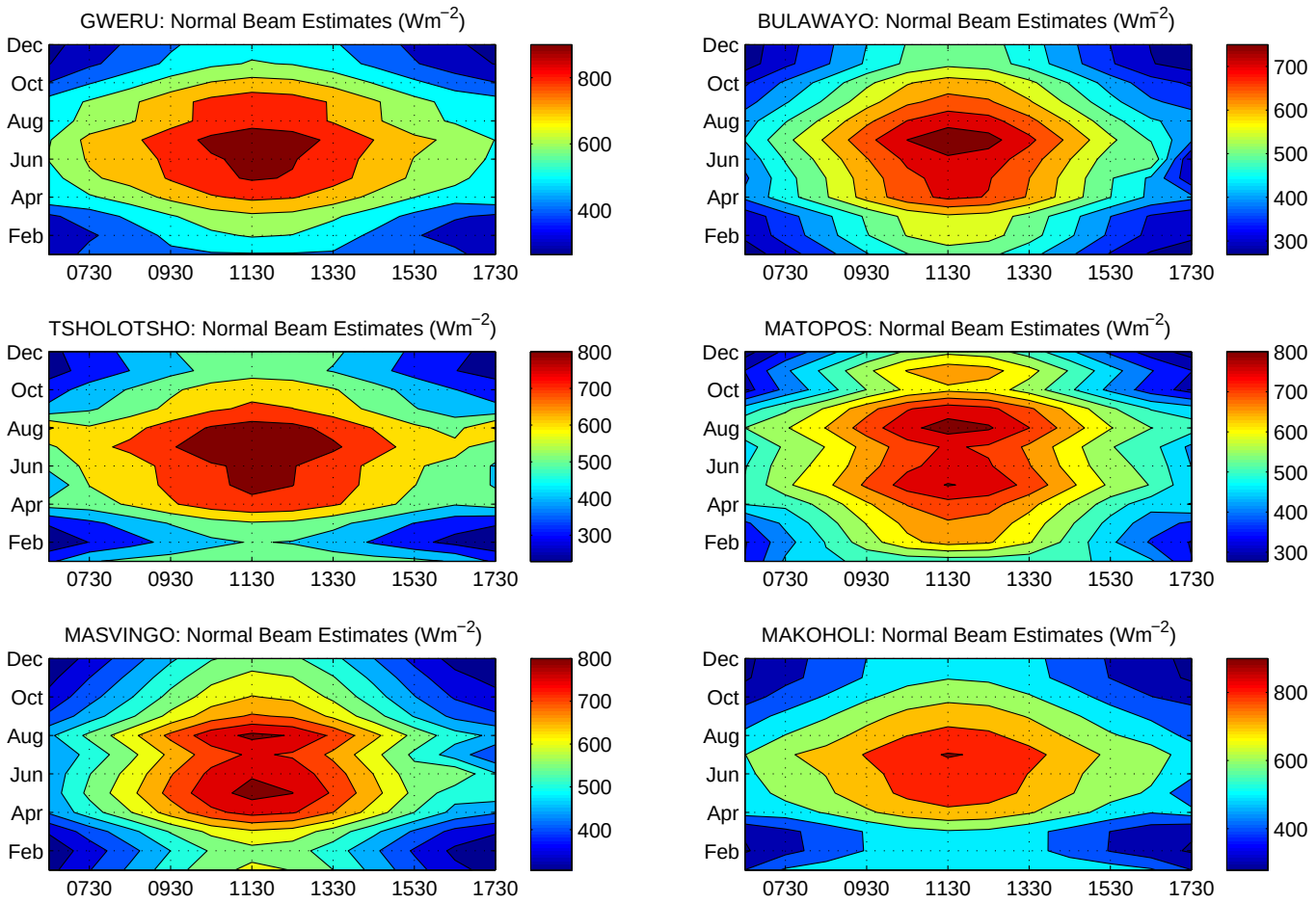

Figure 2.16: Filled contour images to illustrate the variation of the estimated beam radiation with time of the day, through-out the year, for individual locations.

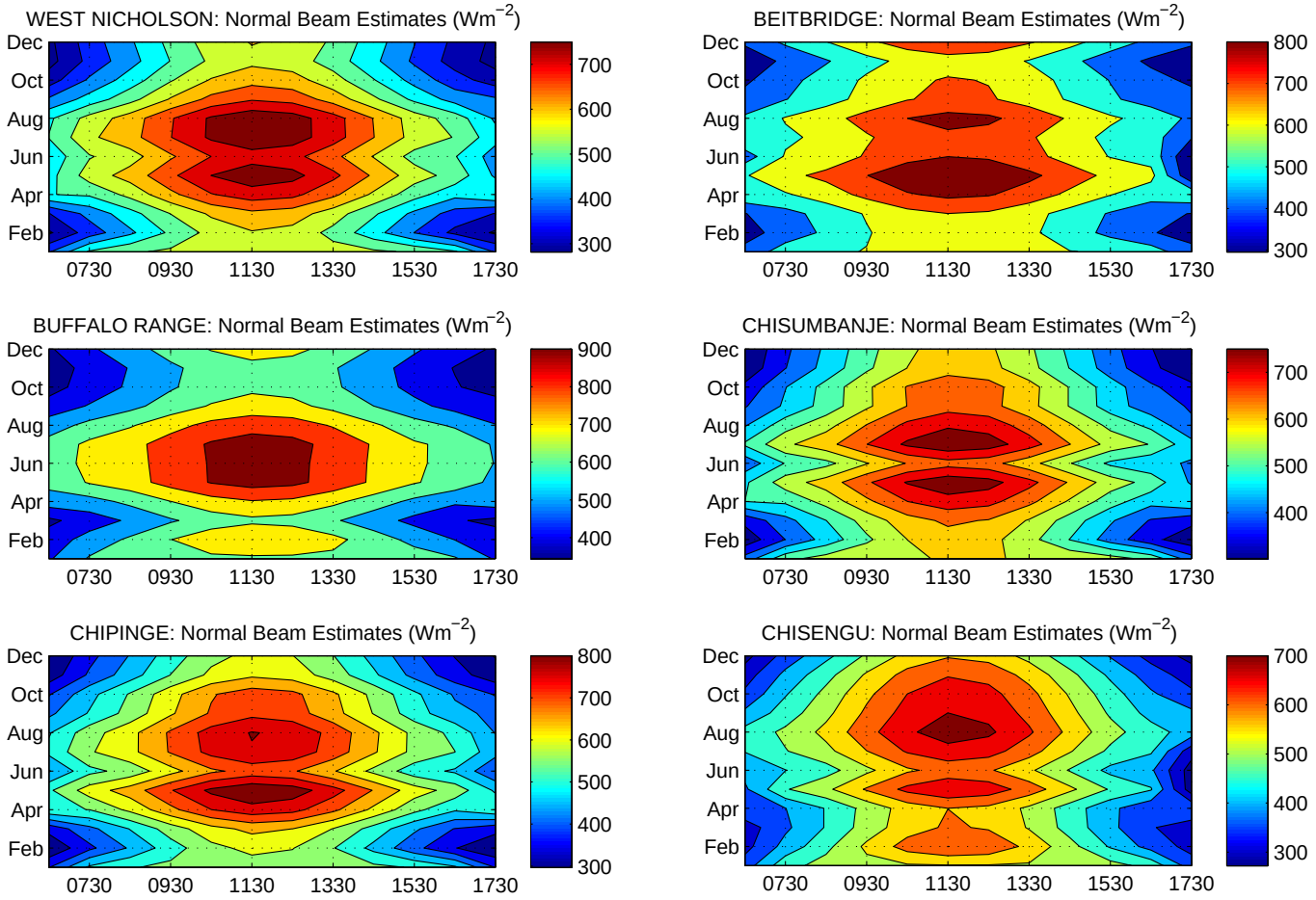

Figure 2.17: Filled contour images to illustrate the variation of the estimated beam radiation with time of the day, through-out the year, for individual locations.

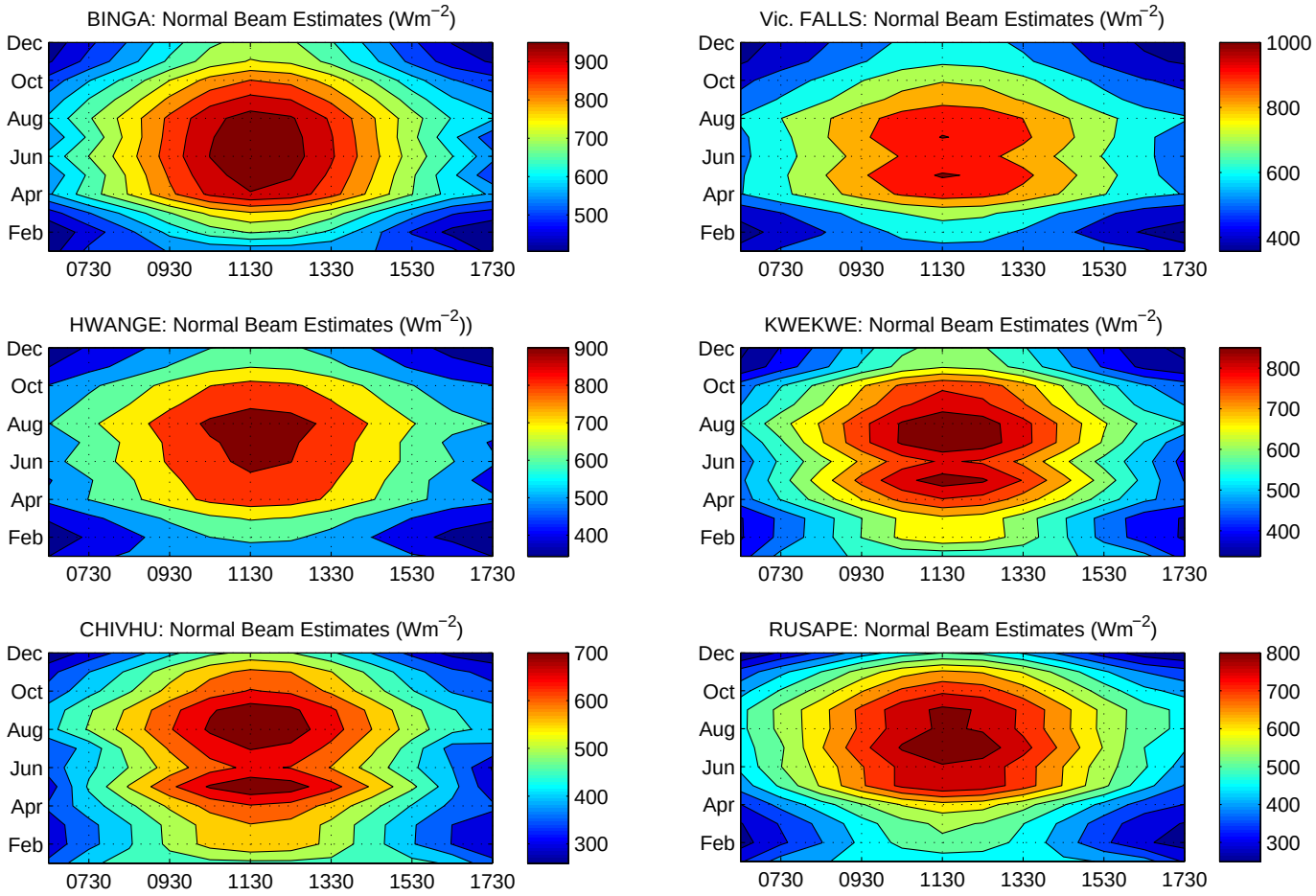

Figure 2.18: Filled contour images to illustrate the variation of the estimated beam radiation with time of the day, through-out the year, for individual locations.

Harare: Time Series For Sunshine Data (1991 - 2000)

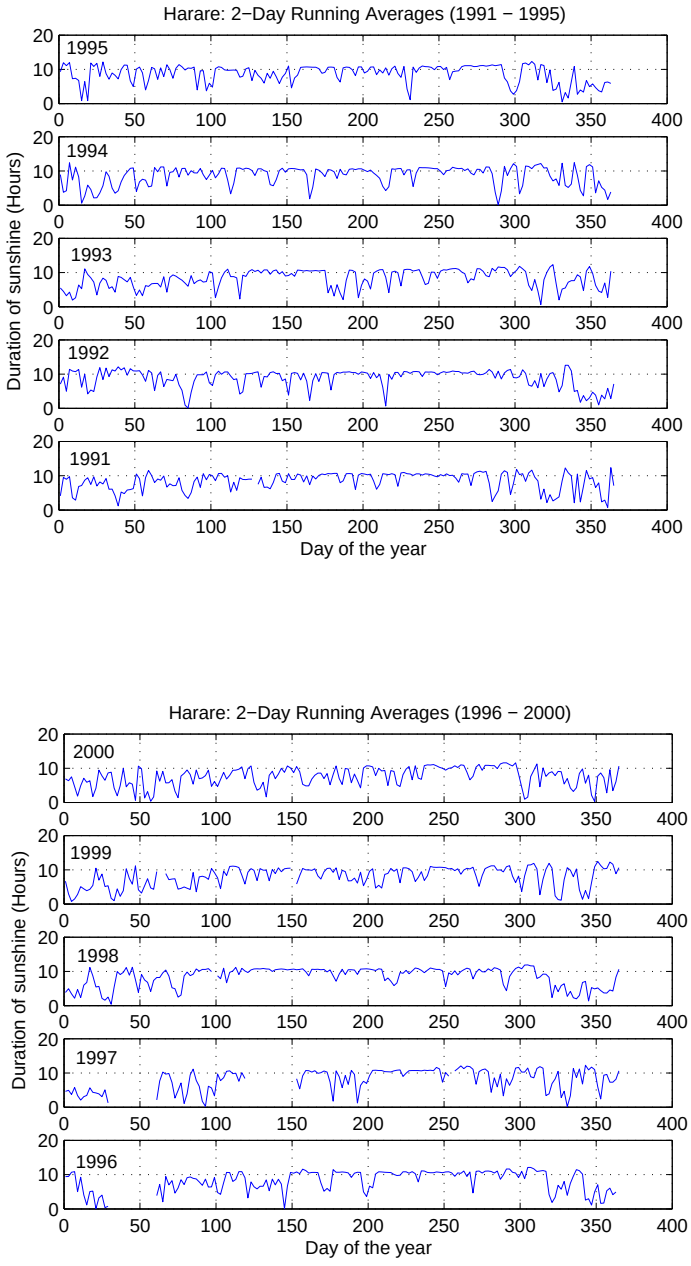

Figure 2.19: **Harare**: Plots showing time series for 2-day running averages for the duration of sunshine hours.

References

[1] ASTM, 'Standard Solar Constant Zero Airmass Solar Spectral Irradiance Tables', Standard E490 − 00, American Society for Testing and Materials, West Conshohocken, P.A, 2000.

[2] Fröhlich C and Julius L, 'World climate research programme: Revised instruction manual on Radiation Instruments and Measurements', WCRP publication series No.7, WMO/TD-No:149, October 1986.

[3] Gueymard C.A, 'The sun's total and spectral irradiance for solar energy applications and solar radiation models', Solar Energy, 76, pp 423 − 453, 2004.

[4] Siegel R, Howell J R, 'Thermal Radiation Heat Transfer', *4th Edition*, pg 420.

[5] Goswami D.Y, Kreith F, Kreider J.F (1999) 'Principles of Solar Engineering'. *2nd Edition*.

[6] Bush B.C, Valero P.J.F, and Simpson A.S, 'Characterization of Thermal Effects in Pyranometers: A Data Correction Algorithm for Improved Measurement of Surface Insolation',Atmospheric Research, 1999.

[7] Stine W.B, Harrigan R.W. 'Solar Energy Fundamentals and Design'. (1985)

[8] WMO, No.8, 'Guide to Meteorological Instruments and Methods of Observation', Secretariat of the World Meteorological Organization, Geneva, Switzerland, 1997.

[9] Lysko D.M, 'Measurement and Models of Solar Irradiance', Doctoral Thesis at NTNU, 2006:152.

[10] Major G, 'On the pointing error of pyrheliometers', Material prepared for the BSRN discussion held in Davos, Switzerland, October 1995.

[11] Iqbal M, 'An introduction to Solar Radiation', Academic Press Canada, 1983.

[12] Scharmer, K. and J. Greif (2000), 'The European Solar Radiation Atlas', Vol.1 : Fundamentals and maps and Vol.2: Data Base and Exploitation and Software, Les Presses de l'Ecole des Mines, Paris.

[13] SERI (1981), 'Solar Radiation Energy Resource Atlas of the United States,' SERI Report SERI/SP-642 – 1037, October.

[14] METEONORM (2000), Meteonorm 2000, Version 4.0 - Global Meteorological Database, James & James (Science Publishers), London.

[15] METEONORM (2003), Meteonorm 2003, Version 5.0 - Global Meteorological Database, James & James (Science Publishers), London.

[16] Hove T and Götsche J, 'Mapping Global, Diffuse and Beam Solar Radiation Over Zimbabwe', Renewable Energy 18, pp 535-556, 1999.

[17] Page J K, 'The estimation of monthly mean values of daily total short wave radiation on and inclined surfaces from sunshine records for latitudes 40° N to −40° S'. *Proceedings of the U.N Conference, New Sources of Energy*, New York, 1961.

[18] Duffie J.A and Beckman W.A, 'Solar engineering of thermal processing', 2*nd edition*, pg 51 – 56, 1991.

[19] Collares-Pereira M and Rabl A, 'Derivation of Method for Predicting Long-term Average Energy Delivery of Solar Collectors', *Solar Energy*, 1979.

Chapter 3

Paraboloidal Solar Concentrators

3.1 Introduction

3.1.1 General

Concentrating solar collectors use large specular reflectors to 'concentrate' the incident solar energy onto a smaller receiver. Taking into account the receiver material's thermal limits (i.e critical heat flux), the underlying idea is to reflect incident radiation on the collector aperture onto a receiver that is just large enough to produce heat at the desired temperature. Tracking solar concentrators are usually used where high temperature heat is required. Heat at high temperature is useful for many domestic and industrial uses [1, 2]. In the case of electricity generated from thermal sources, temperature is closely related to efficiency, in which case, elevated operating temperatures become undeniably desirable [3].

For tracking concentrators, the investment in both technology and cost, can only be justified if a high-value product is feasible. Since this project is targeted to benefit mainly Third World countries within the Sunbelt, the pursuit to minimize investment by simplifying the design and using commercially available components has high priority.

When operating under steady state conditions, solar thermal energy systems can be described as having an energy balance between what has been absorbed, removed and or the lost. In other words, if no mechanism is provided for energy removal, the receiver heat loss must balance the absorbed energy, i.e, the temperature of the receiver goes up until heat loss is equal the absorbed radiation. The temperature at which this occurs is called stagnation temperature.

If a receiver is operating below the stagnation temperature point, it implies that some means of active heat removal technique has been employed. In steady state, the useful

energy output of the receiver is the difference between the absorbed radiation and the thermal losses. A simplified mathematical expression can be written as:

$$\dot{q}_{net} = \dot{q}_{absorbed} - \dot{q}_{loss}(T)$$

For high temperature applications, heat loss is a strong function of the operating temperature, which in turn is largely determined by the rate at which the heat is removed. To ensure the removal of a large percentage of the absorbed energy as useful heat, loss from the receiver must be minimized as much as possible.

Heat loss can be reduced either by operating near the ambient temperature (e.g for low temperature flat-plate collectors) or by constructing the system such that heat loss at elevated temperatures is reduced. For solar concentrators, the most effective and common way of minimizing heat loss at high temperature, is to reduce the size of the receiver whose mode of heat loss is primarily radiative, and therefore proportional to the radiating area of the hot surface. A reduction in transient effects is implicit in the receiver by virtue of the small size.

3.1.2 Concentration Ratio

Concentration ratio is the term used to describe the amount of radiation concentration achieved by a given collector-receiver combination. It gives a practical estimate of the factor by which radiation flux on the energy absorbing surface is increased. In essence, it is a geometric ratio in that the collector aperture area (A_a) is divided by the surface area (A_r) of the receiver:

$$C = \frac{A_a}{A_r} \tag{3.1}$$

The convenience is that expressed in this form, the concentration ratio relates to heat loss [4] since it is based on the receiver area.

An alternative way of computing concentration ratio involves integrating the radiant flux incident on the receiver over its surface area and divide it by result of integrating direct beam flux over the area of the collector aperture. This method accounts for optical losses in the system. However, this method is less practical and has no direct relationship to the receiver area. As such, it does not give an insight into the thermal losses involved, which are largely dependent and proportional to the receiver area. Therefore, owing to its direct link to A_r, the geometric concentration has more relevance to this study and is therefore regarded as the default concentration ratio in this work, unless stated otherwise.

3.1.3 Theoretical Limits to Concentration Ratio

Sometimes known as the *sine law of concentration*, the (theoretical) upper limit to which a beam of light can be concentrated is given by

$$C_{max,2D} = \frac{n}{\sin(\varepsilon/2)} \tag{3.2}$$

for the two-dimensional concentrators. ε is in this case the angular size of the suns disc while n is the refractive index of the material through which light is traveling, yielding to $C_{max,2D} \approx 216$ in air [5]. However, concentration ratios to the order of 30 for two-dimensional systems are normal. For the three-dimensional type, the sine law of concentration can be stated as:

$$C_{max,3D} = \frac{n^2}{\sin^2(\varepsilon/2)} \tag{3.3}$$

which gives $C_{max,3D} \approx 46\ 000$ in air. 2-dimensional concentration needs an accurate system in order to yield high efficiency whereas 3-dimensional systems may be simplified. For purposes of interest to this work, concentration ratios to the order of 100 are reasonable.

An early impetus to the development of non-imaging optics was the realization that conventional imaging optics falls far short of the sine law limit. Unlike traditional imaging optics, the techniques involved do not attempt to form an image of the source; instead an optimized optical system for radiative transfer from a source to the receiver is the main objective. In the context of solar concentrators, the application of non-imaging optics enables the engineer to manoeuvre the receiver configuration and resultantly the concentration ratio in order to achieve the desired temperatures.

3.2 Concentrator Technology and Solar Thermal Electricity

3.2.1 General

Energy in the form of electricity is undeniably indispensable to keep rolling the wheels that move (forward) modern society in the 21st century. However, a significant part of this electricity today comes from fossil fuels. With the evidently increasing disastrous threats from global warming amid rapidly-dwindling fossil fuel resources, solar thermal electricity is arguably one of the ideal options on the table for a clean global future electricity supply.

Although it faces many competitors on the road to high volume production, the fact that it can easily be incorporated into the existing infrastructure for the conventional thermal power plants, is an important advantage. Hybridization is likely to be a useful strategy, in which case, hybridizing biomass and solar thermal power could provide reliable energy with minimal CO_2-emissions.

As a matter of fact, solar concentrators are at the centre of the conversion of the sun's energy to the much needed electricity. Typical of any evolving technology, the development and testing of new concepts, options and design possibilities by scientists and engineers, is going on in different parts of the world. Some of the said concentrator technologies have been successfully operated (and refined) over the years. It is arguable that, the experience thus far gained in their operation, renders them the potential for successful use in developing countries like Zimbabwe, for mitigating the ever-worsening energy shortage problems. The problem with Third World countries is that; only successfully tested technologies are recommended because room for trial and error is very limited financially.

Solar concentrator technology can be divided into two main types:

(i) *Low concentration non-tracking technology*, which uses all the radiation that strikes the collector aperture. Such systems have proved to be quite useful for low-temperature-heat production although they are characterized by poor energy throughput. Since we are concerned with intermediate to high temperature, a further discussion of this type is therefore not necessary. However, an in-depth treatment of this type is discussed by Duffie and Beckman [6].

(ii) *High concentration solar tracking systems*, which use only the direct beam component and circumsolar radiation. It yields to high-temperature-heat production and has been successfully used for generating electricity. Since this technology keeps improving, the scope of the present discussion will be limited to those successful concentrator-regimes that have a great potential for application in the developing countries that lie within the Sunbelt, Zimbabwe in our case. We will therefore briefly discuss the three most popularly used concentrator designs: parabolic troughs, parabolic dishes, and central receivers. Discussion on the other specialized types that include dish-thermal concentrators with secondary reflectors and solar furnaces can be found in literature, see for example [5, 7].

3.2.2 Parabolic Troughs

This is the most widely deployed type. It usually consists of long and curved mirror-surfaced troughs, which concentrate sunlight on a liquid inside a tube that runs parallel to the mirror and situated within the focal line. The usual operation is one-

axis solar tracking. A very successful example is the solar power plant (354 MW_e) at Kramer Junction, California, USA (see figure 3.1). This impressive technology was commercialized by LUZ International Inc., later succeeded by the Solel Corporation.

Figure 3.1: Picture showing parabolic trough concentrators at Kramer Junction. Source: NREL.

These parabolic mirrors are usually made of back-silvered glass to ensure high reflectance and durability. The receiver is a stainless steel tube coated with a highly selective cermet (a blend of ceramic and metal and is durable even under high temperatures) material and is usually covered by a geometrically concentric and evacuated borosilicate[1] glass tubing. Using comparable technology, CIEMAT (The Research Centre for Energy, Environment and Technology) in Spain developed a similar plant, but at a smaller scale.

3.2.3 Central Receivers

Central Receivers or Power Towers consist of a fixed receiver mounted on a tower, surrounded by a large array of mirrors known as heliostats. Each heliostat individually tracks the sun and reflects its rays onto the receiver, which then absorbs the heat. Within the receiver, a fluid (usually molten salts) convectively removes the receiver's heat energy and is then transported from the receiver to drive a turbine generator or is simply kept in storage tanks. Figure 3.2 is a picture of one such

[1]Borosilicate is a heat and chemical resistant glass.

solar-tower electric plant.

Figure 3.2: A picture of Solar Two, the prototype power tower. Some 1,926 heliostat mirrors are used to produce 10 million watts of electricity. Source: Sandia Laboratories.

Although the initial idea is understood to have been proposed by Soviet scientists in the 1960s [8], the most successful 'story' so far (on solar towers), is *Solar Two*, developed in the California, USA. This power plant features a design in which a 17-acre field of heliostat mirrors concentrate sunlight on the top of an 80 m tower.

The first version of this facility, Solar One, had a number of problems and is now known as Solar Two after it was upgraded during the early to mid-1990s. The distinctive feature of Solar Two to its predecessor was the use of molten salts as the heat transfer and storage medium. This improved efficiency significantly, as well as facilitating provision of dispatchable[2] power.

3.2.4 Parabolic Dish Concentrators

More detail will be given to the parabolic dish type since it is a component at the heart of the proposed prototype. As their name suggests, these are parabolic-shaped (ideally) point-focus concentrators that reflect solar energy onto a receiver mounted at the focal point. Parabolic dishes typically use dozens of curved reflective panels made of glass or laminated films. These concentrators are mounted on a structure

[2]Dispatchable generation refers to sources of electricity that can be turned on/off depending on demand.

that facilitates a two-axis solar tracking system. A picture of one such prototype for electricity generation is shown in figure 3.3

Figure 3.3: Picture showing a parabolic dish prototype built is Southwest USA for powering a water pump..

The concentrated sunlight at the receiver may be utilized directly by a cycle heat engine mounted on the receiver, or simply heats a fluid that is transported for storage.

3.3 Reflection From a Parabolic Dish

3.3.1 Geometry

The surface formed by rotating a parabolic curve about it's axis is known as a paraboloid of revolution, and solar concentrators having a reflective surface in this shape are often referred to as parabolic dish concentrators. The equation of the paraboloid in Cartesian coordinates with z as the axis of symmetry is:

$$x^2 + y^2 = 4fz \tag{3.4}$$

where f is the focal length. In cylindrical coordinates, with a as defined by figure 3.4, equation (3.4) becomes

$$z = \frac{a^2}{4f} \tag{3.5}$$

Now, to find the surface area of the parabolic dish, the above expression is now integrated over the appropriate limits. An arbitrary differential area strip dA_s on the paraboloid is chosen, and can be defined as

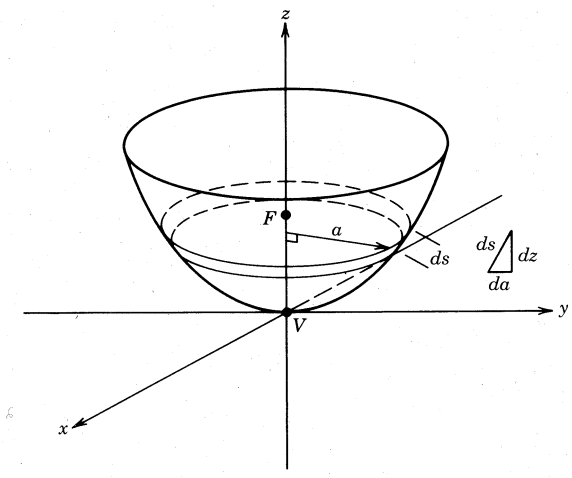

Figure 3.4: The paraboloid.

$$dA_s = 2\pi a \cdot ds \tag{3.6}$$

From figure 3.4, the differential element of the arc $ds = \sqrt{da^2 + dz^2}$, and substituting this in the above equation, we therefore get

$$dA_s = 2\pi a\sqrt{dz^2 + da^2} \tag{3.7}$$

Differentiating $z = a^2/4f$ with respect to a, we get $dz = (a/2f)da$, and then putting it in the previous equation gives

$$dA_s = 2\pi a\sqrt{\left(\frac{a}{2f}\right)^2 + 1}\ da \tag{3.8}$$

We then integrate this equation in order to get the full surface area A_s of the paraboloid:

$$A_s = \int_0^a dA_s = \frac{8\pi f^2}{3}\left\{\left[\left(\frac{a}{2f}\right)^2 + 1\right]^{3/2} - 1\right\} \tag{3.9}$$

The length of the arc s is an important design parameter. It can be obtained from $y^2 = 4fx$ (parabolic curve equation) by integrating a differential segment of this curve [9], and then apply the appropriate limits:

$$s = \left[a\sqrt{\left(\frac{2h}{a}\right)^2 + 1}\right] + 2f\ln\left[\frac{2h}{a}\sqrt{\left(\frac{2h}{a}\right)^2 + 1}\right] \tag{3.10}$$

3.3.2 Reflection From a Smooth Parabolic Surface

For a smooth (no tiles) paraboloidal reflector with parallel rays of incoming radiation, impinging at right angles to the plane containing the aperture, the reflected beam from small a surface element should ideally hit the focal point. However, due to irregularities inherent in any practical reflective surface, and also indebted to the sun's disc that has a finite angular size (or 0.53°), the image on the focal plane (which is normal to the dish axis) will like wise have a finite size. In fact, light rays reaching the earth's surface are not parallel. Implicit is the fact that, rather than all the incident rays being reflected to the focal point, the reflected rays form an image of finite size centered about the focus.

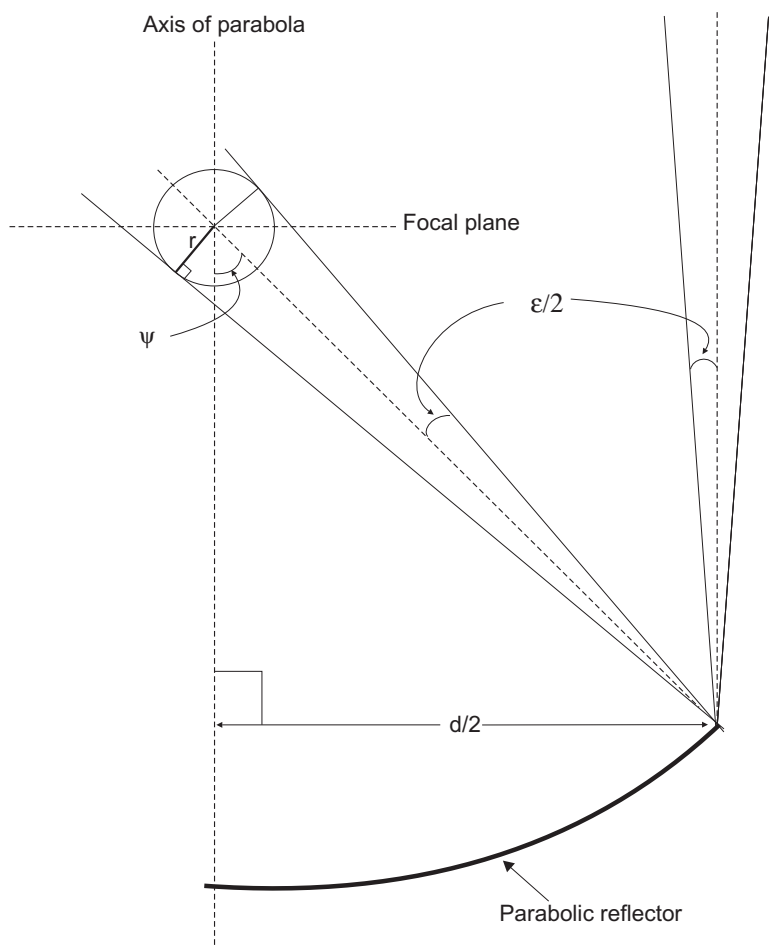

ε=32′ (The angular width of the sun's disc as seen from earth)

Figure 3.5: Schematic to illustrate the reflection of nonparallel rays by a perfect parabolic surface. The radius of the sphere just large enough to intercept all the reflected beam is defined by r as shown, and ψ is the rim angle.

Figure 3.5 tries to illustrate the reflection of nonparallel rays by a perfect parabolic surface. It can be shown that

$$r = \frac{d}{2\ \sin\psi}\ \sin(\varepsilon/2) \tag{3.11}$$

if specular reflection is assumed. With reference to the geometry shown in figure 3.5, it is evident that r defines the radius of the sphere just large enough to intercept all of the reflected beam. The corresponding statistical image at the focal plane will be an ellipse.

3.3.3 Error Considerations

The images formed by any concentrator will, of course, be degraded by any lack of perfection in the optical system. However, in practical cases, the engineer is more interested in good energy throughput rather than image quality. In fact, imaging the sun has no obvious advantage in solar conversion systems, and as Winston [5] elaborates in his paper, the requirement of an image is unduly restrictive if followed.

Therefore, some approximations, often resulting in a variety of configurations, are acceptable [10, 11]. The actual image formed by a solar collector on the focal plane, can be thought of as a summation of solar images, each to some extent distorted and or displaced by imperfections in the optical system [12].

To simplify the calculations involved in determining the errors, these can be treated as random and can thus be reported in standard deviation units. One can combine all of the source broadening mechanisms into a single Gaussian distribution as follows:

$$f(\theta_i) = \frac{1}{\sigma\sqrt{2\pi}} \exp\left(\frac{-\theta_i^2}{2\sigma^2}\right) \tag{3.12}$$

where θ_i is the incident angle relative to the concentrator pointing axis. The variance σ^2, characterizes the deviation of the effective distribution from the source and is given by

$$\sigma^2 = (2\sigma_{slope})^2 + (\sigma_{spec})^2 + (\sigma_{sun})^2 + (\sigma_{track})^2 \tag{3.13}$$

where σ_{slope}, σ_{spec}, σ_{sun} and σ_{track} are the effective root-mean-square deviations characterizing reflector surface slope error, specularity, the angular width of the sun and tracking errors respectively. The factor of two in the slope error term comes about because an error in the slope results in a change in the angle of the reflected ray by twice the amount of the slope error (see figure 3.6).

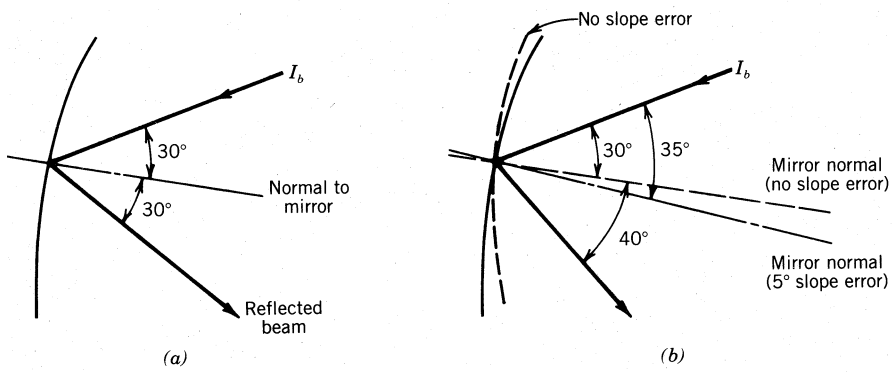

Figure 3.6: Schematic to illustrate the impact of slope error on beam deflection.

The assumption of a Gaussian sun is not physically correct because the sun has a non-normal flux distribution. However, according to Goswami[4] and or Duffie [13], the Gaussian model may be used if the variance due to the solar image spread σ^2_{sun}, is to the same order (or less) as the rest in equation (3.13), especially σ^2_{slope}, otherwise the Gaussian sun approximation should not be used. In order to facilitate the desired analysis in this section, the Gaussian sun model was adopted.

Accounting for errors whose distribution is Gaussian, gives way to the application of the popularly known and commonly used '$65 - 95 - 99.7$ *rule*' or the empirical rule. This is illustrated in figure 3.7, with μ as the mean, and σ is the deviation as usual. The area under the curve defines the relative frequency in any given range. To be specific, 68% of the observations fall within one standard deviation, while 95% fall within 2 standard deviations and about 99.7% fall within 3 standard deviations. Below the horizontal axis is a set of numbers showing measures of the standard deviation from the mean.

For practical purposes in this research, it is commendable to use ± 3 times σ to guarantee that at least 99% or more of all the incident energy is captured. Table 3.1 shows the percentage of measurements of flux falling within multiples (n) of a given standard deviation (σ) and will be used in a later section.

Standard deviation(σ)	Value of n	Percentage
± 1	2	68%
± 2	4	95%
± 3	6	99.7%

Table 3.1: Table showing the '$68 - 95 - 99.7$ rule' commonly used to describe normal distributions.

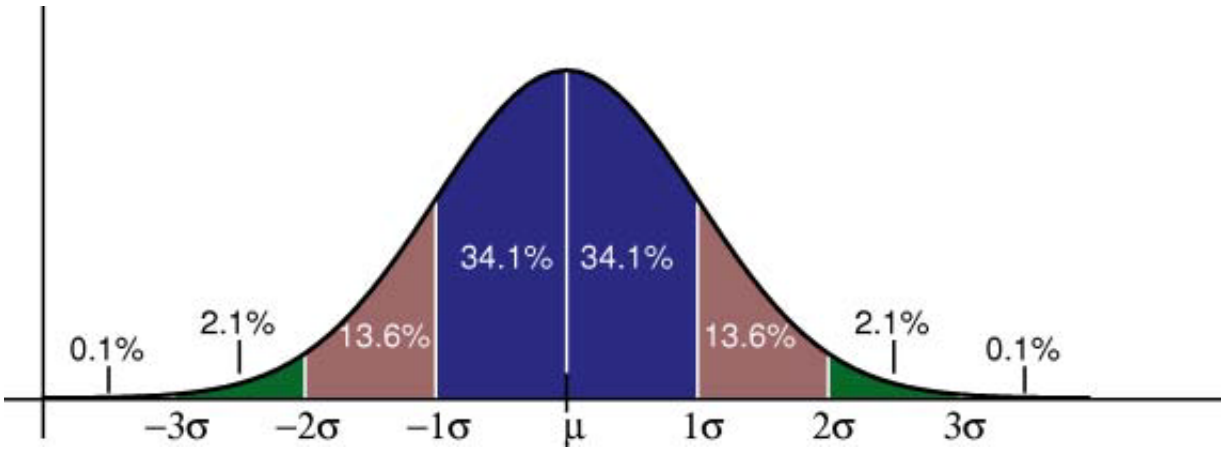

Figure 3.7: The '68 – 95 – 99.7 rule' for normal distributions. Source:Wikipedia

Based on angles and dimensions as shown in figure 3.5, it can be shown that when errors are considered, the radius of a spherical receiver that would be just large enough to intercept at least 99% of the reflected beam is given by:

$$r = \frac{d\ \sin\left(\frac{\varepsilon+3\sigma}{2}\right)}{2\ \sin\psi} \tag{3.14}$$

It is important to note that the above relationship is only valid for an ideal reflecting parabolic dish, the surface of which is assumed to be smooth and continuous. However, in most practical cases, the parabolic surface is composed of mirror tiles carefully placed and glued on the reflecting side of the paraboloid. We now discuss this case in some detail.

3.3.4 Receiver Shape and Size

In this section, we seek to discuss reflection from a parabolic surface covered with mirror tiles of finite size that tend to resemble the parabolic curvature as much as is possible. Obviously, the distribution of the radiation intensity reflected by a flat mirror tile is different from that reflected by a perfect parabolic surface. It is understood that the distribution of the intensity of the reflected beam from a flat tile can be approximated by the convolution of a Gaussian and a rectangular function. Resultantly, the dimensions and position of the tiles strongly influence the distribution of the concentrated radiation at the focal plane. Also implied is the size of the receiver.

As will be seen later (in section 3.3.6), a flat circular receiver gives better results in terms of concentration ratio when the focal-length to aperture diameter ratio is large (i.e for $f/d > 0.5$). However, a parabolic dish with a wide rim angle is in general

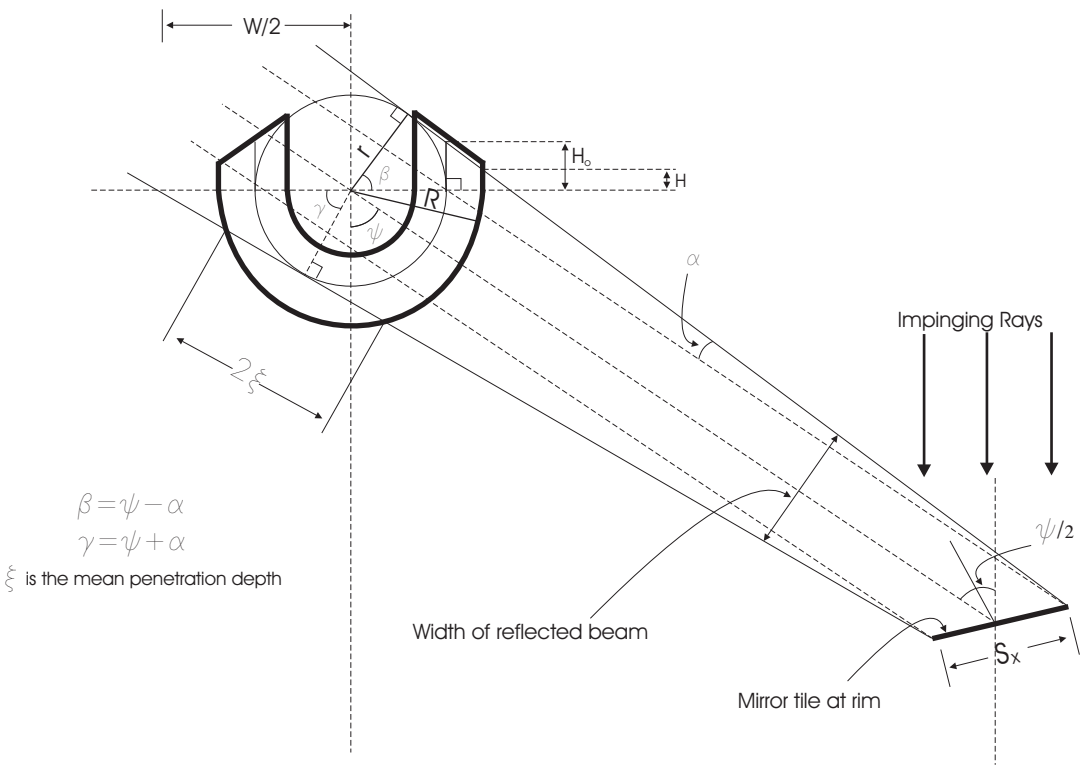

Figure 3.8: Schematic (*not drawn to scale*) to illustrate how the U-shaped configuration is expected to intercept the reflected beam for the case in which tile height of rim elements dominate. H_o and r define the height and radius respectively for a receiver that is just large enough to intercept the reflected beam. When these dimensions are adapted to accommodate the influence of the mean penetration depth ξ, the actual cylindrical height and radius are defined by H and R, see text. S_x is maximum height of rim tiles, α is the angle defining beam dispersion and ψ is the rim angle.

desirable for safety and compactness. In theory, it is convenient that the dimensions of the tiles be reduced in size from the rim towards the vertex for compact systems. The problem is that the parabolic curvature is more pronounced near the vertex for dishes with wide rim angles whilst paraboloids with a narrow rim angle are more flat. That means near-vertex tiles should be smaller compared to their counterparts at the rim if the parabolic curvature is to be followed appreciably.

Therefore, in our case where tiles of a trapezoidal shape seems ideal, the tile height of rim elements becomes the major determining factor if this height is greater or comparable to the maximum dimension of near-vertex tiles. It implies that the corresponding flat receiver at the focal plane will be very large. To counter this problem, making the receiver-limiting surface a 3-dimensional (3D) structure would be an effective approach. For this work, two 3D receiver designs, both compatible with parabolic reflector whose surface is composed of trapezoidal mirror tiles, have been proposed.

The first one has a hemispherical configuration, with the open end extended to form a cylinder. In other words, it's as if the cylinder is sitting on top of and glued to a hemispherical part of equal thickness such that their inner and outer radii coincide, thus forming U-shaped cross-sectional view when observed perpendicular to the resultant plane of symmetry. The absorbing porous material is then evenly packed between two limits, the inner and outer radii, see the illustration shown in figure 3.8.

Assuming the case where tile height of rim elements dominate, the ideal radius for both the cylindrical and spherical parts that is just large enough to intercept a beam from a tile can be approximated by

$$r \simeq \frac{1}{2}S_x \cos(\psi/2) + \left[\frac{d}{2\sin\psi} + \frac{1}{2}S_x \sin(\psi/2)\right]\tan\alpha \tag{3.15}$$

where d is the aperture diameter of the parabolic dish concentrator. The corresponding expressions for H_o and W as represented in figure 3.8 are given by

$$H_o = r\tan\left(\frac{\psi-\alpha}{2}\right) \tag{3.16}$$

$$W = \frac{2r}{\cos(\psi+\alpha)} \tag{3.17}$$

By mere intuition, it can be seen that for a receiver whose size is just large enough to intercept the reflected beam, part of the radiation at the edge of this beam will escape unabsorbed. To prevent this loss, the mean penetration depth ξ of the absorbing material has to be taken into consideration. As a result, the actual size of the receiver should be slightly bigger than that defined by r in equation (3.15), see the illustration

of the geometry in figure 3.8. It can be shown that the dimensions (the radius R of the spherical section and H, the height of the cylindrical part) that determine the actual size of the receiver, taking into account ξ can be estimated by

$$R = \sqrt{r^2 + \left(\frac{\xi}{2}\right)^2} \tag{3.18}$$

$$H = H_o - \frac{R - r}{\tan(\psi - \alpha)} \tag{3.19}$$

The second 3D receiver shape proposed for this work is essentially a portion of a cone and is illustrated in figure 3.9. Equations for theoretical imaging as those obtained for the U-shaped receiver can be derived. However, the practical design and construction of the receiver should involve experimental imaging with suitable equipment (e.g a system with laser beams) that enables scanning the reflector surface, in which case, systematic recordings of the image as a function of the position of the incoming beam have to be made.

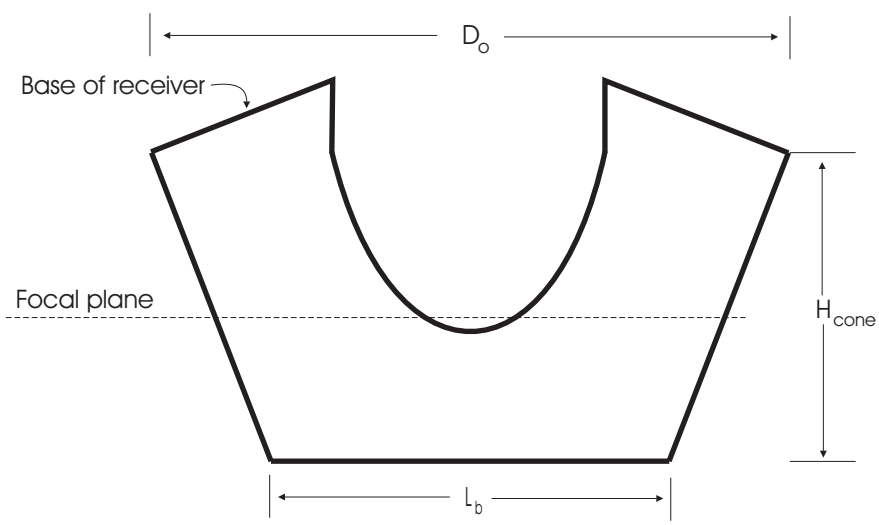

Figure 3.9: Cross-sectional view perpendicular to the plane of symmetry of the 3D receiver shape derived from a portion of a cone. This configuration is ideal for a rectangular beam in which the dimensions (essentially the diagonal in case of square tiles) of near-vertex tiles are dominant in determining receiver size.

In this second case, we will for simplicity, consider a parabolic surface covered with square tiles of equal size and of side-length L_T. This implies that the size of receiver will largely be determined by the diagonal of the tiles near the vertex, instead of tile height of rim elements as in the previous case. The cross-section of the reflected beam in a plane containing the focal point will be rectangular. At the focal plane, reflection from the tiles is expected to produce a (statistical) circular image that is

characterized by a wavy edge.

In order to estimate the size of the image, we will take a simplified approach in which the square beam at the focal plane is assumed to be coming from a slightly bigger but imaginary tile of side-length L_b, such that $L_b = L_T + \Delta L$. In this case, ΔL is additional length arising from dispersion of the real beam and can be obtained from measurements using methods suggested earlier. If it is further assumed that the beam reflected by this imaginary tile suffers no dispersion, it can be shown that the corresponding diameter D_F, of a flat receiver that would intercept such an image can be approximated by

$$D_F = L_b \sqrt{1 + \left(\frac{\cos(\psi/2)}{\cos\psi}\right)^2} \tag{3.20}$$

where ψ is the rim angle. We will consider that D_o is the diameter of the conical receiver at the base and is largely determined by the diagonal of near-vertex tiles such that for practical purposes, $D_o \simeq \sqrt{2}\ L_b$. The corresponding height of this conical configuration H_{cone}, can then be estimated as

$$H_{cone} = L_b\ \frac{\cos(\psi/2)}{\sin\psi} - \frac{1}{2}\sqrt{D_o^2 - L_b^2}\ \tan(\pi/2 - \psi) \tag{3.21}$$

The first term on the right hand side of this relationship defines beam height. The respective surface areas for both the flat and conical receivers can then be derived to get

$$A_F = \frac{\pi}{4}\ L_b^2\ \left[1 + \left(\frac{\cos(\psi/2)}{\cos\psi}\right)^2\right] \tag{3.22}$$

$$A_{cone} = \frac{\pi}{4}\ \left[L_b^2 + 2(L_b + D_o)\ \sqrt{H_{cone}^2 + \frac{(D_o - L_b)^2}{4}}\ \right] \tag{3.23}$$

3.3.5 Ray-tracing

For years, ray-tracing has been considered as a standard method for analyzing concentrators. It constitutes tracing the individual paths of a large number of rays passing through the optical system in order to find out their distribution pattern on the surface of interest. For parabolic concentrators, ray-tracing would start with the assembly of rays incident on the aperture and then determine their distribution and intensity at the receiver. Spencer and Murty [14] give a general treatment of the method, while Welford and Winston [15] present a comprehensive discussion in the solar energy context.

As interest on solar concentrating technologies grows, experience in the field has led NREL to develop a beam characterization system that measures the distribution of concentrated sunlight on a target with appreciable accuracy. Figure 3.10 shows an image of beam distribution on a target from a rectangular tile as depicted by this technology. Apart from improved accuracy, the system enables the researchers to carry out beam distribution analysis in a much shorter time.

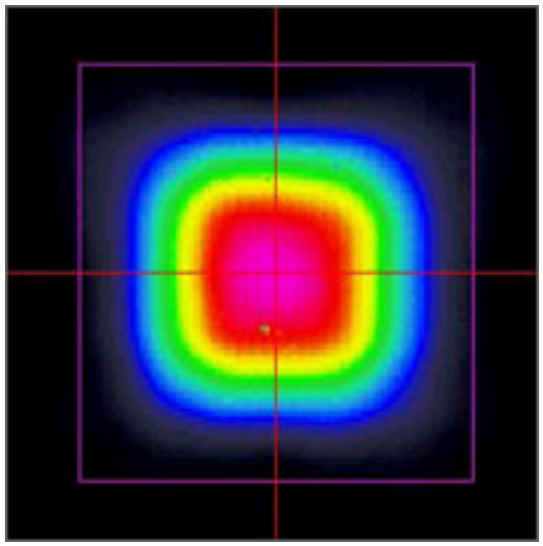

Figure 3.10: Image of radiation intensity distribution said to have been reflected from a rectangular tile as detected by the beam characterization system. NREL researchers now use this system to study the distribution of concentrated radiation on a target. Source: NREL.

The fundamental idea underlying the operation of parabolic concentrators, is to reflect the light energy incident on the collector aperture onto a receiver whose size yields to the required concentration ratio. The trade-off between a 'receiver of the wanted size' and the need to capture as much as possible (if not all) of the reflected radiation, should be balanced carefully if an optimal outcome is to be achieved.

3.3.6 Advantages of 3D Receiver Designs

Knowledge of the correlation between the preferred receiver configuration and concentrator rim angle is necessary. Solar concentrators use a truncated portion of a parabolic curve. The extent of this truncation is usually defined in terms of the rim angle or the ratio of the focal length to aperture diameter f/d, in which case, either of these linear dimensions can be used to specify the size of the curve.

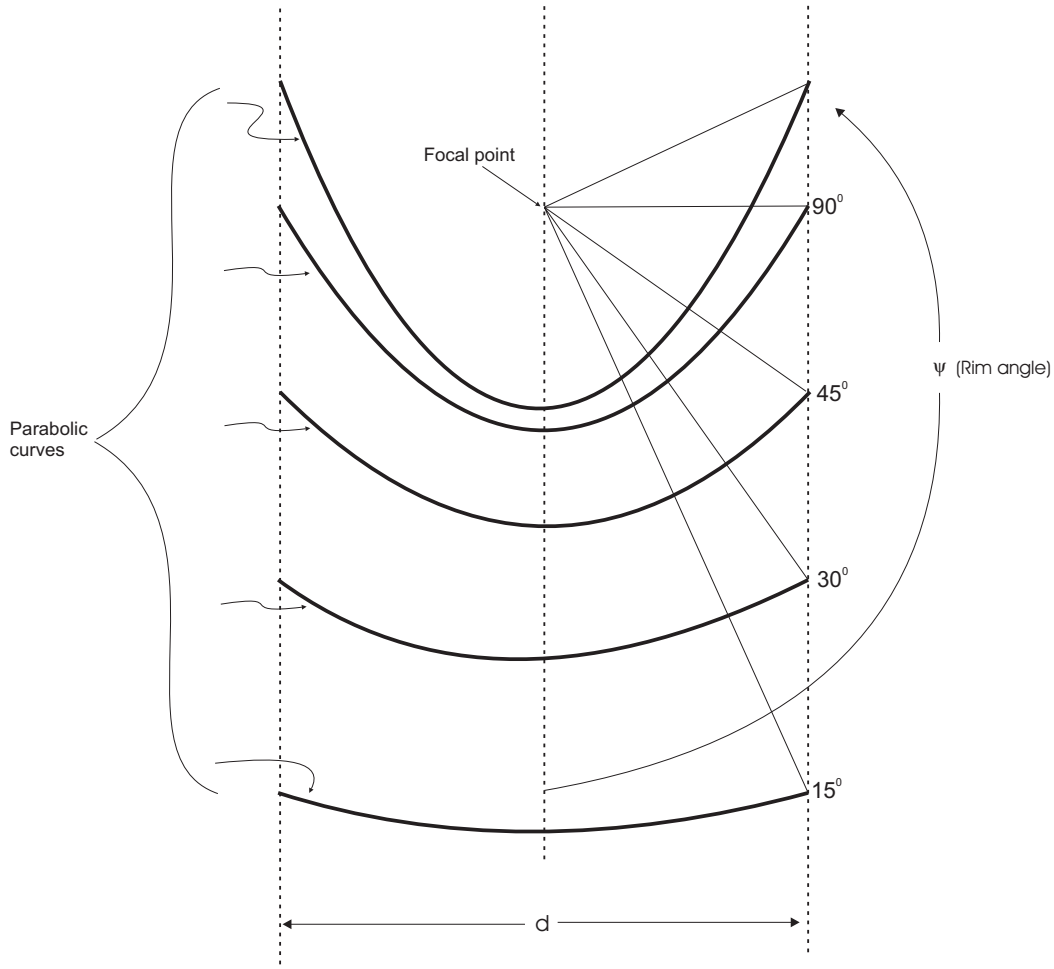

Figure 3.11: Schematic to illustrate segments of a parabolic curves having a common focal point and the same aperture diameter. The angles shown are not to scale and therefore just nominal.

Figure 3.11 shows various finite parabola having a common focus and the same aperture diameter. It can be seen that a parabola with a small rim angle is relatively flat and the focal length is long compared to its aperture diameter. As a result, the spreading of the beam is quite substantial for small rim angles.

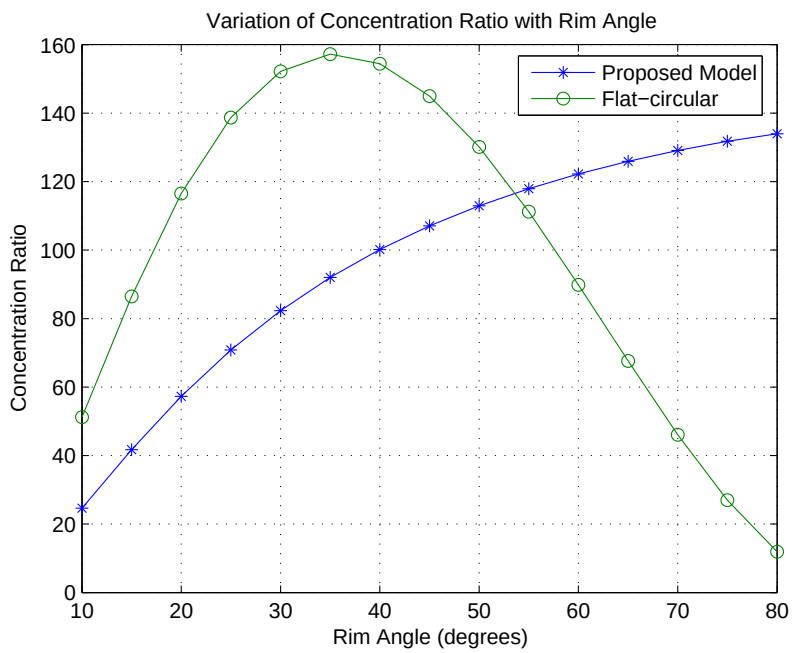

Figure 3.12: Plots showing an example of the variation with rim angle of the concentration ratios for the flat circular receiver and the proposed 3D U-shaped design, see text for the dimensions used.

As an example, based on the dimensions and angles as depicted by figure 3.8, let us consider a parabolic dish of aperture radius 1.0 m, the surface of which is covered with trapezoidal mirror tiles of maximum height 0.07 m located at the rim, and that the extent of angular dispersion can be approximated by $\alpha \simeq (\varepsilon + 3\sigma)$. The resultant variation with rim angle, of the concentration ratio for the U-shaped design is plotted in figure 3.12. The results for a corresponding flat circular receiver are also shown for comparison.

It can be seen the U-shaped 3D configuration enables the design of a compact system with high concentration ratio (i.e a low f/d ratio, see figure 3.13). By virtue of the shorter focal distance, less risk of accidental exposure to concentrated radiation is expected, implying a safer operating environment compared to longer focal lengths. More so, it should be easier to build and to 'solar-track' a system with shorter focal distance than vice versa. The focal length in a way influences significantly such operational aspects as weight of the solar-tracking unit, length of supports, even costs

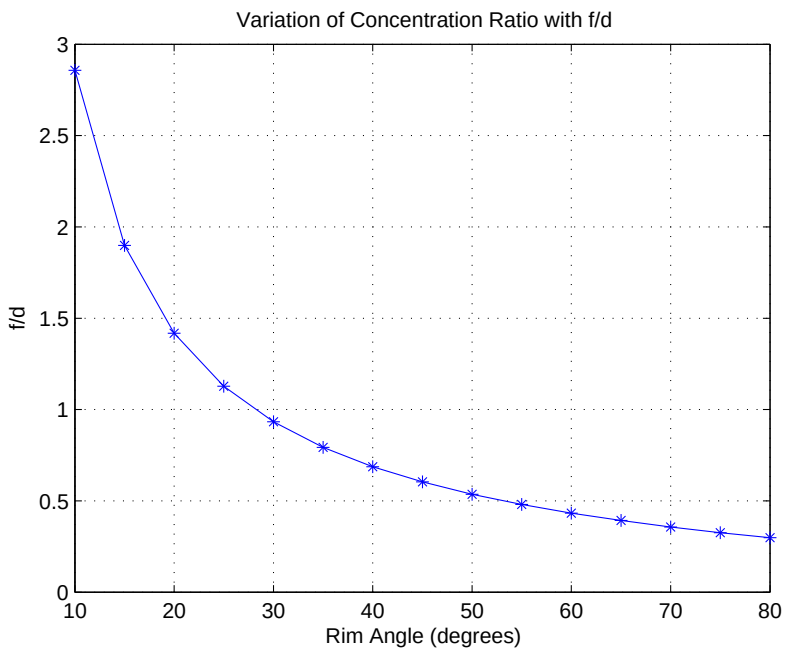

Figure 3.13: Plot showing focal length to aperture ratio as function of the rim angle.

to some extent, etc. It is therefore generally arguable that, parabolic dishes with wide rim angles (or $f/d > 0.5$) are desirable.

3.4 The Tracking Mechanism

3.4.1 Solar Geometry

For any location on the earth, the sun moves in a predictable trajectory. To specify its position, the celestial coordinates required are the solar altitude angle α_s and the solar azimuth angle γ_s, both functions of time. Literature treating solar geometry in an elaborate way is abundant, for example see[4, 6]. It can be shown that these angles are given by the following relations:

$$\sin \alpha_s = \sin \phi \sin \delta + \cos \phi \cos \delta \cos \omega \tag{3.24}$$

$$\sin \gamma_s = \cos \delta \sin \omega / \cos \alpha_s \tag{3.25}$$

where ϕ is the latitude angle, ω is the hour angle and δ is the declination given by

$$\delta = 23.45^\circ \sin\left[\frac{360(284+n)}{365^\circ}\right] \tag{3.26}$$

with n =day of the year.

The time involved is the solar time, based on the apparent motion of the sun across the sky. Solar noon is the time when the sun crosses the meridian of the observer. The relationship between solar and standard time is given by

$$Solar\ time = Standard\ time + EOT + (L_{st} - L_{loc}) \cdot 4\ min/degree \tag{3.27}$$

where L_{st} is the standard meridian for the local time zone, L_{loc} is the longitude of the location in question and EOT is the equation of time (in minutes). It is given by:

$$EOT = 9.87 \sin 2B - 7.53 \cos B - 1.5 \sin B \tag{3.28}$$

where B=360$(n-81)/364$ in degrees. EOT is essentially a correction factor that accounts for the ellipticity of the earth's motion around the sun.

The equation relating the angle of incidence of beam radiation on a surface (the aperture plane in our case), θ_i, to the other angles is given by:

$$\cos\theta_i = \cos\theta_z \cos\beta + \sin\theta_z \sin\beta \cos(\gamma_s - \gamma) \tag{3.29}$$

where β is the slope angle with respect to the horizontal, γ is the surface azimuth angle and θ_z is the zenith angle.

The apparent motion of the sun in the sky is due to two movements: a diurnal rotation of the earth around its axis and an annual revolution around the sun. Solar collectors track the sun by moving in prescribed ways that minimize the angle (θ_i) of incidence of beam radiation. This will in turn lead to the reception of maximal beam radiation on the collector surface.

Solar tracking regimes are classified by their motions based on rotation about a single axis, or about two axes. Two-axis tracking is ideal for automatic trackers that use sensors to detect the direction of maximum solar irradiance while rotation about a single axis could be of any orientation. However, in practice horizontal east-west, horizontal north-south or parallel to the earth's axis are commonly used. In our case, a polar mount tracking system in which the collector unit rotates about an axis parallel to the earth's axis is ideal. Adjustment of the declination is usually done manually every fews days. To keep the rotating collector system synchronous

to the sun's motion, traction can be provided by an electric motor or a drive based on falling weights controlled by a pendulum as in clocks.

3.4.2 Weight Driven Solar Tracking System

Since our system is meant to serve rural folks who are usually located outside the national electricity grids in developing countries, the option of using a mechanically operated solar tracking system has potential for application. A weight driven traction and control system, based on the grandfather clock principle is suitable technology. The basics of the gearbox set-up and connection to the pendulum is shown in figure 3.14.

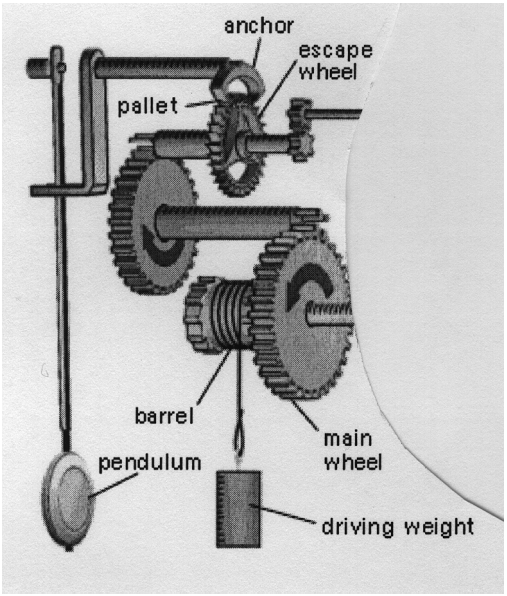

Figure 3.14: Schematic showing the basic gearbox of the tracking system based on the grandfather clock principle.

In essence, the falling weight provides the traction while the rotational speed can be controlled by the (stabilized) gravitational pendulum mechanism. A system of gears, whose combination is carefully designed to synchronize the rotation of the dish with the sun's motion are incorporated.

The escape wheel is a key component whose rotation is controlled by the pallets. During a portion of the operating cycle, it allows the pendulum to run entirely free of interference from the whole system of gears. It has specially shaped teeth, which interact with the so called the *entrance* and *exit* pallets. These pallets are attached solidly to the anchor.

As the escape wheel rotates due to traction from the falling weight, a tooth will slide across the sloping impulse plane of the entrance pallet. This will turn the pallets about their axis, which places the exit pallet into the path of the rotating escape wheel. This wheel is only able to turn freely just by a small amount (called the drop) before another tooth lands on the locking face of the exit pallet. The escape wheel is said to be locked on the exit pallet, implying that in order to unlock it, the exit pallet must move backwards by a small amount. This should be synchronized with the instant the pendulum begins to swing in the opposite direction, resulting in the release of the escape wheel, and then the cycle starts again.

3.4.3 The Pendulum

The accuracy of the proposed tracking mechanism, as-matter-of-factly depends on the pendulum, and therefore, the need for an in-depth discussion concerning some of its features is warranted. Throughout history[3], the pendulum has been the 'emblem' of horology and the epitome of clockwork regularity. What is so special about a pendulum is that it is a simple but relatively good oscillator, and as such, has been at the centre of horology for centuries until the invention of the quartz and atomic clocks.

An oscillating body such as a pendulum, which moves to and fro, is constrained by two opposing forces: inertia that tries to sustain the motion, and damping. The interplay of inertia and damping, usually in the form of either elasticity or friction, has been a source of fascination to physicists for centuries. Elasticity is characterized by a restoring force that always tries to restore a system to its resting state, whilst inertia is a property that resists change. In a pendulum, the mass is concentrated in the bob for inertia, and the force of gravity is the restoring force.

The period T of a pendulum is related to its length and the acceleration due to gravity g, and is independent of the mass of the bob. T is the time taken for two swings (left to right and back again) of the pendulum, it is given by

$$T = 2\pi\sqrt{\frac{l}{g}} \tag{3.30}$$

where l is the length of the pendulum measured from the pivot point to the bob's center of gravity. The presence of g as a variable in the above equation implies the need for gravimetric adjustments, because g slightly varies with location on Earth.

[3]Galileo conceived of a pendulum clock before he died in 1642, but it was the Dutch mathematician Huygens who actually built one in 1656.

For example, if one operates an accurate pendulum clock in Glasgow (g = 9.815 63 ms^{-2}) and then take it to Cairo (g = 9.793 17 ms^{-2}), the pendulum must be shortened by 0.23%, if accuracy is to be maintained.

The pendulum is undeniably the real source of accurate solar tracking in our case, with the rest of the mechanism subservient to its needs. The engineering task is therefore twofold: to ensure that the force needed to keep our pendulum in accurate oscillation must be delivered in extremely accurately measured amounts, and to counteract all frictional forces in the gearbox which would otherwise damp the swings. Provision to prevent any lateral movement of the driving weight is also implied. Since the setting is such that the pendulum receives the impulse periodically, errors are expected to be very small indeed.

Changes in temperature will affect the length of the pendulum, and resultantly pendulum rods made of invar, an alloy which expands and contracts very little with variations in atmospheric temperature, are highly recommended. Oscillations can also be affected by the stability of the pendulum suspension support.

The pendulum's oscillatory motion is vulnerable to changes in barometric pressure. A rise in pressure increases the density of the air and makes the bob weigh slightly less by Archimedes principle[4]. More air is set in motion by the bob, and its inertia has to be added to that of the pendulum. In other words, if frictional damping from whatever source, is very small compared with the restoring force, the pendulum will continue oscillating for many cycles without suffering detectable damping. Therefore, barometric pressure has significant influence on the period of oscillation.

It is necessary to emphasize that of prime importance in the operation of a pendulum in our case is amplitude of oscillation. The clock work system must be made in such a way that the amplitude is of the correct angular size and that its variation during operation is marginalized to zero. An alternative design, in which the pallet and escape wheel are replaced by a more robust mechanism has been developed Jørgen Løvseth and can be used to minimize effectively the variation of amplitude with time during tracking periods.

3.5 Chapter Summary and Conclusions

Parabolic concentrators for high-temperature-heat production is a known technology as evidenced by its success in major projects, some of which are discussed in section 3.2. It is suitable and ideal for use in the present research, in which case, a reflector

[4]The upthrust is equal to the weight of the displaced fluid.

whose surface is covered with carefully sized trapezoidal mirror tiles is recommended. The Gaussian distribution can be used to asses the errors in the reflected beam if the deviations arising from other sources, are to the same order as the deviation caused by the angular size of the sun's disc. The analysis done on errors shows that the system is optically very sensitive.

The concentration ratio varies with rim angle for a fixed aperture size, and resultantly different receiver configurations have different optimal rim angles. The proposed 3D receiver designs have been analyzed, compared and found to be quite satisfactory for wider rim angles ($> 55°$) as the combination allows the design of compact concentrating systems. For locations outside the electricity grids, good mechanical solar tracking can be achieved by the application of the grandfather clock principle, in which case, the pendulum component plays a major role regarding the quality of the tracking system.

References

[1] Norton B. 'Solar Process Heat: Distillation, Drying, Agricultural and Industrial Uses', *Solar Energy*, State of the Art, ISES position papers - Jeffrey Gordon(Editor), pg 497(2001).

[2] Kreith F and Kreider J.F. 'The Principles of Solar Engineering'. *Series in thermal and Fluids Engineering*, 1978.

[3] Mills D.R. 'Solar Thermal Electricity', *Solar Energy*, State of the Art, ISES position papers - Jeffrey Gordon(Editor), pg 577(2001).

[4] Goswami D.Y, Kreith F, Kreider J.F. 'Principles of Solar Engineering'. 2*nd Edition*, 1999.

[5] Winston R. 'Solar Concentrators', *Solar Energy*, State of the Art, ISES position papers - Jeffrey Gordon(Editor), pg 393(2001).

[6] Duffie J.A and Beckman W.A. 'Solar Engineering Of Thermal Processes', *2nd Edition*, 1991.

[7] Mats Ronnelid. 'Optical Design of Stationary Solar Concentrators For High Latitudes'. pg-22. Uppsala, Sweden, 1998.

[8] Vant-Hull L.L and Hildebrandt A.F. 'Solar Thermal Power System Based on Optical Transmission', *Solar Energy, 18*, 31, 1976.

[9] Stine W.B, Harrigan R.W. 'Solar Energy Fundamentals and Design'. 1985

[10] Winter C.J, Sizmann R.L and Vant-Hull(Eds) L.L. 'Concentrator Optics', *Solar Power Plants: Fundamentals, Technology, Systems economics*, (1991).

[11] Meinel A.B. 'Concentrating Collectors'. *Solar Energy Engineering*, Sayigh A.A.M (Editor), (1977).

[12] Mobarak A and Rahim A. A. 'Determination of Focal Flux Distribution of a Parabolic Dish Solar Concentrator Applying Real Shape'. *12th Annual International Solar Energy Conference, ASME*, pp 79-86, 1990.

[13] Harris J.A and Duff W.S. 'Focal Plane Flux Distribution produced by Solar Concentrating Reflectors'. Solar Energy(5), pg 403(1981).

[14] Spencer G.H and Murty M.V.R.K. 'General Ray Tracing Procedure', *J. Optical Soc. of America*, 52, 672(1962).

[15] Welford W.T and R Winston. 'Principles of Optics Applied to Solar Energy Concentrators', *The Solar Energy Handbook* (J. Kreider and F. Kreith, eds) McGraw-Hill, New York(1981).

Chapter 4

The Volumetric Fibrous Receiver

4.1 Introduction

4.1.1 General

The volumetric receiver (or absorber) concept, using ambient air to transfer concentrated solar radiation has evolved a great deal over the last few decades. For many researchers, one of the main objectives in investigating the processes or phenomena of heat and mass transport relevant to these type of receivers is the need to predict the response due to excitations imposed on the system. The response could be in the form of spatial and or temporal variations of values of state variables (e.g density, temperature, fluid-pressure) that characterize the system as a whole or part of it, depending on their relevance to the desired predictions.

However, determination of flow variables for problems involving heterogeneous porous media is generally difficult [1], even when subjected to simplifications allowing specification of the medium periodicity and or regularity [2]. For practical situations, limitations due to: irregularity of the domain's boundaries, heterogeneity of the media, irregular spatial and temporal distributions of various excitations, worsen the already daunting task of identifying pertinent heat transport mechanisms [3, 4]. Consequently, these add to the inherent complexity involved in developing a deterministic approach [5] regarding pragmatic engineering design best-suited for volumetric fibrous receivers.

As a matter of fact, the use of modeling on heat transport in porous media cannot be overstated in modern research [6]. In essence, a model is a simplified version of the real system, that satisfactorily (usually from two perspectives: details and accuracy) approximates those excitation-response relations of the system in question. The study of heat and mass transport in porous media is a rather complex subject, and as pointed out by Travkin [7], the proper form of the governing equations in

porous media is still a source of frequent discord and an area of debate, even among seasoned researchers in the field.

Therefore, implicitly there exist no unique model within the domain of volumetric fibrous absorbers. The selection or development of the appropriate model is largely subjective to the type of anticipated predictions. In solar concentrating technology, many different types of solar receivers of a porous structure have been proposed and or developed , some of which are reviewed in [8, 9, 10, 11]. A greater majority of the said models are currently in use, apparently competing yet without comparison or analysis, probably owing to the diversity of the purposes for which they are meant to serve.

4.1.2 Discretization of the Receiver Configuration

A volumetric receiver compatible with a parabolic concentrator as discussed in section 3.3.4 is now modelled. The absorbing material is a mass of evenly packed fibrous material, which is then irradiated by concentrated solar radiation from a parabolic dish collector. A possible candidate is a mass of high temperature stainless steel fibres (of diameter 0.1 mm), type: 1.4841/AISI 314 that contains 25% Cr and 20% Ni (Source: a German firm called Stax, see www.stax.de). Stainless steel can withstand temperatures of up to about 1400 ^{o}C.

Since full absorption in the solar spectrum (wavelength up to 3μ m) is of prime importance, a way of blackening (also capable of sustaining fairly high temperatures of say 600 ^{o}C) the steel fibres should be investigated. It is understood that mere heating of the fibres can blacken them to some extent, but perhaps not black enough to absorb all the anticipated wavelengths. During operation, concentrated solar radiation is essentially absorbed in a volume rather than a surface, hence, the flux densities would be spread into the depth of the absorber, thus minimizing re-radiation losses.

Air is sucked through the receiver, and is heated by convection. A hemispherical glass cover or glazing, also concentric with the outer surface of the absorber is included. To model heat transfer in the receiver, the U-shaped configuration as shown in figure 3.8 is considered. The volume of the hemispherical part of the receiver is given by

$$V_{sph} = \frac{2\,\pi}{3}(R_{out}^3 - R_{in}^3) \tag{4.1}$$

The study of what happens inside the receiver is approached by discretizing the receiver configuration into equal volume-elements (ΔV_i) which we will call *cells*. It is assumed that each cell can be represented by unique temperature, hopefully equal to the cell's mean temperature. The total number of these cells into which V_{sph} is

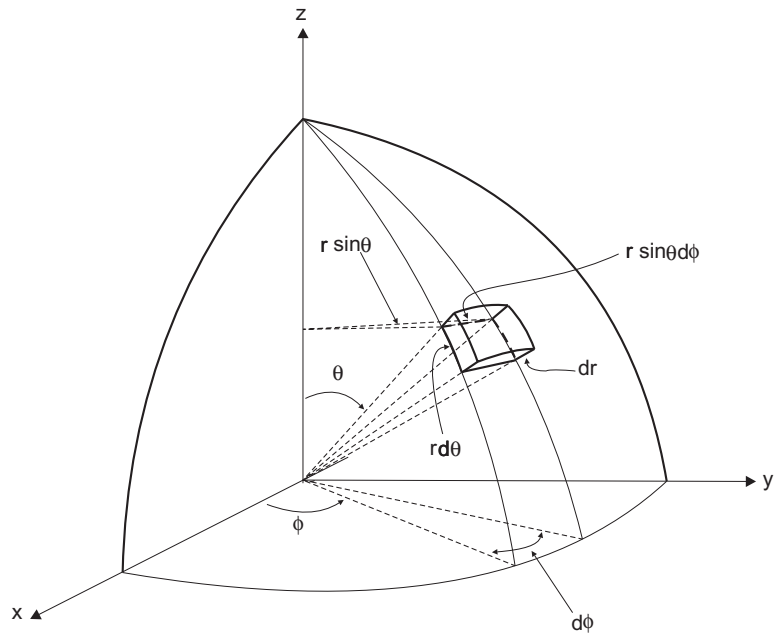

Figure 4.1: Spherical Polar Coordinates.

divided is equal to $(N_r \cdot N_\phi \cdot N_\theta)$, divisions in r, ϕ and θ respectively as presented in the spherical coordinate system shown in figure 4.1. For convenience, the volume of a hemispherical sub-division of the receiver, containing cells located at the same radii can be determined as

$$V_n = \frac{2\,\pi}{3}(R_{n+1}^3 - R_n^3) \tag{4.2}$$

Starting the indexing from the inner side, the intersection radii of the sub-divisions can be determined by rearranging the above equation to give

$$R_{n+1} = \left(\frac{3}{2\pi}\,V_n + R_n^3\right)^{1/3} \tag{4.3}$$

chosen in a manner that will make all sub-divisions to be of equal volume (i.e $V_n = V_{sph}/N_r$). The resultant typical volume element in the spherical part will look as that shown in figure 4.1. The intersection radii between hemispherical sub-divisions as determined by equation 4.3, as well as the corresponding azimuthal divisions, are also used and set to be coincident with their respective counterparts in the cylindrical section. The height of volume element situated in the cylindrical section is given by H/N_z, i.e N_z is the number of divisions in H.

The general picture is that all elements in the hemispherical section have the same volume, implying that Δr varies with depth from one sub-division to the next. The

same applies for the cylindrical section. In other words, successive values of Δr decrease outwards as cell surface increases. The straight line segment S between any two randomly chosen cells located at $A(x_i, y_i, z_i)$ and $B(x_j, y_j, z_j)$ is given by:

$$S = \sqrt{\Delta x^2 + \Delta y^2 + \Delta z^2}$$

where
$\Delta x = x_j - x_i = r_j \sin\theta_j \cos\phi_j - r_i \sin\theta_i \cos\phi_i$
$\Delta y = y_j - y_i = r_j \sin\theta_j \sin\phi_j - r_i \sin\theta_i \sin\phi_i$
$\Delta z = z_j - z_i = r_j \cos\theta_j - r_i \cos\theta_i$

Because of azimuthal symmetry, radiation exchange can be calculated for cells within a representative slice of the absorber, conveniently located at $\phi = 0$ in order to simplify computations for Δx and Δy. By choosing N_ϕ to be an odd number, we need only to calculate radiation exchange with cells located within $(N_\phi - 1)/2$ slices. If cells within the representative slice located at $\phi = 0$ are regarded as reference cells, then calculations for radiation exchange has to be done with each of the cells in the following slices: $i = 2...(N_\phi - 1)/2$. The effect is to reduce the number of computation by a factor of two (and therefore greatly reducing computation time), in which case, the other half can be accounted for using azimuthal symmetry.

For surfaces in radiation exchange, orientation of the other element with respect to the surface normal is important. As will be seen later, some of the calculations in section 4.5 require the knowledge of the angle between the surface normal and vector joining the elements of interest. The angle of interest, in this case, can be determined using dot product.

Let $\overrightarrow{r}_i$ be the position vector for point A, and like-wise $\overrightarrow{r}_j$ for point B. Also, let $\overrightarrow{S}$ be a vector such that

$$\overrightarrow{S} = \overrightarrow{r}_j - \overrightarrow{r}_i$$

If $\overrightarrow{n_i}$ is the normal at the surface of concern, then applying the dot product we get

$$\cos\theta_i = \frac{\overrightarrow{n_i} \cdot \overrightarrow{S}}{|\overrightarrow{n_i}||\overrightarrow{S}|}$$

4.1.3 Radiation Exchange Via the Central Opening

To find out whether the radiation hits the central opening or not before it reaches the cell in question, let's consider two cells as illustrated by figure 4.2, located at $A(x_i, y_i, z_i)$ and at $B(x_j, y_j, z_j)$, whose position vectors can be expressed as

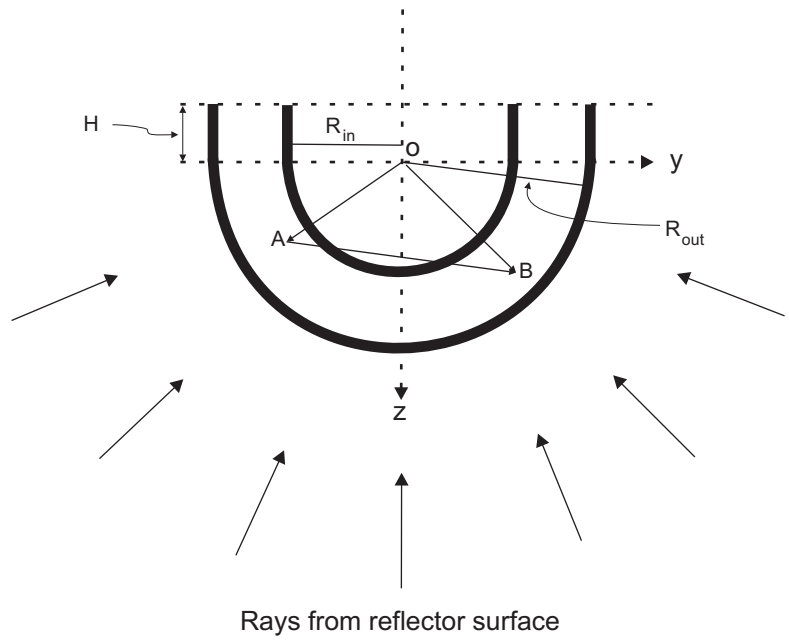

Figure 4.2: A schematic to illustrate a cross-section of the absorber in the x-z plane.

$$\overrightarrow{OA} = \overrightarrow{r_i}, \qquad \overrightarrow{OB} = \overrightarrow{r_j}$$

Also, as previously assumed, let $\overrightarrow{S} = \overrightarrow{r_j} - \overrightarrow{r_i}$, such that

$$\overrightarrow{r} = \overrightarrow{r_i} + \varepsilon \overrightarrow{S} \qquad \varepsilon \in \{0, 1\}$$

meaning that $\overrightarrow{r_j} = \overrightarrow{r_i} + \overrightarrow{S}$ when $\varepsilon = 1$. If $\overrightarrow{S}$ crosses the central spherical opening, there are two points where $|\overrightarrow{r}| = R_{in}$ (where R_{in} is the inner radius of the absorber). Expressing this concept mathematically we get

$$R_{in}^2 = \overrightarrow{r}^2 = (\overrightarrow{r_i} + \varepsilon \overrightarrow{S})^2, \qquad \Rightarrow \qquad \varepsilon^2 + 2\varepsilon \frac{\overrightarrow{r} \cdot \overrightarrow{S}}{S^2} + \frac{r_i^2 - R_{in}^2}{S^2} = 0 \tag{4.4}$$

In essence, the above expression is a quadratic equation, and hence, the use of the quadratic formula is implied in solving for ε:

$$\varepsilon = -\frac{\overrightarrow{r} \cdot \overrightarrow{S}}{S^2} \pm \sqrt{\left(\frac{\overrightarrow{r} \cdot \overrightarrow{S}}{S^2}\right)^2 - \left(\frac{r_i^2 - R_{in}^2}{S^2}\right)} \tag{4.5}$$

This problem is of the form $\varepsilon = -a_1 \pm \sqrt{(a_1)^2 - b}$, therefore an acceptable solution is possible when $(a_1)^2 > b$, yielding to two values, ε_1 and ε_2, where by definition, both must be elements of $\{0, 1\}$. Once ε_1 and ε_2 are established, computations to determine the corresponding optical paths before and after the hollow zone are fairly easy.

4.2 Variation of Air Velocity

By virtue of the spherical geometry of the absorber, sector-wise flow is assumed for the air. At steady state, the difference between the incident power and the radiative losses constitutes the power picked up by the convective fluid, air in our case. An energy balance estimate for any spherical sub-division at steady state, can be written as

$$\dot{m}c_p\Delta T = P_{incident} - P_{loss} \tag{4.6}$$

where $\dot{m}$ is the mass flow rate, ΔT the temperature difference between the incoming and outgoing air, and P is the power. The mass flow rate $\dot{m}$, can be used to derive an analytical tool to model the variation of air-velocity as it moves in sector-wise flow towards the central suction zone of the receiver. The mass flow rate is given by:

$$\dot{m} = \rho A u \tag{4.7}$$

where $A = 2\pi r^2$ for the hemispherical section, u is the air velocity and ρ is the fluid density. For constant mass flow rate and assuming smooth flow across the hemispherical section, the radial air-velocity $u(r)$ depends on fluid density $\rho(T)$ and radius r, and can be approximated by:

$$u(r) = \frac{\rho_o}{\rho(T)} \left(\frac{R_{out}}{r}\right)^2 u_o \tag{4.8}$$

for the spherical part. Estimating the dependence of fluid density on temperature by $\rho(T) = \rho_o \frac{T_o}{T(r)}$ yields to

$$u(r) = \left(\frac{R_{out}}{r}\right)^2 \frac{T(r)}{T_o} u_o \tag{4.9}$$

Under similar conditions and following the same procedure, the cylindrical counterpart $u'(r)$, is given by the following expression:

$$u'(r) = \frac{R_{out}}{r} \frac{T(r)}{T_o} u_o \tag{4.10}$$

For both the spherical and cylindrical sections of the absorber, as $r \rightarrow R_{in}$, the air is expected to even out the temperature differences as it accelerates towards the central zone of the absorber.

4.3 Heat Transfer from the Fibres to Air

The convective heat transfer coefficient h, practically represents the thermal resistance of a relatively stagnant layer of fluid between the heat-transfer surface and the

fluid medium. Since the spacing between the fibres is large compared to d_f, single fibres can be modeled as individual cylinders [12], and thus making adaptation of the approach used by McAdams [13] relevant and convenient in estimating the average heat transfer coefficient. Holman[14] and McAdams give detailed descriptions of air-flow across single cylinders. A fit to data by Løvseth [15] based on McAdams' findings, yields to the following parameterization of the average film coefficient:

$$h = \Omega u^n {d_f}^{n-1} \qquad (n = 0.28) \tag{4.11}$$

For atmospheric air at 293.15 K ($20°C$), the constant $\Omega = 0.52$, increasing with the order of 10% per 100 K temperature rise. Adapting this relationship to incorporate the effects of any such temperature changes, a more general expression for a cell i, in our case, will be given by:

$$h_i = 0.52[1 + 0.001(T_i - 293.15)]\ u_i^n\ {d_f}^{n-1} \tag{4.12}$$

The volumetric heat transfer coefficient $h_{v,i}$, can then be computed as

$$h_{v,i} = n_f\ \pi d_f L\ h_i \tag{4.13}$$

where n_f is the number density of fibres of length L and diameter d_f, see section 4.5.1. Therefore, the convective heat flux density q_i'', for a typical cell can be determined by:

$$q_i'' = h_{v,i}(T_{fi} - T_i) \tag{4.14}$$

Cross flow is assumed, and for absorption, fibres are being treated as single cylinders of length equivalent to $L\cos\theta$ at right angles to the incoming radiation and to the air current, in which case, the ratio[1] of the convection surface to the absorbing surface (let's call it $Ratio^*$) is equal to 2π i.e

$$Ratio^* = \frac{\pi d_f L}{d_f \bar{L}_\perp} = 2\pi$$

Thus, the convection surface is at least six times more than the absorbing surface. The possibility of achieving a deeper penetration coupled with a fairly high $Ratio^*$, has influenced our choice: a fibrous volumetric absorber. With d_f to the order of 0.1 mm or less, the establishment of thermal equilibrium between the fibres and the air is expected to be rather fast. As a result, randomly oriented fibres will not change the general picture very much.

[1]The absorbing surface is equal to $d_f \bar{L}_\perp$, while the convection surface is given by $\pi d_f L$. Note that $\bar{L}_\perp = L/2$, see section 4.5.1.

4.4 Drag and Blow-power

An object will experience the force of drag due to a fluid in which it is moving through or vice versa. The equation of the force F_D on a moving object (fibres in our case) due to a fluid is given by:

$$F_D = \frac{1}{2}u^2 \rho A' C_D \tag{4.15}$$

where A' is the area of the projection of the object on a plane perpendicular to the direction of motion , u is the velocity of the fluid relative to the object, ρ is the fluid density and C_D is the drag coefficient. The drag coefficient varies depending on the flow regime, shape of the object and is found by experiment. In general, C_D is a function of the following dimensionless parameters: the Reynolds number (Re), Mach number (Ma), Froude number (Fr), *shape* and relative surface roughness (ζ) of the object. Mathematically, we can express this dependence as

$$C_D = f(shape, Re, Ma, Fr, \zeta)$$

Consistent with the approach used in earlier sections, in this discourse fibres are treated as smooth-faced cylinders. Such an approximation takes care of the *shape* and ζ in above relationship. The Ma concept is mostly used to characterize objects traveling at high speed in a fluid, while Fr gives a measure of wave celerity (the speed of individual waves) and or how flow reacts to perturbations. Consequently, both parameters are not relevant to the present context.

This leaves the Re as the main parameter that influences the value of the drag coefficient applicable to our absorber system [17]. The main categories of Re dependence are: very low Re flow, moderate Re flow (laminar boundary layer), and very large Re flow (turbulent boundary layer), see a textbook by White [18] for an elaborate discussion. The dependence of C_D on the Reynolds number is shown in figure 4.3. Therefore, the power required to overcome the aerodynamic drag is given by:

$$P_D = F_D \cdot u = \frac{1}{2}u^3 \rho A' C_D \tag{4.16}$$

It is important to note (for practical purposes) that the power needed to push an object through a fluid increases as the cube of the velocity. In other words, exerting four times the drag force at twice the speed, requires eight times the power.

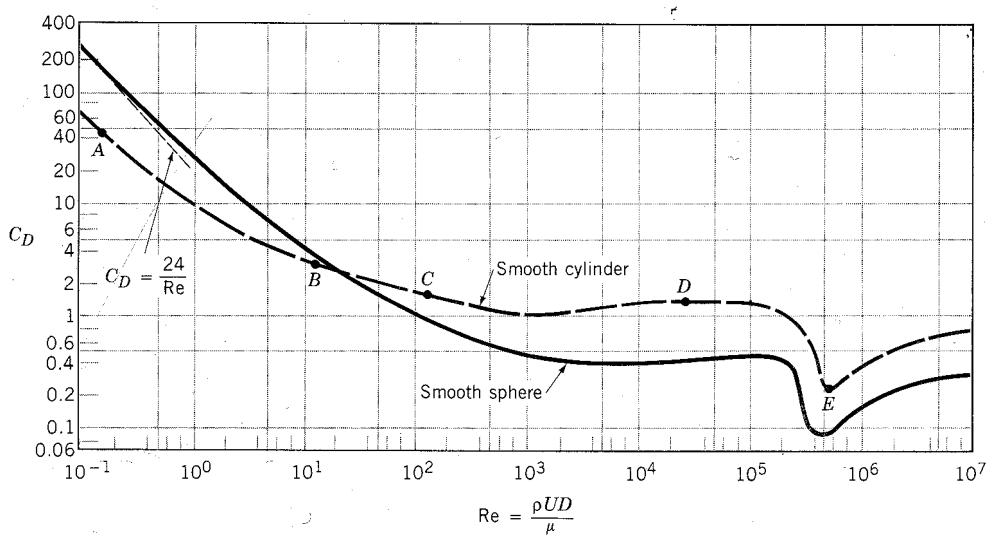

Figure 4.3: Drag coefficient as a function of Reynolds number for a smooth cylinder and for a smooth sphere. Adapted from [16].

4.5 Radiation Exchange

4.5.1 The Extinction Coefficient

In a fibrous absorber setting, a beam penetrates to some depth. The absorbed fraction is largely dependent on the extinction coefficient κ, which is in essence, the reciprocal of the mean penetration depth ξ. This relationship can be expressed mathematically as

$$\kappa = n_f d_f L_\perp = 1/\xi \tag{4.17}$$

where d_f is the fibre diameter and $L_\perp$, the projected length of the fibres normal to the direction of the radiation. The number density n_f (i.e the number of fibres per unit volume), of the fibres in a typical volume element can be calculated as:

$$n_f = \rho_w / m_f = \frac{4}{\pi d_f^2 L_f} \frac{\rho_w}{\rho_f} \tag{4.18}$$

where ρ_w is the apparent density of the fibrous mass, ρ_f is the inherent density of the fibre material, and m_f is the mass of an average fibre of length L_f.

To find the effective absorption length $\bar{L}_\perp$, let us consider a fibre of length L_f, arbitrarily oriented to the direction of the impinging beam as shown in figure 4.4. The length of the fibre as 'seen' by the incoming rays is equivalent to $L_f \cos\theta$. We then

integrate $L_f \cos\theta$ over a solid angle $d\omega = \sin\theta d\theta d\phi$ with limits [-$\pi/2, \pi/2$] and $[0, 2\pi]$ for θ and ϕ respectively, and then divide[2] by 4π.

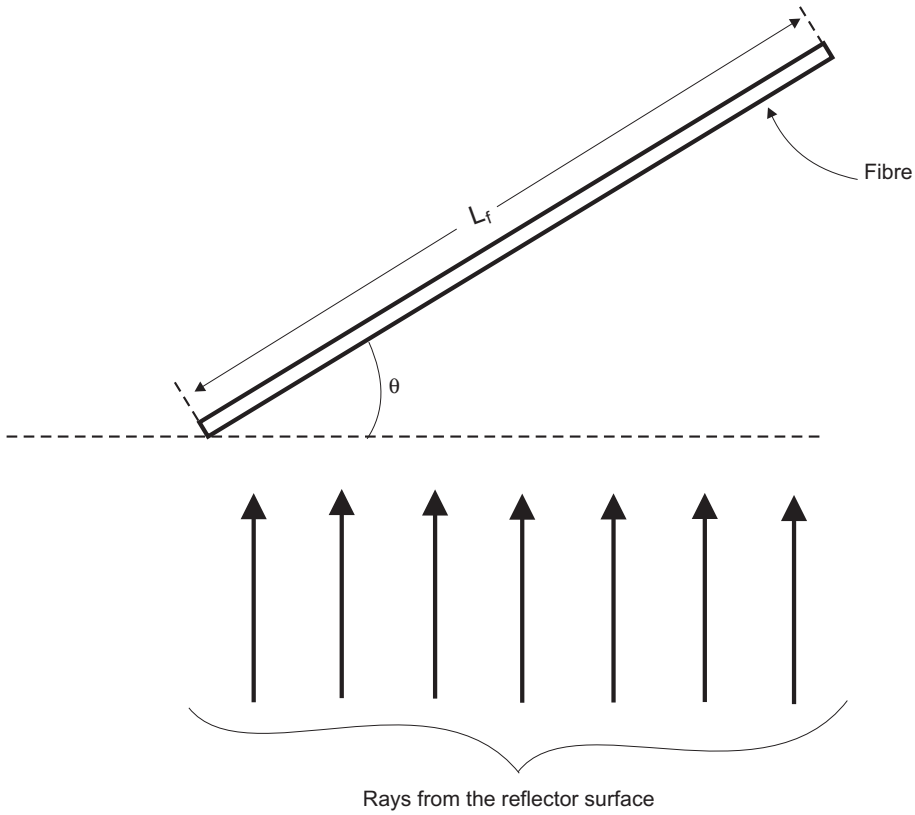

Figure 4.4: The effective absorption length of fibre is $L_f \cos\theta$, the rays are assumed to be parallel.

Because of the nature of the problem, it is easier to use the limits; $0 \leq \theta \leq \pi/2$, and then multiply the integral by a factor of two. Hence, using the later option and making the necessary simplifications yields to

$$\bar{L}_\perp = \frac{L_f}{2\pi} \int_0^{\pi/2} \cos\theta \sin\theta d\theta \int_0^{2\pi} d\phi \tag{4.19}$$

Solving the integral for ϕ and then putting $\sin\theta d\theta = -d(\cos\theta)$ gives

$$\bar{L}_\perp = -L_f \int_0^{\pi/2} \cos\theta d(\cos\theta) \tag{4.20}$$

To simplify the integration, we make a substitution: $x = \cos\theta$ and also adjust the limits accordingly, solving the resulting integral yields to

[2]Division by 4π means the resulting effective length is per unit solid angle.

$$\bar{L}_{\perp} = -L_f \int_1^0 x d(x) = L_f/2 \tag{4.21}$$

For randomly oriented fibres, the effective optical absorption length is to the order of half the length of the fibres. Substituting equations (4.18) and (4.21) into (4.17) it follows that the extinction coefficient can be approximated by

$$\kappa = \frac{2}{\pi d_f} \frac{\rho_w}{\rho_f} \tag{4.22}$$

If ρ_w varies with position, then the extinction coefficient κ, must obviously be expressed as an integral. In our case, we assume ρ_w to be constant unless specified.

The proposed absorber can be considered to be a high porosity fibrous medium since the separation between individual fibers is much greater than the fibre diameter and the wavelength of the incident radiation. In simple terms, each fibre acts as an isolated absorber and or scatterer. The physics of the problem is different for high-density fibrous media, where the fiber spacing is comparable to the fiber diameter and wavelength, see works by Lee et al. for an elaborate treatment [19, 20].

4.5.2 Exchange Area Relations

The need for a quantitative assessment of radiation heat transfer in a multidimensional inhomogeneous media is under pursuit in this section. Over the years, different techniques with varying degrees of complexity have been developed to solve the same problem. Not to mention all but a few, examples include: the discrete ordinate method [21, 22, 23], the finite-element method [24], and the zonal method [25] among other such techniques. However, the majority of these techniques have only shown some degree of success in demonstrating certain effects of radiation heat transfer, usually in simplified idealized conditions.

Nevertheless for our case, a properly tailored finite element method, accounting for multidimensional aspects of radiative heat transfer in inhomogeneous and non-isothermal media [26, 27] would be an effective approach. The domain of interest, usually a non-isothermal media, is subdivided into surfaces or volumes zones that are each approximated to be isothermal. An energy balance is then performed for each zone. This process leads to a set of simultaneous equations for the unknown temperatures or heat fluxes.

The basis of such an approach would lead to direct-exchange area (DEA) relations, a concept commonly used with zonal method. In our case, the DEAs would represent the geometrical and optical relationship of every zone with each other [28, 29]. An

in-depth description of such a method is treated by Modest [30]. A survey on the literature treating this method attributes the method's origins to Hotel and Cohen [31].

The gist of the DEA is now developed, in our case, for a non-isothermal fibrous material of uniform density, which is assumed to be a gray absorbing/emitting medium. To serve as an example of what is understood to be DEA in this work, only one case (the volume-to-surface exchange area) will be discussed in detail. The other two will be quoted as definitions from commendable literature [30, 27] on the subject. Consider a finite volume V, (and also a finite surface A) subdivided into smaller finite isothermal cells ΔV or elemental surface areas ΔA such that

$$V = \sum_{i=1}^{N_1} \Delta V_i \ , \qquad A = \sum_{j=1}^{N} \Delta A_j$$

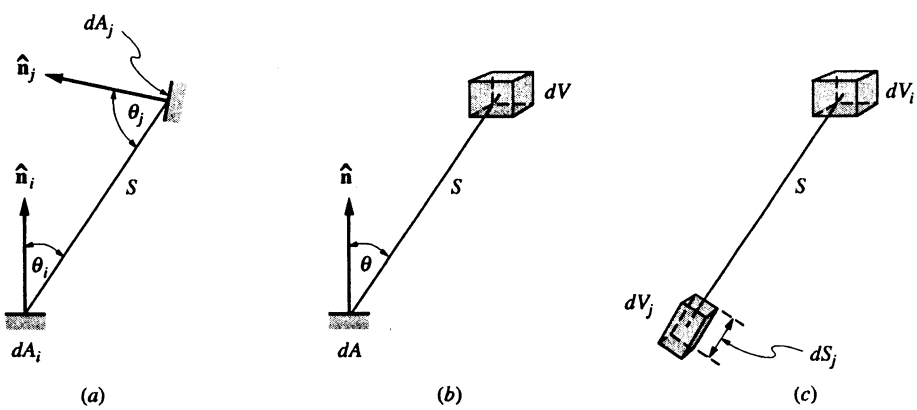

Figure 4.5: Schematic to illustrate radiation exchange between (a) two differential surface-elements (b) differential volume- and surface-element (c) two differential volume-elements. Adapted from[30].

Now, let's consider a differential volume dV_i in radiative exchange with a differential surface dA_j , see the illustration in figure 4.5 (b). S is the vector-distance between the respective points of reference of the said differential elements. The emissive power per unit solid angle[3] around dV is $\kappa_i I_b dV_i$. The surface element dA_j subtends a solid angle $dA_j \cos\theta / S^2$ when viewed from dV_i. If the extinction coefficient κ is assumed to be constant over the optical path S, then the fraction of radiation transmitted through the path S is equal to $e^{-\kappa S}$ [32]. Multiplying these factors and then integrating over ΔV_i and ΔA_j gives the energy arriving at the surface element ΔA_j, from the finite volume element ΔV_i as:

[3]The emissive power in all directions from dV_i is $4\pi I_b dV_i$, and dividing it by 4π will give the emissive power per unit solid angle.

$$q''_{i-j}\Delta A_j = \kappa \int_{\Delta V_i}\int_{\Delta A_j} I_b\ e^{-\kappa S}\ \frac{\cos\theta_j}{S^2}\ dA_j dV_i \tag{4.23}$$

Assuming that the volumes and surfaces of interest are sufficiently finely divided, I_b does not need to be integrated over dV_i [33, 34]. Substituting $I_b = \sigma T^4/\pi$ and $q_{i-j} = q''_{i-j}\Delta A_j$ in the above equation, we get:

$$q_{i-j} = \kappa_i \frac{\sigma T_i^4}{\pi}\ \int_{\Delta V_i}\int_{\Delta A_j} e^{-\kappa S}\ \frac{\cos\theta_j}{S^2} dA_j dV_i \tag{4.24}$$

from which the so called *volume-to-surface direct exchange area*, commonly denoted by $\overline{g_i s_j}$, is defined as

$$\overline{g_i s_j} = \int_{\Delta V_i}\int_{\Delta A_j} \kappa_i\ e^{-\kappa S}\ \frac{\cos\theta_j}{\pi S^2} dA_j dV_i \tag{4.25}$$

Hence, the energy arriving at ΔA_j is regarded as the emissive power σT_i^4 of the fibrous material in ΔV_i that is radiated from an effective surface area $\overline{g_i s_j}$. Since the volume V has supposedly been divided into N isothermal zones, the total energy flux incident upon ΔA_j is

$$q''_{i-j} = \frac{1}{\Delta A_j}\ \sum_{i=1}^{N}\ \overline{g_i s_j}\ \sigma T_i^4 \tag{4.26}$$

Basically, an analysis similar to the one used to arrive at the definition of $\overline{g_i s_j}$, can be applied to derive the *surface-to-surface* ($\overline{s_i s_j}$) and *volume-to-volume*($\overline{g_i g_j}$) DEAs. Illustrations are shown in figure 4.5 (a) and (c). By definition, these two DEAs can be expressed as the following integrals:

$$\overline{s_i s_j} = \int_{\Delta A_i}\int_{\Delta A_j} e^{-\kappa S}\ \frac{\cos\theta_i \cos\theta_j}{\pi S^2}\ dA_j dA_i \tag{4.27}$$

$$\overline{g_i g_j} = \int_{\Delta V_i}\int_{\Delta V_j} e^{-\kappa S}\ \frac{\kappa_i \kappa_j}{\pi S^2}\ dV_j dV_i \tag{4.28}$$

The reciprocity relation also holds for DEAs, i.e making the same arguments in the opposite direction, it can be shown that

$$\overline{s_i s_j} = \overline{s_j s_i}, \quad \overline{g_i g_j} = \overline{g_j g_i}, \quad \overline{g_i s_j} = \overline{g_j s_i} \tag{4.29}$$

The relations in equation (4.29) simplify computations involving DEAs a great deal. Unlike the configuration factors, the DEAs are not non-dimensional but have the dimensions of area.

4.5.3 Thermal Radiation Exchange Inside the Absorber

A combination of the DEA and the reciprocity relations will now be employed to discuss radiative heat exchanges pertinent to our system: a U-shaped receiver (fibrous material) with a concentric opening in the centre. To suppress convective and infrared losses, a spherical glass cover, also concentric with the receiver, is included. In this model, the said absorber is discretized into volume elements, each believed to be in radiative communication with one another and all the surface-elements of interest.

In general, all the three types of DEAs are present in our case. The nature of the problem at hand requires the cylindrical and the spherical parts of the absorber to have different densities. Hence, their respective extinction coefficients will differ as well. To tackle this problem, the optical path S will be treated as $S = S_1 + S_2 + ...$, where each segment has a constant extinction coefficient, κ_1, κ_2, etc respectively. This implies that the transmission factor in the DEAs for our case, will be modified to $e^{-(\kappa_1 S_1 + \kappa_2 S_2 + ...)}$ depending on the nature of the optical path in question. As an example, the generalized form of, say $\overline{g_i g_j}$, will be as follows

$$\overline{g_i g_j} = \int_{\Delta V_i} \int_{\Delta V_j} e^{-(\kappa_1 S_1 + \kappa_2 S_2 + ...)} \frac{\kappa_i \kappa_j}{\pi (S_1 + S_2 + ...)^2} \, dV_j dV_i \tag{4.30}$$

In the same manner, the transmission factor in $\overline{g_j s_i}$ and $\overline{s_i s_j}$ will be adjusted in conformity with changes in optical path. The energy arriving at ΔV_j emitted from another volume element ΔV_i (and vice versa) is given by

$$q_{i-j} = \overline{g_i g_j} \sigma T_i^4, \qquad q_{j-i} = \overline{g_j g_i} \sigma T_j^4 \tag{4.31}$$

Therefore, the net radiation exchange at ΔV_i can be expressed as

$$\Delta q_i = q_{i-j} - q_{j-i} = \overline{g_i g_j} \sigma (T_i^4 - T_j^4) \tag{4.32}$$

If the domain of interest has N volume elements and K surface elements, the corresponding net radiation at ΔV_i is therefore computed as

$$\Delta q_{i,net} = \sigma \sum_{j=1}^{N} \overline{g_j g_i} (T_j^4 - T_i^4) + \sigma \sum_{n=1}^{K} \overline{s_n g_i} (T_n^4 - T_i^4) \qquad for \quad i = 1, 2, 3, ...M \tag{4.33}$$

Expressed in this way, $q_{i,net}$ is positive if zone i is gaining energy as a result these radiative exchanges, and negative if the opposite is true. In our case, $i = 1, 2, 3, ...M$ represents the particular elements belonging to a set of reference cells i.e isothermal zones of a representative slice of the absorber system. In the case of a surface element ΔA_k, the net radiative exchange as a result of interacting with elements from the same domain as above is

$$\Delta q_{k,net} = \sigma \sum_{j=1}^{N} \overline{g_j s_k}(T_j^4 - T_k^4) + \sigma \sum_{n=1}^{K} \overline{s_n s_k}(T_n^4 - T_k^4) \qquad for \quad k = 1, 2, 3, ...M' \quad (4.34)$$

in which case $k = 1, 2, 3, ...M'$ is here taken to represent particular members of the reference surface-elements set. The importance of equation (4.34) is that it is the basis for assessing heat loss to the ambient. In essence, the heat loss from the absorber as it is understood in this model, is primarily radiative loss from the glass to the atmosphere since convection loss is not expected to be that significant after suppression by the glass cover.

4.5.4 The Glass Cover

In our case, the purpose of a transparent cover or glazing is largely to shield the absorber from the wind and therefore effectively suppress convection losses. However, the glazing material should be one that allows solar energy to pass freely, simultaneously restraining heat transfer that would, in the absence of the glazing, pass freely from the absorber to the ambient. Modern technology has produced coatings on glass that can reflect the long-wave radiation but is transparent to short-wave radiation, i.e the glazing becomes a transparent insulator. These coatings reflect radiant infrared energy, thus tending to keep radiant heat on the same side of the glass from which it originated.

For an elaborate treatment on glazing and coatings, reference is given to Granqvist et al [35]. Duffie and Beckman [36] recommend low-iron glass for use in solar energy applications because if the Fe_2O_3 content is high, it will significantly absorb in the infrared portion of the solar spectrum. The general picture is that the glass dome does not eliminate the heat flow that would ordinarily pass to the environment; it rather suppresses it somewhat.

4.6 Discussion of Modelling Results

Based on the theoretical premise thus far treated, a computer model that imitates the said radiative and convective heat exchanges was developed (*courtesy of J. Løvseth*) in MATLAB. It was then used to study what happens inside the proposed volumetric fibrous absorber.

The results analyzed in this section are for a volumetric fibrous absorber with R_{out}=7.0 cm, R_{in} = 2.5 cm, and a cylindrical height of 1.3 cm: irradiated by parabolic dish of aperture radius equal to 1.0 m. The resultant concentration ratio is; $C \simeq 100$.

The said absorber-inner and -outer radii yield to a thickness of 4.5 cm, (i.e R_{out}-R_{in} = 4.5 cm). The anticipated construction is such that the inner diameter as defined by R_{in}, must coincide with that of the air transport pipes.

The thickness of the absorbing material can be varied by increasing or decreasing either the outer or inner radii while the other one is maintained constant. Increasing R_{out} generally implies a reduction in concentration ratio while reducing this thickness by increasing inner radii leads to a significant portion of the incident radiation passing through unabsorbed. Alternatively, reducing the thickness could be compensated by reducing mean penetration depth. However, the simulation programme has shown that doing this confines absorption closer to the surface and resultantly increases loss to the ambient.

4.6.1 Determination of Mean Penetration Depth

As shown in section 3.3.4, the height of the cylindrical part is much smaller compared to dimensions of the spherical section. It is therefore imperative that the mean penetration depth (ξ_2) in the cylindrical section, must be shorter than its counterpart (ξ_1) in the spherical section, i.e in order to maximize absorption, the apparent density of the absorbing material must be such that $\xi_1 \geq \xi_2$.

In the simulation programme, which takes into account absorption of solar radiation, thermal radiation exchange between cells and heat transfer to air by convection, all possible combinations for which $\xi_1 \geq \xi_2$, $\xi_1 = \xi_2$ and $\xi_1 \leq \xi_2$ within the range of interest had to be tried. The results confirm that minimum heat loss is achieved when $\xi_1 \geq \xi_2$. The plot presented in figure 4.6 shows that in the case of the dimensions under consideration, minimum heat loss to the ambient is achievable when $\xi_1 \simeq 2.0$ cm and $\xi_2 = 1.0$ cm. Net radiative heat transfer from receiver to glass cover is also minimal at the same points.

The (somewhat) broad minimum suggests that the unavoidable practical problems that might occur in achieving a homogeneous fibrous material density will not change the general picture very much, as long as it is within an acceptable range. For example, in this case, we do not expect optical depths averaging within 2.1±0.3 cm to cause substantial increases to the heat loss.

The glass cover temperature, which principally determines radiative heat loss from the absorber system is shown in figure 4.7. A cross-check with the plot for net thermal from the receiver to glass cover in figure 4.6, shows that minimum glass temperature corresponds to minimum net thermal power as expected. The resultant heat loss to the ambient also confirms this point.

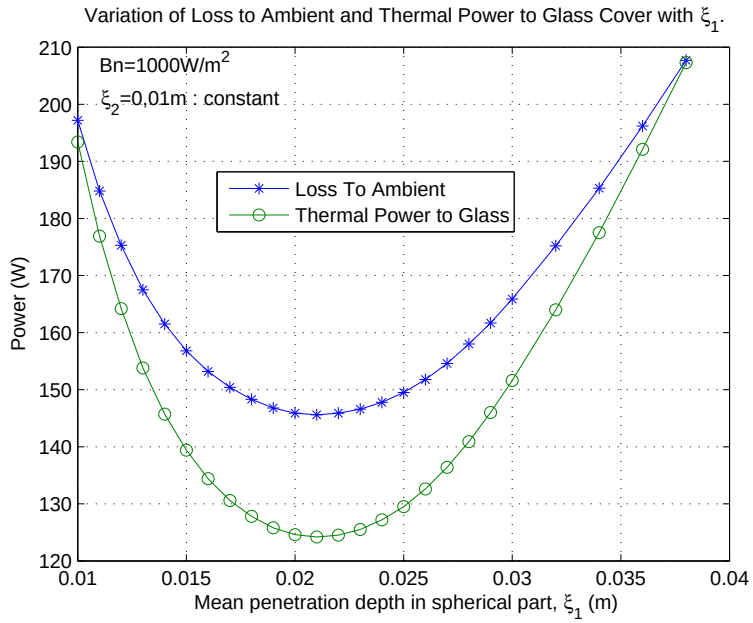

Figure 4.6: Plots showing variation of heat loss to the ambient and net thermal power to glass cover, with changing penetration depth in the spherical part. The penetration depth in the cylindrical section is kept constant. Bn is the radiation intensity.

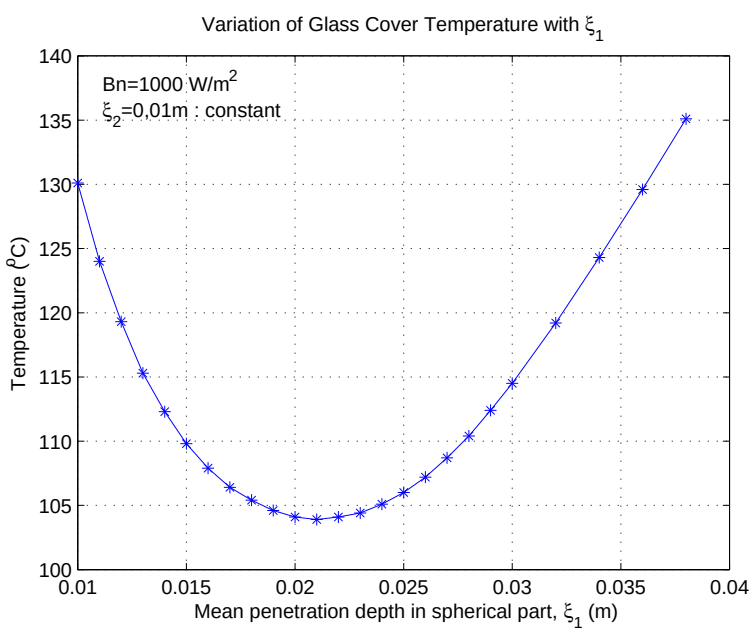

Figure 4.7: Plot showing variation of glass cover temperature with changing penetration depth in the spherical part. The penetration depth in the cylindrical section is kept constant.

4.6.2 Mass Flow Rate

The mass flow rate is of concern as it determines the energy extracted from the fibrous absorber, and then transported to the thermal storage. The results obtained are shown in figure 4.8.

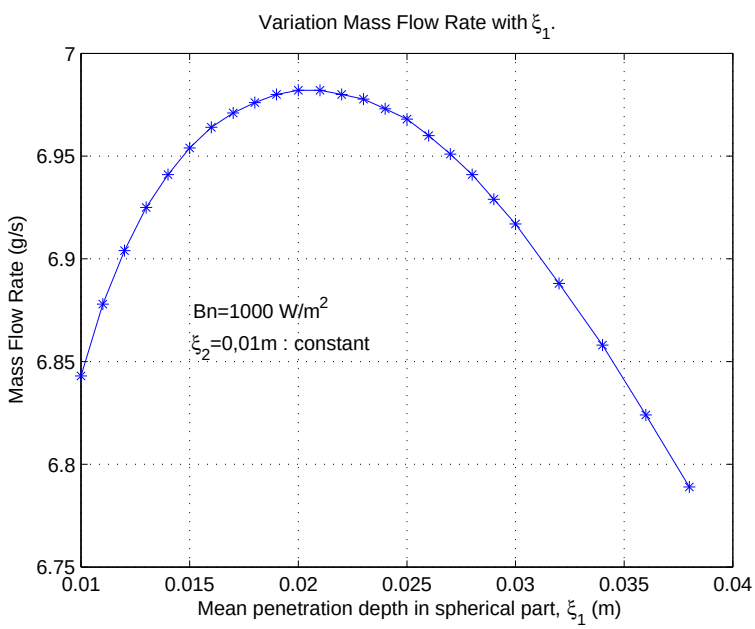

Figure 4.8: Plot showing variation of mass (air) flow rate with changing penetration depth in the spherical part. The penetration depth in the cylindrical section is kept constant.

The computation of mass flow rate is dependent mainly on the energy absorbed by the fibres, which is then picked up by the convective fluid (air in our case). Therefore, a deeper penetration favours more absorption until a certain optimal fibrous material density ρ_w, which when exceeded, starts allowing a growing number of photons to go through the absorber without being absorbed. The nature of the plot in figure 4.8 is in agreement with plots presented in the previous section, see figure 4.6. For the set of parameters and conditions under discussion, a mass flow rate to the order of 7 g/s would be optimal to raise the temperature of the air to about 400 ^{o}C within the receiver.

4.6.3 Efficiency of the Receiver

Variation of the anticipated efficiency of the absorber is of primary importance for practical purposes. In this case, it is defined as ratio of the energy finally picked up by the convective air to the radiant energy incident on the receiver after reflection

by the parabolic dish.

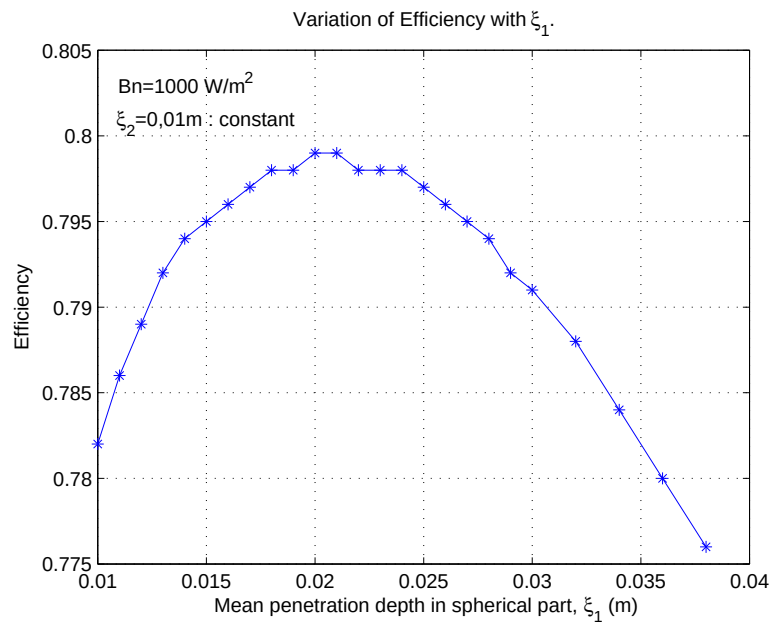

Figure 4.9: Plot showing variation of mass (air) flow rate with changing penetration depth in the spherical part. The penetration depth in the cylindrical section is kept constant.

It is interesting to note that the efficiency plot of the absorber system in question has a maximum that corresponds and agrees with the other results. The plot is presented in figure 4.9. It also suggests that small discrepancies in fibrous material density can be accommodated without problems. On average, an efficiency quite close 80% is predicted for the conditions and settings being discussed here.

4.7 Distribution Profiles Within a Representative Slice of the Receiver

This section presents simulation results of the spatial variations (distribution profiles) of values of state variables characterizing the absorber system during operation in steady state as predicted by the modelling programme. The results being discussed are only for a set of reference volume-elements within a representative slice of the absorber system. This slice is essentially a single azimuthal division ($\Delta\phi$), discretized such that divisions in θ are within the range of $0 \leq \theta \leq 90$ for the spherical section while $\theta > 90$ refers to the cylindrical section, see figure 4.1. Division in radius in both sections are understood to be equal and coincident. The entire configuration can then be accounted for using symmetry applicable to the receiver configuration.

4.7.1 Spatial Variation of the Drag Force and Air Velocity

As the air traverses the absorber material towards the central suction zone, it experiences a drag that strongly depends on air velocity, and rather mildly on the drag coefficient. For conditions and settings under discussion, the drag coefficient has been found to be within $2 \leq C_D \leq 7$. Simulation shows that air accelerates much faster in the spherical section compared to whats happens in the cylindrical section, see figure 4.10. This is partly due to the geometrical differences (between a cylinder and a sphere, as depicted by equations 4.9 and 4.10) and partly due to the fibrous material density which is double in the cylindrical part as explained in section 4.6.1. The implied effects include reduced convection heat transfer in the cylindrical part, leading to higher temperatures as will be seen later.

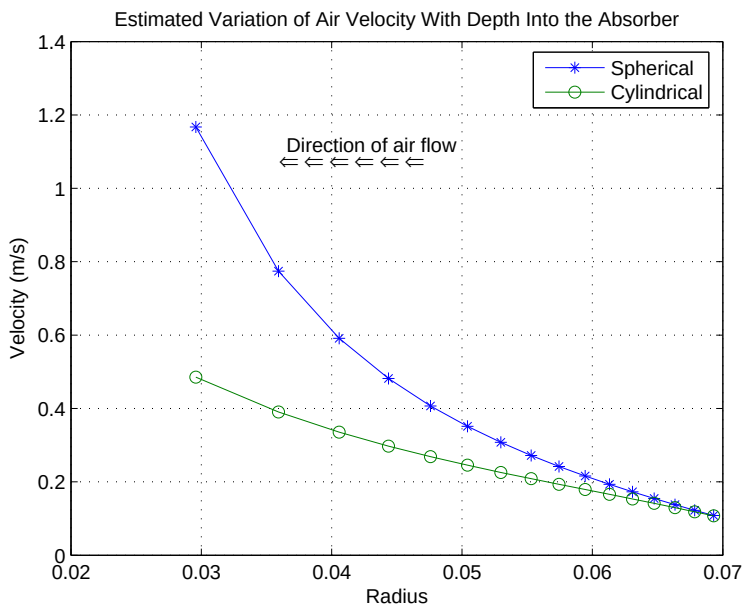

Figure 4.10: Estimated spatial variation of air velocity radially and with depth into the receiver material of apparent density of fibrous material 5 kg/m^3, diameter of fibres 0.1 mm, while density of the fibre material is taken to be 7800 kg/m^3 (i.e stainless steel fibres).

In principle, the magnitude of the drag force determines the blow power that is needed to overcome it. In the case of the size of the receiver system under discussion, the total drag force is less than 1 N. In general, these results help to enlighten that the implied fan power needed to overcome drag in the receiver will not cause serious problems i.e the pressure drop within the receiver doesn't seem to be significant.

4.7.2 The Radial and Sector-wise Temperature Profiles

It is of interest to analyze how the fibre and air temperatures vary radially and with depth into the absorber. Such temperature profiles, as predicted by our simulation programme, are shown in figures 4.11 and 4.12 respectively. The pattern of the air and fibre temperature profiles is similar. However, a closer analysis shows that as the air flows towards the central hollow part, the temperature of the air lags behind that of the fibres in the same cells. As it advances deeper into the absorber, the air convectively picks up heat from the fibres, thereby closing the gap between the fibre and air temperatures.

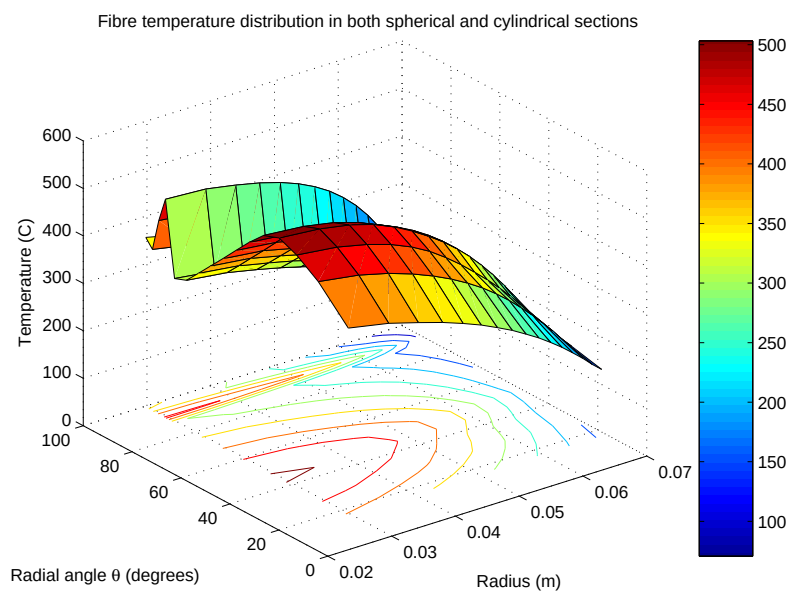

Figure 4.11: Variation of fibre temperature radially(θ-wise) and with depth into the absorber. The corresponding isothermal contours are also shown in the θ-radius plane.

The effect of lower air velocities and double density of the absorbing material in the cylindrical section ($\theta > 90^o$) is evident. Lower velocities imply reduced heat transfer by convection. As a result, it is generally expected that the cylindrical section will manifest higher temperatures compared to its immediate neighboring cells pertaining to the spherical section.

The reflected radiation is not evenly distributed as it strikes the absorber. The outcome from parabolic geometry of the reflecting dish gives a power distribution at the receiver surface as that represented by figure 4.13. The amount of radiation reflected to the receiver is a function of the cosine of the angle between the impinging rays

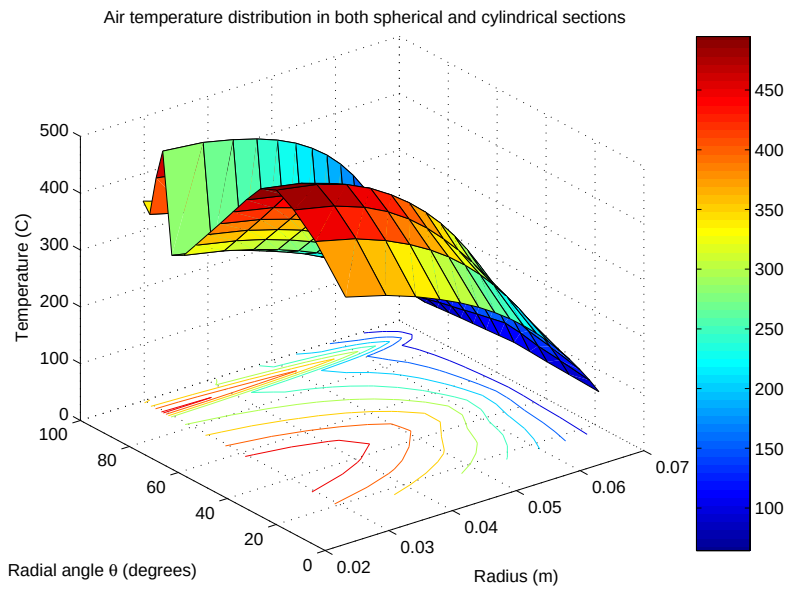

Figure 4.12: Variation of air temperature radially(θ-wise) and with depth into the absorber. The corresponding isothermal contours are also shown in the θ-radius plane.

and the surface normal to the mirror tiles in a particular ring. As a result, cells that are approximately in the range of $(40 \leq \theta \leq 60)$ receive higher doses of the reflected radiation than the rest at the same radius or depth.

With a solar radiation intensity to the order of 1000 W/m^2, the anticipated outlet air-temperature for sectors within a radial angle of $\theta \leq 85°$ is well over 300° C. That accounts for more than 80% of the sectors. Under the same conditions, the temperature of the coldest streams($85° < \theta \leq 90°$) of air entering the central suction-zone is predicted to be about 250° C, while hottest sectors, in the range $30° \leq \theta \leq 60°$ are anticipated to be about 450° C or slightly more. The predicted average temperature of these air streams is to the order of 397 ° C.

It is believed that, apart from the low heat capacity of air, the effective passage of heat from the fibres to the air is partly indebted to the *Ratio** of the convection surface $(\pi d_f L)$ to the absorption surface $(d_f \frac{L}{2})$, which is to the order of 2π. In other words, the convection surface is more than sixfold the size of its absorption counterpart, an arguably worthy point for consideration in this case.

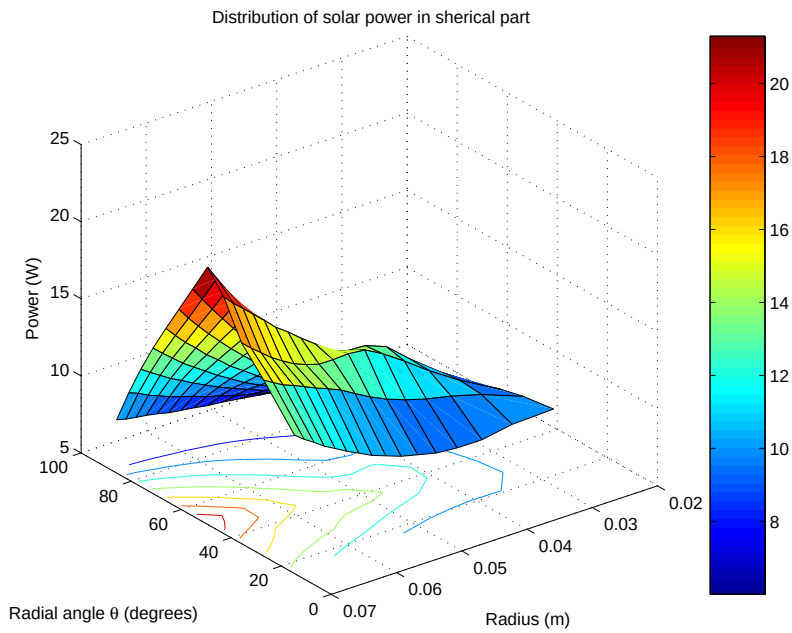

Figure 4.13: Solar power distribution in the spherical part.

4.7.3 Distribution of Thermal Power

The results of the radiation exchange between cells as discussed in the previous sections are shown in figure 4.14 for the representative slice. This figure illustrates the cells that are expected to be losing (orange to deep red) or gaining power as result of radiation exchange (yellow to white cells). Because their temperature is much higher than that of their neighbors in the spherical section, the net radiation lost by cells deep in the cylindrical section is evidently much higher. However, it is important to note that the majority of cells losing net power as a result of radiation exchange are located deeper in the spherical section, the dominant part.

The average thermal loss from individual zones is to the order of 3 W while those gaining get a paltry 1 W at most. This suggests that, the thermal power balance (i.e the difference between sum of the positive and negative values of thermal power) in steady state, is mainly lost to the glass dome, which will in turn pass a substantial amount of this power to the ambient as loss.

4.8 Chapter Summary and Conclusions

A mathematical model, based on the finite-element method, has been developed to study the behaviour of the volumetric absorber. The essence of the method involves

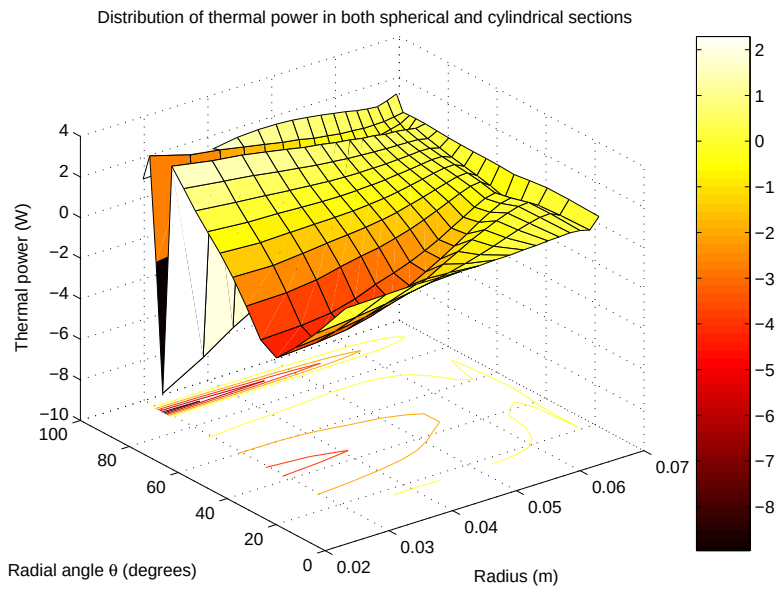

Figure 4.14: Distribution of thermal power in the spherical part. Isothermal zones that are losing have negative power and those ones that are gaining have positive values.

discretizing the absorber into isothermal volume elements (referred to as cells), which are characterized by the so called direct exchange areas (DEAs) that enable the establishment of thermal radiation exchange.

MATLAB routines have been used to develop a computer model, which takes into account thermal radiation exchange between the cells, absorption of solar radiation and convective heat transfer from the fibres to air. This simulation programme has been used to study in detail various aspects, parameters and variables of prime importance that include: absorber efficiency, mass flow rate, the radial and sector-wise temperature profiles for both air and the fibres.

In this case, it is reasonable to regard the efficiency of the absorber as the overall performance indicator. For the settings and conditions that have been discussed in this chapter, a marginal variation contained within 75 - 80% was found when the mean penetration depth was correspondingly varied from 1.0 - 3.0 cm in the spherical section (the dominant and main part of the absorber). When the solar radiation levels are low, say 300 W/m^2, the absorber efficiency dropped down to well below 70%, which suggests that thermal radiation is more dominant than solar radiation; the vice versa is true for high radiation levels.

The main objectives for developing the simulation programme include the need to

understand how such a receiver works, which would in turn facilitate the exploration of the possibilities of optimizing its construction and or operation. As far as these targets are concerned, it can be said that the simulation programme has yielded valuable insights and shaded more light regarding the major issues of concern for practical considerations in both its construction and during operation. However, these predictions still stand to be validated in the next phase: the construction and testing of a solar oven prototype.

References

[1] Bear J, 'Modeling Transport Phenomena in Porous Media'. *Convective Heat and Mass Transfer in Porous Media*, NATO ASI series E, Applied Sciences, vol.196, 1991.

[2] Kowalski G.J and Mitchell J.W, 'Analytical and experimental investigation of heat transfer mechanisms within fibrous media exposed to solar radiation', 20*th Joint ASME/AIChE National Heat Transfer Conference*, 1982.

[3] Vafai K(editor), 'Handbook of porous media', 2*nd edition*, 2005.

[4] Kurosaki Y, and Yamada J, 'Radiation transport in porous media'. *Convective Heat and Mass Transfer in Porous Media*, NATO ASI series E, Applied Sciences-vol 196, 1991.

[5] Kaviany M, 'Principles of Heat Transfer in Porous Media', 2*nd edition*, *Mechanical Engineering Series*, 1999

[6] Pop I and Ingham D.B, 'Convective heat transfer - mathematical and computational modeling of viscous fluids and porous media', 2001.

[7] Travkin V.S, and Catton I, 'Porous media descriptions - non-local, linear and non-linear against effective thermal/fluid properties'. *Advances in colloid and interface science*, $76 - 77$, pg $389 - 443$, 1998.

[8] Pitz-paal R, Hoffschmidt B, Bömer M, and Becker M, 'Experimental and numerical evaluation of the performance and flow stability of different types of open volumetric absorbers under non-homogeneous irradiation', *Solar Energy*, vol.60, Nos.3/4, pp $135 - 150$, 1997.

[9] Kribus A, Doron P, Rubin R, Reuven R, Taragan E, Duchan S and Karni J, 'Performance of DIAPR operating at 20 Bar and $1200°C$', *ASME J. Sol Energy Eng.*, vol.123, pp $10 - 17$, 2001.

[10] Hellmuth T.E and Matthews K.L, 'Modeling and optimum design of a wire mesh solar volumetric air receiver', *Solar Engineering*, vol.1, 1995.

[11] Kribus A, Ries H and Spirkl W, 'Inherent limitations of volumetric solar receivers', *Journal for Solar Energy Engineering*, vol.118, pp 151 − 155, 1996.

[12] Lee Siu-Chun, 'Effect of fibre orientation on thermal radiation in fibrous materials'. *Int. J. Heat and Mass Transfer*, vol-32, No.2, pp 311 − 319, 1989.

[13] William H. McAdams, 'Heat Transmission' *3rd edition*, pg252 − 280, 1954.

[14] Holman J.P, 'Heat Transfer', *4th edition*, pg 212 − 220, 1963.

[15] Løvseth J, 'Small Scale, Multi-purpose Concentrating Solar Energy Systems', 2001, (Unpublished).

[16] Munson B.R, Young D.F and Okiishi T.H, 'Fundamentals of Fluid Meachanics', 4th edition, 1999.

[17] Cheremisinoff N.P, 'Encyclopedia of Fluid Mechanics: Flow Phenomena and Measurement', Vol.1, 1986.

[18] White F.M, 'Fluid Meachanics'. 2nd edition, 1994.

[19] Lee S and Grzesik J. A, 'Scattering Characteristics of Fibrous Media Containing Closely Spaced Parallel Fibres', *Journal of Thermophysics and Heat Transfer*, Vol.9, No.3, 1995.

[20] Lee Siu-Chun, 'Dependent vs independent scattering in fibrous composites containing parallel fibres'. *Journal of Thermophysics and Heat Transfer*, vol.8, No.4, 1994.

[21] Fiveland W.A, 'Discrete ordinate method for radiative transfer in isotropically and anisotropically scattering media', *J.Heat Transfer*, vol.109, no.3, pp 809 − 812, 1987.

[22] Selcuk N and Ayranci I, 'The method of lines solution of the discrete ordinate method for radiative transfer in enclosures containing scattering media', *Numer. Heat Transfer B*, vol.43, no.2, pp 179 − 201, 2003.

[23] Krisnamoorthy G,Rawat R, and Smith P.J, 'Parallel computations of radiative heat transfer using the discrete ordinate method', *Numer. Heat Transfer B*, vol.47, n0.1, pp 19 − 38, 2005.

[24] Razzaque M.M, Klein D.E, Howell J.R, ' Finite element solution of radiative heat transfer in a 2-D rectangular enclosure with gray participating media', J. Heat Transfer, vol.105, no.4, pp 933 − 934, 1983.

[25] Hottel H.C and Sarofim A.F, 'Radiative Transfer', *McGraW-Hill*, New York, 1967.

[26] Nobel J.J, 'The zonal method: Explicit matrix relations for total exchange areas', Int J. Heat Transfer, vol.18, no.2, pp 261 − 269, 1975.

[27] Yuen W.W and Takara E.E, ' The zonal method: A practical solution method for radiative transfer in non-isothermal inhomogeneous media', *Annu. Rev. Heat Transfer*, vol.8, pp153 − 215, 1997.

[28] Tian W and Chiu W.K.S, 'Calculation of direct exchange areas for non-uniform zones using a reduced integration scheme', Journal of heat transfer, ASME, vol.125, pp 839 − 844, 2003.

[29] Yuen W.W, 'The multiple absorption coefficient zonal method(MACZM), an efficient computational approach for the analysis of radiative heat transfer in multidimensional non-gray media', *Numer. Heat Transfer B*, vol.49, pp 89 − 103, 2006.

[30] Modest M.F, 'Radiative heat transfer', 2*nd* edition, pg 133, 1993.

[31] Hottel H.C and Cohen E.S, 'Radiation exchange in a gas filled enclosure: Allowance for non-uniformity of gas temperature', *AIChE Journal*, vol.4. pp 3 − 14, 1958.

[32] Travkin V.S, and Catton I, 'Radiation heat transport in porous media'. *ASME* vol.3, 1999.

[33] Siegel R, Howell J R, 'Thermal Radiation Heat Transfer', 4*th Edition*, pg 423.

[34] Viskanta R and Mengüc M.P, 'Radiation Heat Transfer in Combustion Systems',*Progress in Energy and Combustion science,* vol.13, pp 97 − 160, 1987.

[35] Granqvist C.G, Terry K.G and Wright J.L,'Glazings and Coatings', Solar energy, State of the art, ISES position papers, James & James, pp 29 − 108, 2001.

[36] Duffie J.A and Beckman W.A, 'Solar engineering of thermal processing', 2*nd edition*, pg 231, 1991.

Chapter 5

Thermal Energy Storage

5.1 Introduction

Heat storage is an essential feature in solar-thermal applications. The intermittent nature of the availability of insolation, which is largely characterized by a mismatch between its availability and demand, as-matter-of-factly require some form of energy storage. In our case, where solar radiation is harnessed to satisfy energy needs that includes cookery, a detailed study on high-temperature-heat storage is necessary if an optimal and satisfactory system is to be developed.

Quite a number of materials qualify to be used as storage mediums, however, in practice there is no one 'best' heat storage type, but rather each of them has characteristics that might make it the most desirable under certain conditions, depending on the key factors that will be under consideration. Usually the choice is premised on a criteria of consistency in high heat capacity, delivery at a desirable temperature and to do so cost-effectively in terms of running and maintenance costs.

In addition, the economics regarding how much of the annual load is anticipated to be covered by solar, and how much by the auxiliary source plus the degree of reliability expected from the storage system require careful analysis. In the sections that follow, three types of thermal energy storage will be treated. An in-depth discussion is then devoted to the type that has direct relevance to this study: thermal storage in packed beds.

5.2 Types of Thermal Energy Storage

5.2.1 Latent Heat Storage

Phase Change Materials (PCMs) are chemical substances that undergo a phase transition at temperatures within the desired range for heating purposes. In other words, thermal energy can be stored in a material which can naturally experience phase transformation at a temperature that is useful to the application. If a material with phase change temperature T_*, is heated from T_1 to T_2 such that $T_1 < T_* < T_2$, the thermal energy Q taken up by a substance of mass m is given by

$$Q = \int_{T_1}^{T_*} mc_{p,1}\, dT_* + m\zeta + \int_{T_*}^{T_2} mc_{p,2}\, dT_* \tag{5.1}$$

where ζ = heat of phase transformation. In our case, the interesting type of phase change transformations useful for possible application is the solid$\rightleftharpoons$liquid. In general, PCMs which undergo this type of phase transformation are popular for solar energy applications. For this case, equation (5.1) can then be simplified to

$$Q = m[c_{p,s}(T_* - T_1) + \zeta + c_{p,l}(T_2 - T_*)] \tag{5.2}$$

where $C_{p,s}$ and $C_{p,l}$ are the specific heat capacities (at constant pressure) in the solid and liquid phases respectively.

Characteristics that negatively affect design of a latent heat storage system have been summarized by Grodzka[2], some of which are: (i) the cost of many of the more effective latent heat storage materials is high, (ii) some of the latent heat storage materials are not pure materials but mixtures that tend to separate[1] into their component parts on repeated freeze-thaw cycling, (iii) some of the latent heat storage materials such as NaOH can react violently with the organic heat-transfer oils commonly used in solar thermal energy collectors, (iv) super cooling of the latent heat storage material can occur on solidification. Because of these problems and the somewhat abundant availability of sensible heat storage systems, latent heat storage systems have not been widely used in high-temperature solar thermal energy systems[3].

5.2.2 Thermochemical Energy Storage

A thermochemical energy storage system is one where thermal energy is used to break apart chemical bonds in a reversible fashion, in which case, the forward direction is

[1] However, this problem of the mixture separating into individual components can be prevented by using eutectic mixtures where possible.

endothermic (thermal energy storage), while the backward reaction is exothermic (release of heat). For example,

$$A + \Delta H \rightleftharpoons B + C \tag{5.3}$$

The quantity of heat Q stored in such a chemical reaction is a function of the heat of reaction ΔH, and the extent of the reaction:

$$Q = f_r \Delta H \tag{5.4}$$

where f_r = fraction reacted and ΔH, the heat of reaction per unit mass. The separation of chemical bonds requires large quantities of energy input, thus resulting in high energy density storage in small amounts of the material. This is arguably a desirable characteristic that can facilitate easy transportation and long term storage without the need for insulation, thanks to their stability at ambient temperatures. At elevated temperatures the energy storing reaction reverses, forming the original chemical system with the release of heat.

A popular example of such a reversible energy storage system is the thermal splitting of water; a subject under the spotlight in the scientific world as efforts continue to smoothen the technology. At temperatures in excess of $2000°C$, water begins to dissociate into hydrogen and oxygen:

$$2H_2O + \Delta H = 2H_2 + O_2 \tag{5.5}$$

In which case, the reverse reaction;

$$2H_2 + O_2 = 2H_2O + \Delta H \tag{5.6}$$

will not proceed at low temperatures without a catalyst i.e a mixture of hydrogen and oxygen in a container at room temperature will not react.

Research exploring possibilities of the photo-decomposition of water to hydrogen and oxygen has been going on for some time, with significant works surfacing around the late 70s[4, 5]. Several other thermochemical storage systems have been tried since then, not to mention all but just a few, examples include that of $Ca(OH)_2/CaO$ by Fujii et al[6], CO_2/CH_4 by Edwards et al[7] and Imhof's open solar reactor using calcite[8]. Williams and Carden experimented with an ammonia dissociator prototype[9], while Steiner[10] investigated systems for the medium temperature range using MgH_2/Mg. A Recent research by Kolb et al., aimed at using solar power towers for the mass production of hydrogen [11] also contributes towards this technology.

However, although thermochemical energy storage holds much (still largely theoretical) promise, the technology hasn't reached the point of cost-effective practical use in meeting the common man's day to day energy storage needs. Despite the applausable works mentioned above (and many more), there is still a lot of homework to do for scientists and engineers regarding the development of appropriate technology yielding to low-cost thermochemical energy storage.

To date, in the field of solar engineering, only small lab-scale tests have been conducted to demonstrate the feasibility of a few subsystems. Nevertheless, if this technology sees the light of the day, it will surely be a major breakthrough in alleviating the energy crisis threatening the future of this modern world.

5.2.3 Sensible Heat Storage

Conceptually, sensible-heat storage is perhaps the simplest mode of storing thermal energy. In principle, the sensible heat, Q, is stored by raising the temperature of the storage material from T_1 to T_2 and can be expressed as,

$$Q = \int_{T_1}^{T_2} mc_p dT = \int_{T_1}^{T_2} \rho V c_p dT \tag{5.7}$$

where ρ and V are the density and volume of the storage material respectively. The most common sensible heat storage materials include water, oil, rocks, ceramics and molten salts.

Engineering research in the area has been going on over the years, in which case, a variety of fluids has been tested to transport the sun's heat, including water, air and sodium before molten salts took the lead. Nowadays, molten salts, usually a mixture of sodium-nitrate ($NaNO_3$) and potassium-nitrate (KNO_3), have emerged as the favoured choice. As such, it is commonly used as high temperature heat transfer medium in industry and also in solar concentrating applications.

As a heat transfer and or storage medium, molten salts are stable, have a good heat capacity and viscous properties that make them practical mediums for thermal energy transport and or storage. They are simply a low-cost medium which can handle high temperatures compatible with today's high-pressure and high-temperature steam turbines, and it is non-flammable and nontoxic. In addition, when the salt solidifies, it contracts whilst freezing water expands. Thus, molten salt freezing in a pipe would not burst the pipe as water would.

Another somewhat commonly used heat transport and transfer medium for many industrial applications is Dowtherm-A. It is a eutectic mixture of two very sta-

ble compounds biphenyl ($C_{12}H_{10}$) and diphenyl oxide($C_{12}H_{10}O$). The virtue of these compounds is that they have practically the same vapour pressures, implying that the mixture can be handled as if it were a single compound. DOWTHERM-A may be used in systems employing either liquid phase or vapour phase heating. The recommended use temperature ranges are: 15 to 400°C for the liquid phase and 257 to 400°C for the vapour phase.

Water has the highest specific heat capacity of 4190 J/kg·C which has made it an obvious choice for low-temperature heat storage. The advantages of water as a thermal storage medium include: it's abundance at low cost, nontoxicity, inflammability, excellent transport properties, high specific heat capacity and has a well-known counter-corrosion methodology. The main disadvantages are: high vapour pressure, leaks easily and can cause destructive expansion when it freezes.

5.3 Choice of Storage System

The selection of the storage material is an essential part in the designing of thermal energy storage systems. The choice depends on several factors, two of which jointly play a pivotal role in most cases, viz: *solar collection technique* and *application*. The former determines the temperature at which the storage material is expected to be charged, in which case, the thermophysical properties of the storage material at the same temperature are of great importance in gauging the suitability of the material for the task. The maximum rate of charge is also a direct function of the solar collector. The second factor, application, determines the storage discharge temperature and the maximum rate of discharge.

Other factors, the importance of which depends on their relevance to the purpose for which the system is built are: cost-effectiveness, long term cycling[2], complexity of containment system, sophistication of heat exchanger design for maximum rates of charge and discharge, corrosivity and space requirements [12]. Dincer gives an articulate and comprehensive discussion on the evaluation and selection of sensible heat storage technologies, systems and applications in the field of solar energy[13]. A survey of the literature on the subjects shows that criteria, techniques, recommendations, checklists for selection, implementation and operation of energy storage systems are available for use by those interested, for example, see works by [14, 15, 16].

In our case, where the technology is aimed at benefitting rural folks in developing countries, the ultimate deciding factors in the majority of the cases are the initial,

[2]If a particular gas is used and recycled.

running and maintenance costs of the system. This tips the scale in favour of using locally available materials and appropriate technology, which should be as simple as possible. It is therefore, our considered view that, *rock bed storage* is technically best suited for high-temperature thermal energy storage in a rural community in the Third World..

5.4 Air-Rock Storage

The air-rock thermal energy storage is perhaps the most reliable storage system owing to its simplicity. Once the system is installed, maintenance is minimal and few things can decrease the performance of the storage. As a storage material, rocks are cheap and readily available, have fairly good heat transfer characteristics with air (as the transfer medium) at low velocities. Since air-rock thermal energy storage systems are almost maintenance-free and more economic compared to their counterparts, they have been an obvious and logical choice for residential heating.

However, rock storage has a low energy density compared to, say water, PCMs or thermochemical alternatives. In essence, this simply implies a bigger heat storage volume. Additional difficulties include condensation followed by microbial activity if the system is allowed to lie dormant in humid weather for long periods of time.

Essential features include the containment unit with a screen to support the bed, inlet and outlet ducts. In operation, air is allowed to flow through the bed in one direction, usually downwards when the storage is charging (addition of heat). For discharge or heat removal, the direction of air-flow is reversed. Simultaneous addition and removal of heat is usually uncommon with conventional packed beds. However, using appropriate piping system, it should be possible to simultaneously tape some of the incoming hot air directly to the hotplate while the remainder can be used to charge the bed.

In general, an optimum rock pebble size is important for storage purposes. It takes less blow power to force the heat transfer air through large stones than through smaller ones. Nevertheless, bigger pebbles may result in insufficient heat transfer surface area. Probably, equally important is uniformity (roundish and preferably smooth) of size. If there is too much variation, the smaller stones will fill in the voids between the larger stones, thus increasing the air blower power requirement. Consequently, washing or filtering out 'fines' which might otherwise fill in the voids is recommended. Generally, the faster the air flow and/or the smaller the rock size, the greater the power requirement.

5.5 Insulation

Mitigating heat loss to the ambient is a major challenge for high temperature storage systems. Therefore, proper insulation for the air transport pipes and the storage unit is of fundamental importance in our case. Most insulators in common use today rely on the principle of trapping air in fibrous material to reduce convective and conductive heat transfer while surfaces with high IR-reflectance are prefered to reduce radiative heat transfer.

5.5.1 Rock Wool

In a fibrous material such as low density rock wool, heat transfer has two components: (i) conduction through the fibres and the intervening fluid, and (ii), radiation between the fibres. The quality of such an insulator will therefore depend on the degree to which air flow is eliminated because large cells of trapped air are conducive to prompt internal convection currents. Nevertheless, large percentages of air and less fibre imply reduced thermal bridging within the insulator.

As temperature rises, radiative heat transfer becomes more dominant because it increases approximately as the mean absolute temperature cubed. Resultantly, radiation becomes increasingly important with rising temperature. To counter this problem, high density rock wool is often used at high temperature. Alternatively inserting several layers of highly reflective metal foils (to suppress radiative heat transfer) within low density rock wool is effective at high temperature.

The problem of determining the effective thermal conductivity in porous media comes about in engineering practice quite often. Consequently, there has been considerable effort in past to develop appropriate analytical models and experimental methods [17]. For the purpose of estimating heat loss through rock wool insulation in this work, the semi-empirical [18] formula was adopted:

$$k_{eff} = 0.2572\ T^{0.81} + 0.0527\ \rho^{0.91}\ (1 + 0.0013\ T) \tag{5.8}$$

This correlation has been validated for fibrous insulations using a wide range of densities and temperatures (5 - 70 kg/m^3 and 10 - 400^{0}C respectively) and is reported to be in good agreement with measurements of rock wool products [18]. Hence, it will be adopted for application in this section.

In our case, the rock bed is a cylindrical stainless steel container with an insulation layer on the outer side as shown in figure 5.1. Heat loss to the environment from the cylindrical, top and bottom surfaces of a charged bed may be estimated from

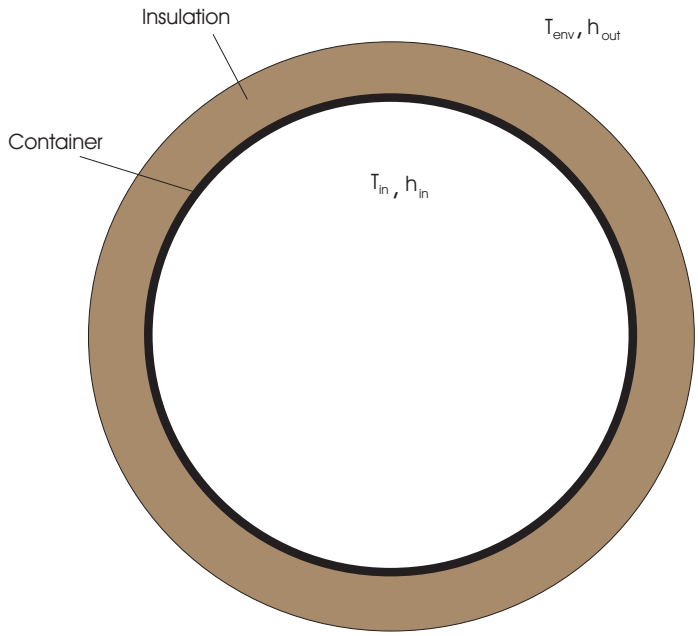

Figure 5.1: A schematic to illustrate the insulation layer on a cylindrical container. When air flow stops, $h_{in} \simeq 0$.

$$q = \frac{T_{inside} - T_{amb}}{R_{tot}} = UA(T_{inside} - T_{amb}) \tag{5.9}$$

where R_{tot} is the total thermal resistance, T_{inside} and T_{amb} are the inner-side and outer-side temperatures respectively, U is the overall heat transfer coefficient, commonly known as the U-value.

5.5.2 Radiation Shields or Metal Foils

Evacuated spaces are an effective form of insulation suitable for high temperature applications. Using a vacuum as an insulator essentially eliminates heat transfer by conduction and convection. Radiative heat loss can be minimized by applying *radiation shields*. The shields are thin, parallel, highly reflecting metal sheets or foils placed between radiating surfaces. Inserting these shields between the radiating surfaces boosts radiation resistance quite substantially and as a result, radiative heat transfer is reduced.

One construction is to use aluminium or silver foils. Spacing is usually achieved by placing a cloth-net having a large open area between the constituent fibres. Up to 20 radiation shields per centimeter [19] is possible as in the case of insulation used for cryogenic[3] storage tanks, satellites and other space vehicles. The space contain-

[3]Relating to very low temperatures.

ing these heat shields is then evacuated and sealed to eliminate possibilities of heat transport by conduction and or convection.

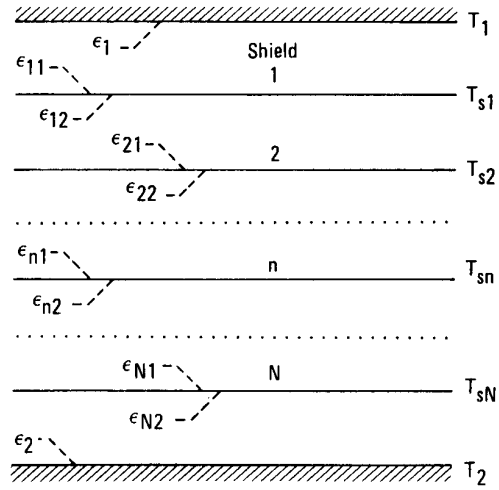

Figure 5.2: Parallel walls separated by N radiations shields. ϵ_n is the emissivity of the nth shield whose sides are named 1 and 2 for reference. Adapted from [4].

Modelling heat loss from a cylindrical bed requires different geometrical treatment for the flat surfaces (top and bottom) and curved surface. The former can be approximated by using equations for infinite parallel plates already developed in literature [4]. It can be shown that for the general case of flat parallel shields as illustrated in figure 5.2, the energy flux is given by

$$q''_{flat} = \frac{\sigma(T_1^4 - T_2^4)}{1/\epsilon_1 + 1/\epsilon_2 - 1 + \sum_{n=1}^{N}(\epsilon_{n1} + \epsilon_{n2} - 1)} \tag{5.10}$$

In practical cases, the emissivity is usually the same on both sides of each shield, and is equal for all shields in most cases, i.e $\epsilon_{n1} = \epsilon_{n2} = \epsilon_S$. This means that q''_{flat} can then be simplified to

$$q''_{flat} = \frac{\sigma(T_1^4 - T_2^4)}{1/\epsilon_1 + 1/\epsilon_2 - 1 + N(2/\epsilon_s - 1)} \tag{5.11}$$

For the special case where the wall emissivities are equal to shield emissivities i.e $\epsilon_1 = \epsilon_2 = \epsilon_s$, the previous equation can be reduced further to give

$$q''_{flat} = \frac{\sigma(T_1^4 - T_2^4)}{(N+1)(2/\epsilon_s - 1)} \tag{5.12}$$

In this case, q''_{flat} decreases as the number of shields increases. It can be shown that fractional reduction in q''_{flat} is larger when the wall ϵ are large compared to ϵ_s.

The reason being that, for small wall ϵ, the unshielded heat transfer is already low.

To estimate heat flow across the cylindrical shields forming the insulation in an evacuated system, the heat shields can be treated as infinitely long concentric cylinders, whose cross-sectional arrangement is depicted in figure 5.3. For the general case, heat flow between the walls labelled A_1 and A_2 can be estimated by

$$q''_{cyl} = \frac{\sigma(T_1^4 - T_2^4)}{1/\epsilon_1 + (A_1/A_2)(1/\epsilon_2 - 1) + \sum_{n=1}^{N}(A_1/A_{sn})(1/\epsilon_{n1} + 1/\epsilon_{n2} - 1)} \tag{5.13}$$

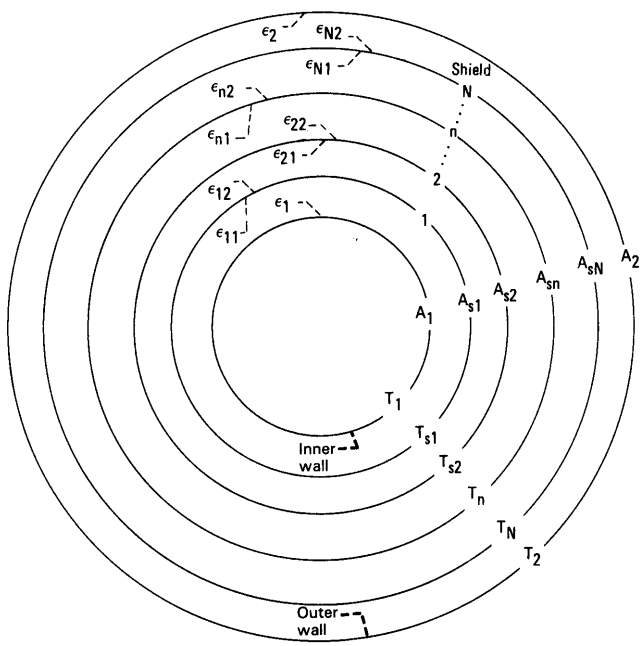

Figure 5.3: Radiation shields between concentric cylinders. A_{sn} is the surface area of the nth shield with emissivity ϵ_n. Adapted from [4].

This equation applies if both walls A_1 and A_2, and all the heat shields A_{sn} are diffuse reflectors and emitters. The other cases, for example, if the walls are diffuse and all the shields are specular, can be found in literature [4]. For estimations in this work, both walls and shields are assumed to be diffuse unless specified otherwise.

5.5.3 Insulation Quality: U-value

The general assessment of thermal insulation quality is based on the so called U-value. It is essentially a measure of the rate of heat loss through the insulation

material. To put it simply, it is the amount of heat loss through the material per square meter for every degree difference in temperature on either side of the insulation (i.e W/m^2·K). Thus, in all aspects of thermal insulation design, be it in the home or industry, one should strive for the lowest possible U-values.

The U-value is related to the total thermal resistance R_t and can be expressed as

$$\sum R_t = \frac{1}{U} \tag{5.14}$$

In our case, contributions due to radiation and conduction, to the effective heat current from the inside of the storage tank to the ambient are considered to be in parallel. The convenience of using U-value is that, heat loss can be expressed analogous to Newton's law of cooling:

$$q = UA\Delta T \tag{5.15}$$

where ΔT is the temperature difference between the ambient and the inside part of the bed. Although heat flow is multidimensional, in our case, a one-dimensional approach yields to a reasonable approximation if it is assumed that surfaces normal to the direction of heat flow are isothermal and that surfaces parallel to the direction of heat flow are adiabatic.

The determination of the U-value can be rather difficult, and as such, it is among the many applications for which it is convienient to express the net radiation exchange in the form

$$q''_{rad} = h_r A(T_s - T_{sur}) \tag{5.16}$$

where the radiation heat transfer coefficient h_r is given by

$$h_r = \epsilon\sigma(T_s + T_{sur})(T_s^2 + T_{sur}^2) \tag{5.17}$$

In this case, T_s and T_{sur} are the surface and surroundings' temperatures respectively. The radiation heat transfer mode as expressed by equation (5.16), is linearized in a manner similar to convection. This conveniently makes the heat rate proportional to the temperature difference rather the difference between the two temperatures raised to the fourth power. Nevertheless, h_r strongly depends on temperature unlike the convection coefficient which generally has a weak dependence on temperature. For concentric cylindrical heat shields as those applicable to our case (see figure 5.3), the temperature of the nth shield (all diffuse) is given by

$$T_n^4 = T_1^4 \; - \; \frac{(T_1^4 - T_2^4)\left[\frac{1}{\epsilon_1} + \frac{A_1}{A_{s1}}\left(\frac{1}{\epsilon_{s11}} - 1\right) + B1\right]}{B2} \tag{5.18}$$

where

$$B1 = \sum_{n=1}^{n-1} \frac{A_1}{A_{sn}} \left[\frac{1}{\epsilon_{n2}} + \frac{A_{sn}}{A_{s(n+1)}} \left(\frac{1}{\epsilon_{(n+1)1}} - 1 \right) \right]$$

$$B2 = \frac{1}{\epsilon_1} + \frac{A_1}{A_2} \left(\frac{1}{\epsilon_2} - 1 \right) + \sum_{n=1}^{N} \frac{A_1}{A_{sn}} \left(\frac{1}{\epsilon_{n1}} + \frac{1}{\epsilon_{n2}} - 1 \right)$$

There exists some kind of analogy between the diffusion of heat and that of electrical charge. In concept, resistance is the ratio of a driving potential to the corresponding transfer rate. Based on this concept, it can be shown that thermal resistance due to conduction in a plane wall is given by

$$R_{t,cond} = \frac{L}{kA} \tag{5.19}$$

For a cylindrical wall, the corresponding expression takes the form

$$R_{t,cond} = \frac{ln(r_2/r_1)}{2\pi Lk} \tag{5.20}$$

The thermal resistance due to radiation may be defined as

$$R_{t,rad} = \frac{1}{h_r A} \tag{5.21}$$

while thermal resistance caused by convection is given by

$$R_{t,conv} = \frac{1}{hA} \tag{5.22}$$

These expressions for thermal resistance were then used to estimate the total resistance from which the corresponding U-values were derived. In our case, where the temperature difference between a charged rock bed and the environment is to the order of 400°C, the U-value has to be quite low in order to achieve effective thermal storage, in which case, U-values much less than 0.1 are desirable.

The U-values of a compact evacuated thermal insulation regime with aluminium or silver heat shields is shown in figure 5.4. Corresponding U-values for the flat surfaces are to the same order although there are slightly higher. It can be seen that, for the cheaper Al-foils, about 10 shields will yield to a U-value of 0.05 W/m^2·K while just 2 foils of silver can yield to U-values as low as 0.03 W/m^2·K. However, high costs associated with silver is the major prohibitive factor for its adoption in many applications where system costs play an important role.

A suitable and probably much cheaper option would be to use the rather bulk rock-wool insulation, if need be, inserted with evenly spaced aluminium foils as explained

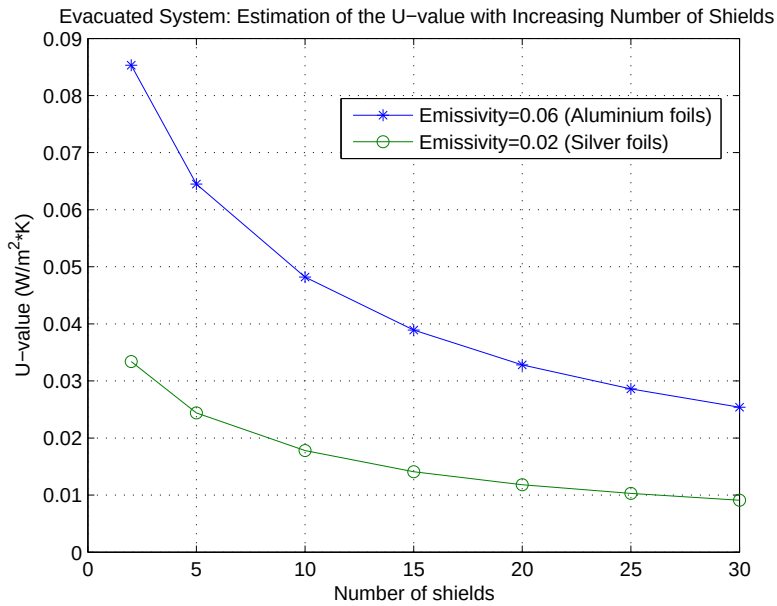

Figure 5.4: Plot showing the estimated variation of the U-value of an evacuated insulation system consisting of Al/Ag-foils, with a spacing of 0.5 mm. The temperature inside the bed is taken to be 400°C, while ambient temperature is 20°C. Values for the emissivities shown were adapted from [20], see table 5.1 for rock bed parameters and dimensions.

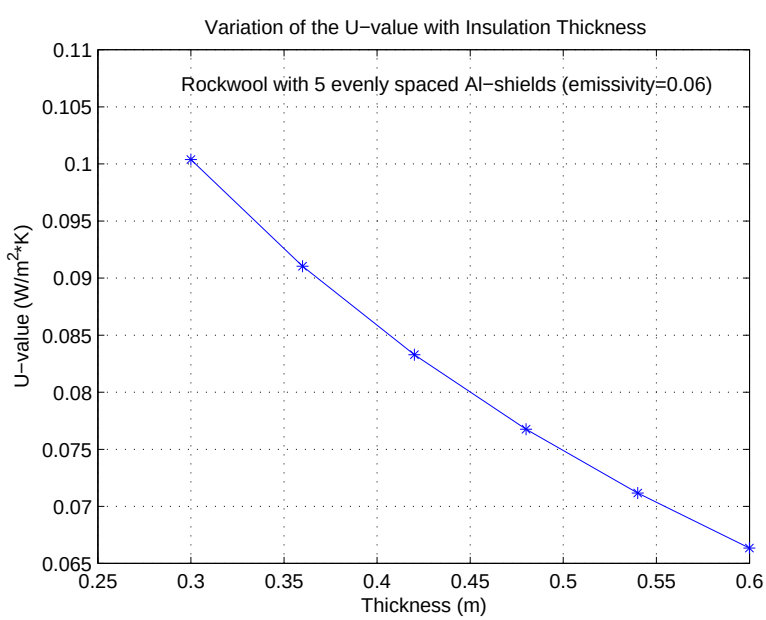

Figure 5.5: Plot showing the estimated variation of rockwool U-values with insulation thickness for cylindrical rock bed container, see table 5.1 for rock bed parameters and dimensions. To reduce radiative heat transfer, the model assumes that 5 evenly spaced Al-foils are inserted.

earlier. The Al-foils are meant to reduce radiative heat transfer. In order to get an idea of its performance at high temperature, let us consider the U-value of an insulation thickness of 0.5 m. The results of simulating such insulation are shown in figure 5.5.

It can be seen from figures 5.5 and 5.4 that although the more complicated evacuated insulation system is compact and offers better performance, rock wool insulation with aluminium foils inserted within can perform fairly well. In this example, a 50 cm layer of commercially available insulation yields to a U-value to the order of 0.075 W/m^2·K. The advantage of this alternative is that components are commercially available at fairly low prices. In addition, there is less sophistication to this technique as compared to the fabrication of an evacuated system, as such, it should be possible to manufacture this kind of insulation easily in developing countries.

5.5.4 The Cooling Rate

It is also important to have estimates in terms of heat loss in relation to the change of the internal energy of the rock bed. Assuming that the air is always well mixed and that the bed is at uniform temperature, the cooling rate is equal to the instantenous heat loss. Considering a cylindrical bed at any time t, this relation can be expressed as

$$-(1-\gamma)(\rho V c_p)_b \frac{dT_b}{dt} = UA(T_b - T_{sur}) \tag{5.23}$$

where T_b is temperature inside the bed as before. Knowledge of the remaining quantity and temperature-wise quality of energy is important for the daily consumption energy budget. Integrating and evaluating equation (5.23), the bed temperature at any time t can be estimated by

$$T_b(t) = T_{sur} + (T_{b,t=0} - T_{sur})\ e^{-\frac{UA}{(1-\gamma)\rho V c_p}\ t} \tag{5.24}$$

Figure 5.6 shows the estimated cooling rate with storage time for a cylindrical rock bed insulated by a 0.5 m thick rock wool layer. Five evenly spaced Al-foils are inserted within the said thickness. It can be seen that with this kind of insulation, the bed temperature is expected to be slightly below 330°C after 4 days if the U-value is to the order of 0.075 W/m^2·K and the temperature inside the bed initially at 400 ^{o}C. In other words such insulation should be sufficient to satisfactorily insulate the storage for about 3 days. Essentially, this is a reasonable storage period for the concentrating system under discussion.

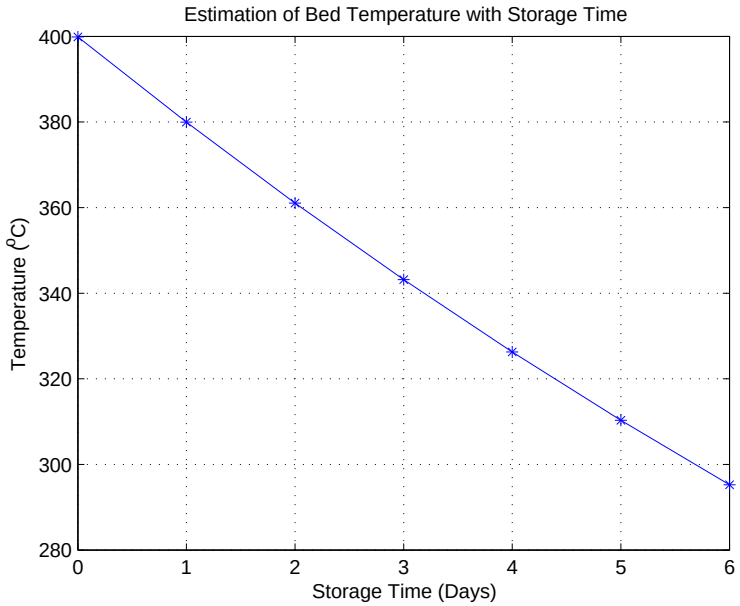

Figure 5.6: This plot shows the estimated cooling rate with storage (see table 5.1 for rock bed parameters and dimensions) time for the insulation layer whose U-value $\simeq$ 0.075 W/m^2·K and corresponding to an insulation thickness of 50 cm, see figure 5.5.

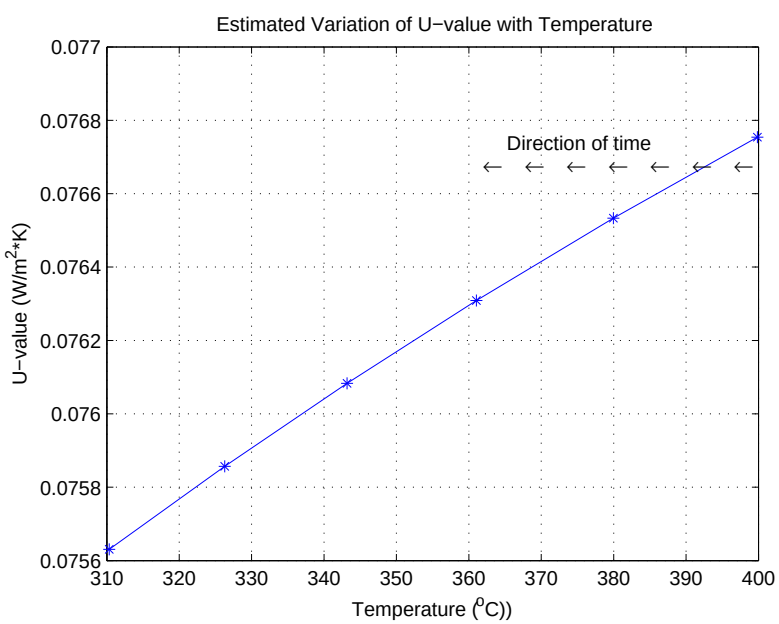

Figure 5.7: This plot shows the dependence of the U-value with temperature as the cylindrical rock bed (see table 5.1 for rock bed parameters and dimensions.) cools with time. Starting from 400 down to about 310 ^{o}C, the time interval between successive points is equal to a day.

In carrying out simulations for rockwool as done in modelling the cooling rate shown in figure 5.6, the dependence of the U-value on temperature as determined by equations 5.8 and 5.17 needs to be taken into account. Such a dependence of the U-value on temperature (and therefore on time in this case) is shown in figure 5.7. It can be seen that the general trend is an improvement in the U-value as the temperature decreases. However, the variation seems to be quite marginal.

5.6 Air Transport in Pipes

Air will be sucked from the receiver to the storage through an insulated pipe by means of a fan. This is a typical internal-flow problem in fluid mechanics. Intuitively, the pressure drop parameter is of prime importance as it determines the pump/fan power requirements. The pressure drop associated with axial positions from x_1 to x_2 in a circular pipe can be expressed as

$$\Delta p = -\int_{p_1}^{p_2} dp = F\,\frac{\rho\bar{u}^2}{2D}\int_{x_1}^{x_2} dx = F\,\frac{\rho\bar{u}^2}{2D}\,(x_2 - x_1) \tag{5.25}$$

where $\bar{u}$ is the mean fluid velocity, D is in this case, the inner diameter of the tube and F is the friction factor.

In principle, the friction factor is a function of the surface condition of the tube and the Reynolds number. It is a minimum for smooth surfaces and increases with increasing surface roughness. Friction factor data is readily available in literature usually given in the form of the so called *Moody Charts* [43]. However, correlations that reasonably approximate F for smooth surface conditions also exist and those that can provide acceptable estimates for this work are:

$$F = \frac{64}{Re_D} \qquad for\ laminar\ flow \tag{5.26}$$

$$F = 0.316\ Re_D^{-0.25} \qquad for \qquad Re_D \leq 2\times 10^4 \tag{5.27}$$

$$F = 0.184\ Re_D^{-0.2} \qquad for \qquad Re_D > 2\times 10^4 \tag{5.28}$$

The fan power required to overcome the resistance to flow associated with the pressure drop as defined by equation 5.25 is given by

$$P_B = \Delta p\ (\dot{m}/\rho_{air}) \tag{5.29}$$

For the insulation of the air transport tubes, the discussions treated in section 5.1 apply. The total heat transfer rate to ambient (heat loss) irrespective of the nature of surface thermal or flow conditions, in a section of the tube is determined by

$$q = \dot{m}c_p(T_{m,i} - T_{m,o}) \tag{5.30}$$

where $T_{m,i}$ and $T_{m,o}$ are the inlet and outlet (in a segment of the pipe) mean air temperatures respectively. In order to estimate heat loss along the tube, it is a reasonable approximation to divide the tube into smaller segments that are each assumed to be isothermal. Energy balance equations can then be established for steady state conditions.

As a general guide for construction, the air transport pipes should be as short as possible but reasonably wide in order to reduce pressure drop and or heat loss. As depicted by the correlations determining the friction factor, pressure drop in pipes is a strong function of flow regimes (laminar or turbulent) while the heat loss depends on the quality of the insulation wrapping the pipe. The decrease in temperature as the air flows through a segment can be estimated by

$$T_{m,o} = T_{m,i} - \frac{UA\Delta T}{\dot{m}c_p} \tag{5.31}$$

5.7 Modelling of High Temperature Rock Bed Storage

5.7.1 Air-Rock System: The Governing Equations

Several heat transfer studies have been done on the heating and cooling of packed beds, see for example works by [21, 22, 23, 24]. Most of these studies are based on the Schumann model [25]. The basic assumptions on which the model is premised are: one dimensional flow, no axial conduction/dispersion, no mass transfer, constant properties, zero temperature gradients within solid particles and negligible heat loss to the ambient. The governing differential equations for the fluid and bed temperatures are given by,

$$(\rho c_p)_\infty \, \gamma \, \frac{\partial T_\infty}{\partial t} = -\frac{(\dot{m}c_p)_\infty}{A} \, \frac{\partial T_\infty}{\partial x} + h_v(T_b - T_\infty) \tag{5.32}$$

$$(\rho c_p)_b \, (1-\gamma)\frac{\partial T_b}{\partial t} = h_v(T_\infty - T_b) \tag{5.33}$$

where the subscripts b and ∞ are used here to signify bed and fluid respectively, the other terms have their usual meanings as discussed in this work. For an air-rock system, the instantaneous change in temperature will be insignificant, thus, the first term in equation (5.32) is negligible, such that the equations can be written as

$$\frac{\partial T_\infty}{\partial (X/L)} = NTU(T_b - T_\infty) \tag{5.34}$$

$$\frac{\partial T_b}{\partial \vartheta} = NTU(T_\infty - T_b) \tag{5.35}$$

where NTU stands for 'Number of Transfer Units' and is given by

$$NTU = \frac{h_v AL}{(\dot{m}c_p)_\infty} \tag{5.36}$$

and the dimensionless time ϑ, is given by

$$\vartheta = \frac{t(\dot{m}c_p)_\infty}{(\rho c_p)_\infty (1-\gamma)AL} \tag{5.37}$$

In the above equations, A and L are the cross-sectional area and length of the bed respectively. A pragmatic approach in solving the above equations typically requires the employment of numerical techniques.

For the development of a numerical solution, the bed is discretized into N sections of depth ΔX that are each assumed to be isothermal, such that $N = L/\Delta X$. The unabsorbed thermal energy in the air has an exponential temperature profile determined by the factor, $e^{-NTU(\Delta X/L)}$. Therefore the energy removed from the air and transfered to the rock-bed in section i of depth ΔX can calculated as

$$(\dot{m}c_p)_\infty (T_{\infty,i} - T_{\infty,i+1}) = (\dot{m}c_p)_\infty (T_{\infty,i} - T_{b,i})(1 - e^{-NTU(\Delta X/L)}) \tag{5.38}$$

An energy balance, that considers loss to the ambient of the rock pebbles within region ΔX can be expressed as

$$\frac{dT_{b,i}}{d\vartheta} = N(T_{\infty,i} - T_{b,i})(1 - e^{-NTU(\Delta X/L)}) + \frac{(U\Delta A)_i}{(\dot{m}c_p)_\infty}(T_{sur} - T_{b,i}) \tag{5.39}$$

where $(U\Delta A)$ defines the area-loss coefficient product for node i.

5.7.2 The Charging Process

The transient behavior of packed beds for both the charging and discharging modes is of fundamental significance, not only with respect to the achievement of best designs but also with respect to their optimal operation. For the charging cycle, the rock bed is heated up by the convective hot fluid (air) flowing through it while the latter is simultaneously cooled down.

To simulate the charging process, the recommended [26] approach to solve equation-(5.39) involves replacing the time derivative by $(T_{b,i}^{+} - T_{b,i})/\Delta\vartheta$ and bed temperatures on the right-hand side of the same by $(T_{b,i}^{+} + T_{b,i})/2$. In this case, the superscript

'+' on temperature (i.e T_b^+) is employed to indicate the new temperature in a transient process, such that T_b is the previous time temperature. Making the necessary substitutions in equation (5.39) yields to

$$\frac{(T_{b,i}^+ - T_{b,i})}{\Delta\vartheta} = N\left(T_{\infty,i} - \frac{T_{b,i}^+ + T_{b,i}}{2}\right)(1-e^{-NTU(\Delta X/L)}) + \frac{(U\Delta A)_i}{(\dot{m}c_p)_\infty}\left(T_{sur} - \frac{T_{b,i}^+ + T_{b,i}}{2}\right) \tag{5.40}$$

With the initial conditions known for all $T_{b,i}$ (i.e for $i = 1, 2, 3, ...N$), calculations for T_b^+ in a transient process, say charging, start at node 1 (see figure 5.8) where the inlet fluid temperature is already known (supposedly from the volumetric air-receiver in our case). The outlet fluid temperature from node 1, which in practice, becomes the inlet fluid temperature for the succeeding node, is determined using equation (5.38).

For long-term performance predictions, the use of the infinite NTU model, in which the bed and fluid temperatures are virtually equal everywhere, is recommended. However, the present model is concerned with short-term charging and discharging modes at high temperature. All the same, long term-performance of packed beds at low temperature is adequately treated in literature, see for example [28].

The assumption that the temperature gradients within the rock pebbles are not significant can be relaxed by using a corrected NTU_c as proposed by Jeffreson [29]:

$$NTU_c = \frac{NTU}{1 + Bi/5} \tag{5.41}$$

where $Bi = \bar{h}R_r/k_b$, popularly known as the Biot number[4] in heat transfer texts. In this case, R_r is the equivalent of the average radius of the rock pebbles of thermal conductivity k_b, and $\bar{h}$ is the convective heat transfer coefficient at the surface of the pebbles and can be determined from McAdams correlation [30]. The latter is given by

$$\bar{Nu} = \frac{\bar{h}D_r}{k_f} = 0.37\ Re^{0.6} \qquad for \qquad 17 < Re < 70\ 000 \tag{5.42}$$

where k_f is the conductivity of the air evaluated at film[5] temperature T_f.

5.7.3 Extrapolation of the Thermophysical Properties of Air

Given the large temperature differences which the air experiences as it travels through the packed bed, it is imperative that its thermophysical properties be adjusted (subjective to the temperature changes) with time and position along the bed during the

[4]For $Bi < 0.1$, the temperature gradients within the rock pebbles can be ignored.
[5]$T_f = \frac{T_b + T_\infty}{2}$

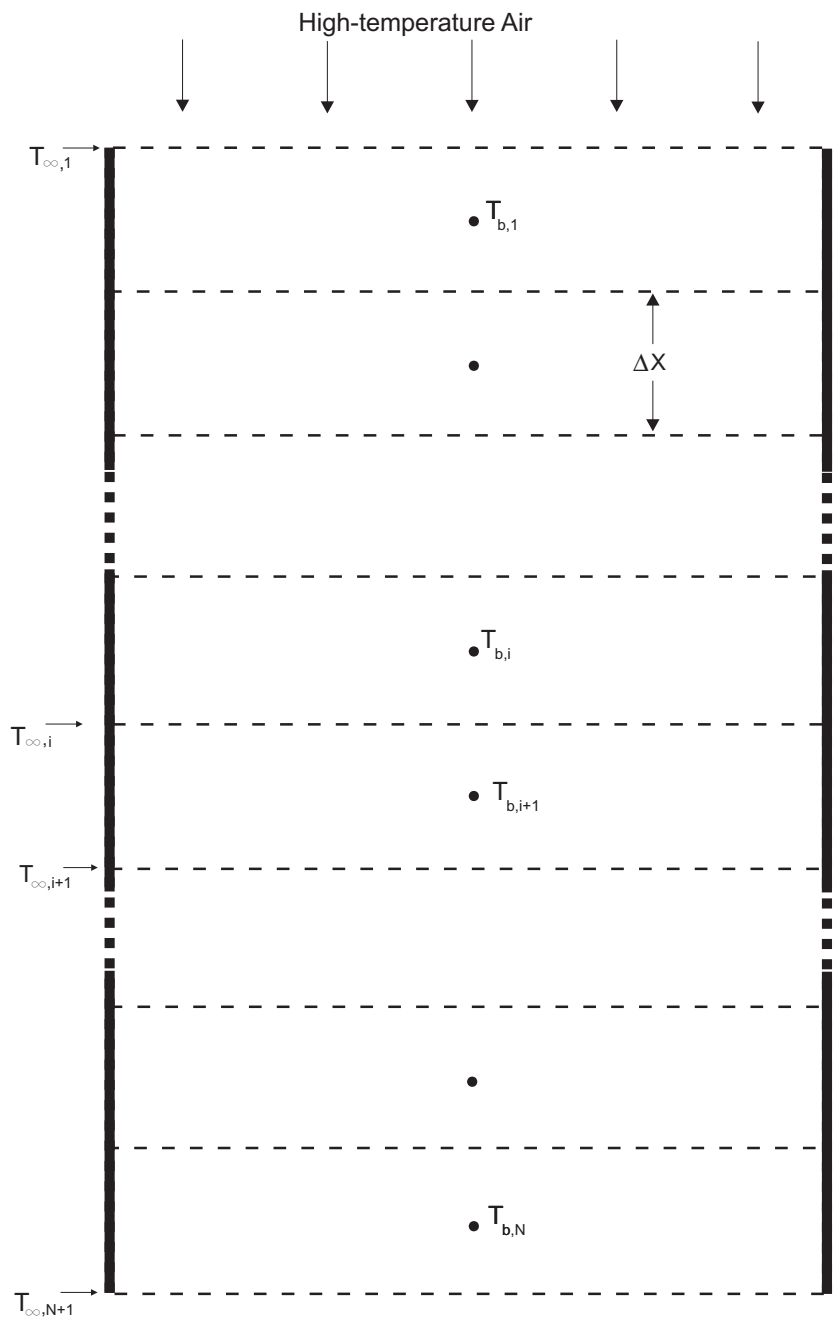

Figure 5.8: A schematic to illustrate a Packed Bed Storage unit divided into N segments. In our model, the length of each segment , is such that the bed temperature is considered to be uniform. Adapted from Duffie and Beckman [28].

charging process. In our model, this was achieved by plotting data available in Heat Transfer literature (from [31]), and then determine the corresponding polynomials (for the thermophysical property in question) using the *Polynomial Curve Fitting* tool in MATLAB. An example is given in figure 5.9 while the rest are summarized in appendix C.

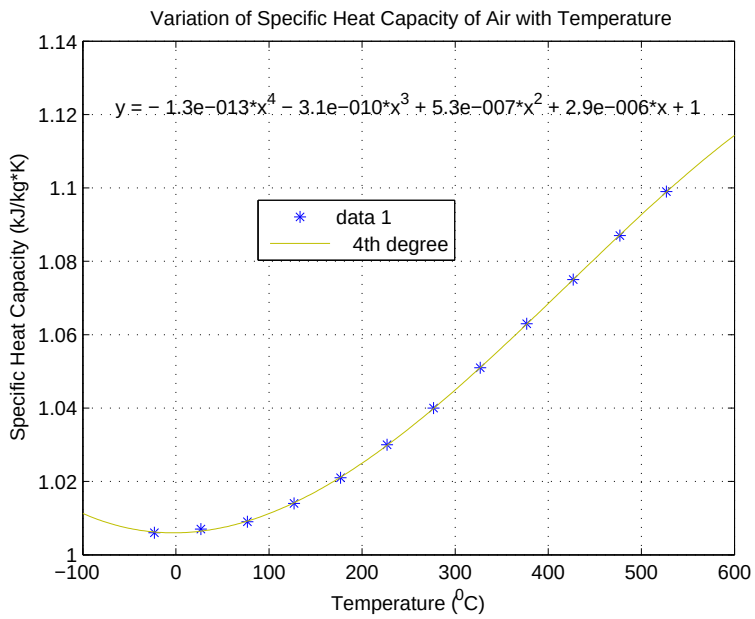

Figure 5.9: Plot illustrating a poly fit that simulates the variation of the specific heat capacity of air with temperature. For the polynomial shown on the plot, x represents temperature while the dependent variable y represents the specific heat capacity.

To reduce their complexity, the said 'Poly fits' are valid only within the confines of interest, i.e $0 \leq T \leq 500$ ^{o}C. The same technique was used to derive the necessary polynomials to model the remaining thermophysical properties of air that includes: specific heat capacity, prandtl number, thermal conductivity, the absolute and kinematic viscosity. This facilitated their adjustment both with temperature, in modelling the transient process of adding heat to the rock pile.

5.7.4 Pressure Drop and Blow Power

The performance of the rock bed storage system is influenced by various design and operational parameters such as size of rock, size of bed, air mass flow rate, void fraction within the rock bed, thermophysical properties of the rock-pebbles and the convective fluid. Of primary importance to all air-rock thermal storage systems are their heat transfer and pressure drop characteristics [32]. The pressure drop

across the packed bed is necessary to estimate the minimum blow power needed to overcome it. The contribution of each layer as shown in figure 5.8 can be found by an adaptation of the correlation proposed by Duffie and Beckman for pressure drop calculations in packed beds. In our case the pressure drop in segment i is given by

$$\Delta p_i = \frac{\Delta X G_i^2}{\rho_{air,i} D_r} \left(21 + 1750 \frac{\mu_i}{G_i D_r} \right) \tag{5.43}$$

where G is the mass velocity, μ is the viscosity of air and D_r is the average particle diameter[6]. The total pressure drop across the bed can therefore be found by adding up contributions from each layer i.e

$$\Delta p_{total} = \sum_{i=1}^{N} \Delta p_i \tag{5.44}$$

Application of the conservation of mass implies that, for the achievement of constant volumetric flow rate $\dot{V}_i$ along the bed, the air velocity is expected to vary subject to changes in the air density if the porosity and bed cross-sectional area are assumed to be uniform. Consequently, for each segment the blow power $P_{B,i}$ necessary to overcome the local pressure drop ΔP_i in a segment i can be computed by

$$P_{B,i} = \dot{V}_i \Delta p_i \tag{5.45}$$

Therefore the minimum fan-power ($P_{B,min}$) output is the sum based on the contributions from all the segments and can be estimated by

$$P_{B,min} = \sum_{i=1}^{N} P_{B,i} \tag{5.46}$$

The computer programme developed to simulate the transient processes essentially should be able to go adjusting all the temperature dependent variables and thermophysical properties of air for each segment at the beginning of the chosen time interval. This way, it will be possible to study issues of concern like pressure drop, the minimum fan power and temperature profile with appreciable quality of resemblance to the real system.

5.7.5 Energy Input and Other Parameters

Since the present research is also aimed at assessing its potential for use in Zimbabwe, the energy input to the charging mode has been derived from results discussed in chapter 2, i.e, data for the distribution of normal beam estimates for the monthly

[6]The average particle diameter, in this case, is understood to be the equivalent diameter of a spherical particle having the same volume.

average daily radiation was used as the input. For example, the estimated distribution of the monthly average daily beam radiation in August for the second largest city in Zimbabwe called Bulawayo, is shown in figure 5.10.

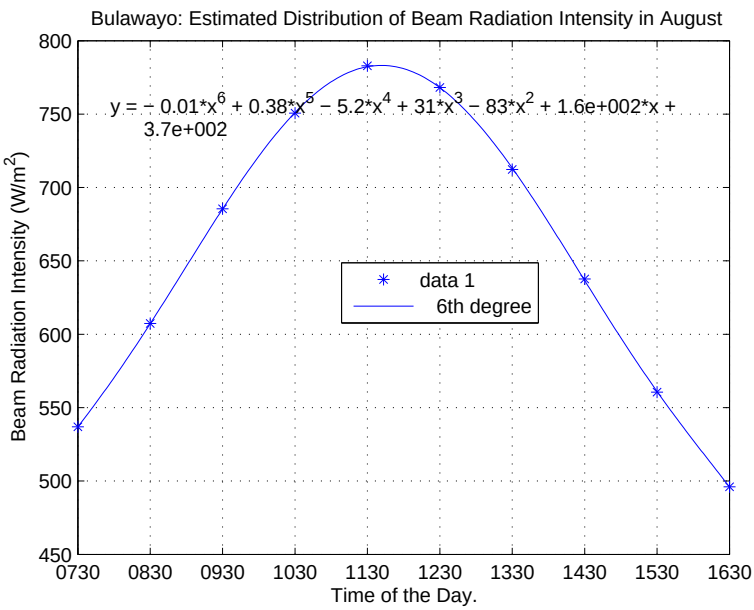

Figure 5.10: A plot showing the estimated distribution of beam radiation intensity in August for Bulawayo, Zimbabwe. Monthly average daily beam insolation is considered.

A time dependent polynomial that represents the bean distribution is then determined and applied to the simulation programme. As mentioned before, the solar collector in our case is a high reflectance parabolic dish 'concentrating' the beam radiation (I_b) onto a volumetric absorber which then passes the energy to the air as heat at a certain efficiency. The energy finally reaching the heat storage can therefore be determined using the following expression:

$$\dot{m}\ c_p\ \Delta T = I_b \cdot A_a \cdot \rho_{ref} \cdot \tau_g \cdot \eta_{abs} \tag{5.47}$$

where ρ_{ref} is the mirror reflectivity, A_a the aperture area, τ_g the transmitivity of the receiver's glass cover and η_{abs}, the efficiency of the absorber. In this case, ΔT is the difference between the outlet and inlet air temperature as the it flows through the absorber.

It is important to note that outdoor conditions present a practical problem, which primarily rests on the dependence beam radiation on various factors like: presence or absence cloud cover, the intensity of the incoming radiation as a function of time of the day, etc. The fundamental challenge boils down to one of supplying hot air at

constant (or increasing) temperature to the storage. The modelling results are now presented for the set of input values shown in table 5.1. The beam input data used here is the monthly average daily radiation (August) for Bulawayo, Zimbabwe.

CHARGING PROCESS: INPUT PARAMETERS

PARAMETER	VALUE	UNIT
Parabolic Collector		
Aperture Diameter	1.1	m
Rock Bed		
Diameter	0.50	m
Height	1.00	m
Porosity	0.40	-
Storage Material: Granite		
Approx. diameter of pebbles	0.02	m
Specific heat capacity	775	J/kg·C
Density	2630	kg/m^3
Thermal Conductivity	2.79	W/m^{-1}·C^{-1}
Initial Temperature of pebbles	20	^{o}C
Convective Fluid: Air		
Mass flow rate	$f(t)$ or constant	kg s^{-1}
Inlet air temperature	constant if $\dot{m} = f(t)$	^{o}C
Specific heat capacity	$f(T)$	J/kg·C
Density	$f(T)$	kg/m^3
Thermal Conductivity	$f(T)$	W/m^{-1}·C^{-1}
Prandtl number	$f(T)$	-
Kinematic viscosity	$f(T)$	m^{2}s^{-1}

Table 5.1: This table summarizes the main input parameters used to model the transient behavior of rock bed storage. In this case, $f(T)$ indicates that the value of the corresponding input parameter is a function of temperature, while $f(t)$ signify time dependence as depicted in figure 5.10 and can be determined using equation (5.47), in which case, the following assumptions have been made: $\rho_{ref} = 0.9$, $\tau_g = 0.9$ and $\eta_{abs} = 0.75$

5.7.6 Effective Thermal Conductivity During Storage

During storage, the system under discussion can be regarded as a container packed with rock pebbles in a static gas at some pressure. Heat transfer mechanisms at high temperature in such a bed are of great interest to this study. Knowing the thermal effective conductivity is essential to allow the study of the thermal behavior of the

storage system. Nonetheless, making accurate measurements on test beds is complex and expensive in terms of both costs and time [33]. Resultantly, considerable effort has gone into developing models[7] that can predict the effective thermal conductivity, see a recent review by [34].

However in our case, where only estimates of the extent of the thermal degradation are important, a simplified model is sufficient. For the development of such a model, the following assumptions were made: regularly (layers in which one pebble is placed on top of the other) and tightly packed spheres, one-dimensional heat gradient in the vertical direction, contact area is negligible such that heat transfer between spheres is principally a contribution of conduction by a thin layer of air within the vicinity of the contact point, and also by radiation. These two heat transfer mechanisms are understood to be in parallel. A simplified model tailored to predict the effective thermal conductivity k_{eff} for our system can be approximated by

$$k_{eff} = 4\Big[\frac{\chi\ k_{rock}}{2} + \left(\frac{2}{k_{rock}} + \frac{1}{\varepsilon\sigma T^3 D_r}\right)^{-1}\Big] \tag{5.48}$$

where D_r is the average particle diameter and $\chi = k_{air}/k_{rock}$, in which case, the dependence of k_{air} on temperature is depicted in figure 7.1 in the appendix. The corresponding variation with temperature of k_{eff} as defined by equation (5.48) is shown in figure 5.11.

When compared (using the same set of data) with other models in a recent review by Jianhua et al. [34], our model gives relatively higher values, on average, by a factor of two, especially for low temperatures. However, somewhat higher values for k_{eff} are acceptable in our case, as they will yield to conservative estimates (predictions) regarding system performance.

5.8 Results and Discussion

The process of adding sensible heat energy to the bed can be done in two ways: (i) either by making the mass flow rate constant and then let the storage inlet air temperature subject to variations in beam intensity as defined by equation 5.47 or (ii) by controlling $\dot{m}$ such the inlet air temperature to the storage remains constant. The results for these two options are now presented separately.

[7]The majority of these models are quite complicated.

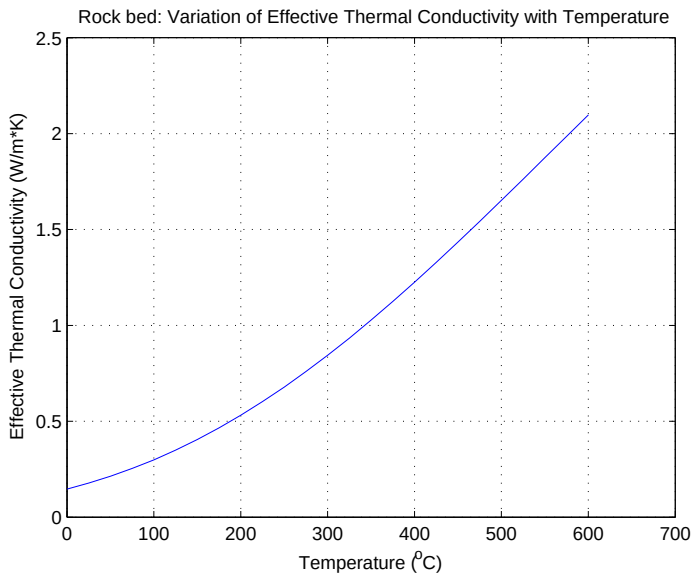

Figure 5.11: This plot shows the variation with temperature of the effective thermal conductivity of a packed bed as predicted by our model, represented by equation 5.48. In this case, $k_{rock} = 2.79$, $D_r = 0.02$ m, $\varepsilon = 0.9$ and k_{air} varies with temperature as shown in figure 7.2.

5.8.1 Constant Mass Flow Rate

The results of keeping $\dot{m}$ constant and then let beam intensity determine the storage inlet air temperature is shown in figure 5.12. It can be seen that with this option, the inlet air temperature to the storage increases with beam intensity until it reaches a maximum at solar noon. After this point, supposedly on a clear day, the inlet air temperature decreases with falling beam intensity as depicted in figure 5.10.

It is evident that, in this mode stratification is initially poor and the risk of exceeding safe temperatures is high and therefore, operation should be strictly monitored. As can be seen, it suggests that whenever the radiation intensity drops, the inlet air temperature lowers. Consequently this will start cooling the bed in general and will even drive the hottest section deeper into bed and undesirably further from the top. However, operation at a fixed mass flow rate implies less sophistication to the system, and as such, this mode is ideal for application in regions characterized with a high frequency of sunny days

5.8.2 Constant Inlet Air Temperature

The preferable and more pragmatic operation mode is to let $\dot{m}$ vary as a function of the incoming beam radiation and controlled such that the inlet air temperature

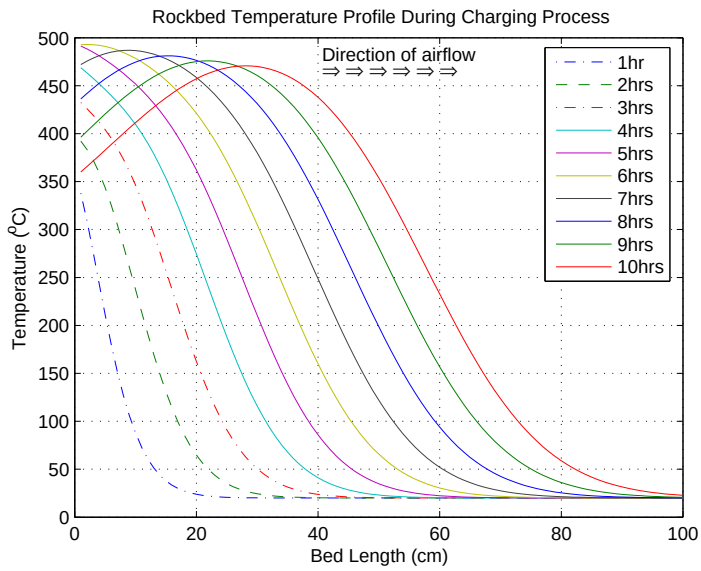

Figure 5.12: This plot shows the expected transient behavior of a rock bed (see table 5.1 for rock bed parameters and dimensions), the input of which is as depicted in figure 5.10. The air mass flow rate is maintained constant at 0.004 kg/s, while storage inlet air temperature is let to vary as determined by variations in beam intensity.

to the storage is constant, say at 400 ^{o}C. The results are shown in figures 5.13. The plot shows a fairly well stratified temperature distribution through out the whole bed.

From the programme, it could be shown that further stratification can be achieved by reducing the diameter of the pebbles, but pebble size reduction is expensive in terms of blow power. More importantly, this option implies that a device that controls mass flow rate in order to maintain the inlet air temperature stable is very important. This might bring some kind of sophistication to the system and might require additional costs, compared to the alternative of using a system where $\dot{m}$ is maintained constant. However, as a first approach, fan operation through a solar cell directly powered by beam radiation should be investigated. The solar cell could be conveniently attached to the side of the dish (lying parallel to the aperture plane) so that it tracks the sun together with the collector.

5.8.3 Pressure Drop Comparisons

When Mass Flow Rate is Kept Constant

A careful look on the pressure drop plot marked curve-1 in figure 5.14 reveals an apparently over stretched S-shape. This is because between morning and noon, the

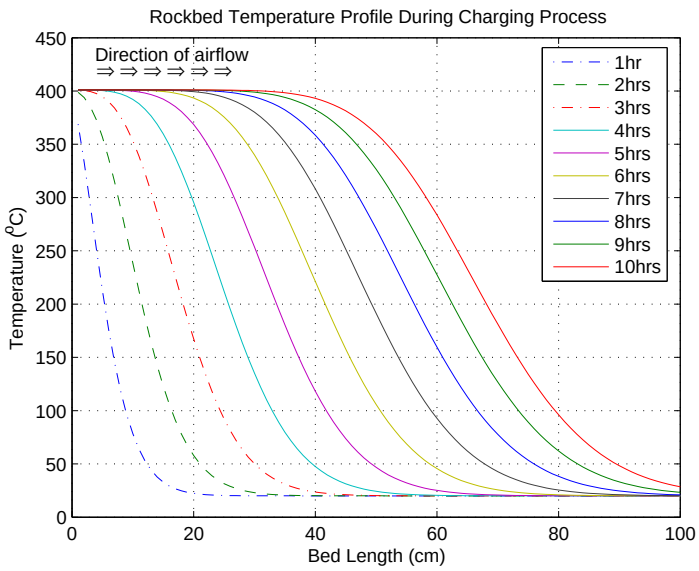

Figure 5.13: This plot shows the expected transient behavior of charging a rock bed (details summarized in table 5.1), the input of which is as depicted in figure 5.10. The bed inlet air temperature has been fixed at 400°C while $\dot{m}$ changes as determined by the variations in beam intensity.

air density decreases with rising air temperature while viscosity increases. The resultant effect is a somewhat exponential rise in the pressure drop. The increase in the charged portion of the bed also contributes to this rise. However, after the solar peak, the inlet air starts getting colder and colder as radiation intensity drops. Resultantly the bed temperature will also begins to fall in general. This will consequently cause the rate of increase in pressure drop to start slowing down accordingly. However, in this case, assuming a linear variation in pressure drop would be an acceptable approximation for practical purposes.

When Mass Flow Rate Varies

Since the inlet air temperature is kept constant (Curve-2 in figure 5.14), the pressure drop in this case is influenced largely by the variations in the mass flow rate, and to a lesser extent, by the portion of the bed that is charged. Between morning and solar noon, as depicted in figure 5.10, $\dot{m}$ must obviously accelerate in order to maintain inlet air temperature constant. At solar noon, $\dot{m}$ has its maximum value which in turn imply a maximum in the pressure drop. The lack of symmetry on the pressure drop curve is due to less influential contribution from the growing fraction of the bed that is charged.

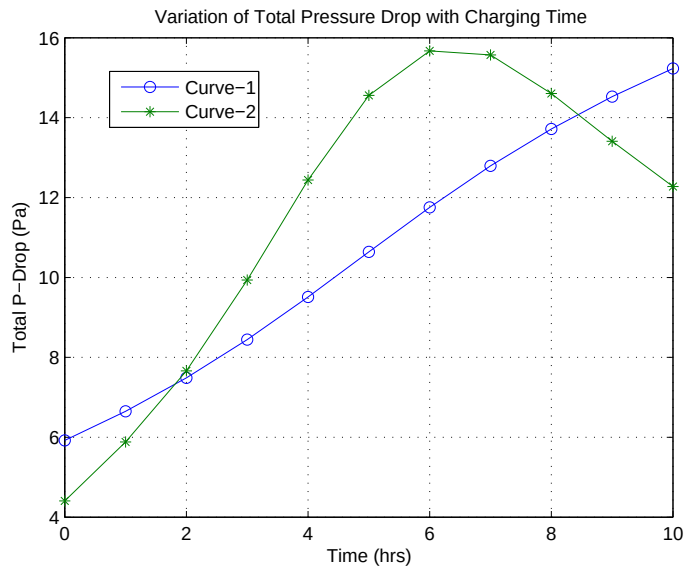

Figure 5.14: Pressure drop plots corresponding to the set of data used for figure 5.12 and 5.13. Curve-1 is a result of charging the bed with a fixed mass flow rate (0.004 kg/s) but variable inlet air temperature. The same parameters are reversed for Curve-2, i.e inlet air temperature is kept constant (400 ^{o}C) while mass flow rate is allowed to vary accordingly.

5.8.4 Thermal Degradation With Storage Time

Apart from heat loss to the ambient, the temperature of a not-fully charged bed will degrade with time as the bed will naturally try to establish thermal equilibrium. It is necessary to be able to estimate the extent of thermal decay in cases where extraction of the heat energy is done after several hours of storage. The performance of the system, in regards to the type of application (essentially cooking and boiling) under pursuit in this study, largely depends on high temperature, in which case, thermal degradation becomes significant with storage time.

The results of simulating the variation of the temperature profile with storage time for rock beds of the same size and initially charged as depicted in figures 5.12 and 5.13, are shown in figures 5.15 and 5.16 respectively. As can be seen, the rate of destratification (or thermal degradation) within the colder region is rather sluggish at the beginning but increases as the temperature rises. On the other hand, the destratification process is rather fast in the region of high temperature, as can be seen by the evening-out of the 'thermal-hump' (in figure 5.15) in just about 3 hours. Apart from the steep temperature gradients at the start, the behavior of the temperature profile with storage time, of an unfully-charged bed is strongly influenced by the variation of k_{eff} with temperature along the bed (and therefore with time in this case).

In addition, when air flow stops presumably at the end of the charging process, a situation in which cooler segments are located above the thermal-hump in figure 5.12, arises. The resultant imbalances in the air density (and thus buoyant forces) within these two regions are expected to offset a somewhat localized convectional current that will hasten the establishment of thermal equilibrium if the storage is not disturbed for some few hours.

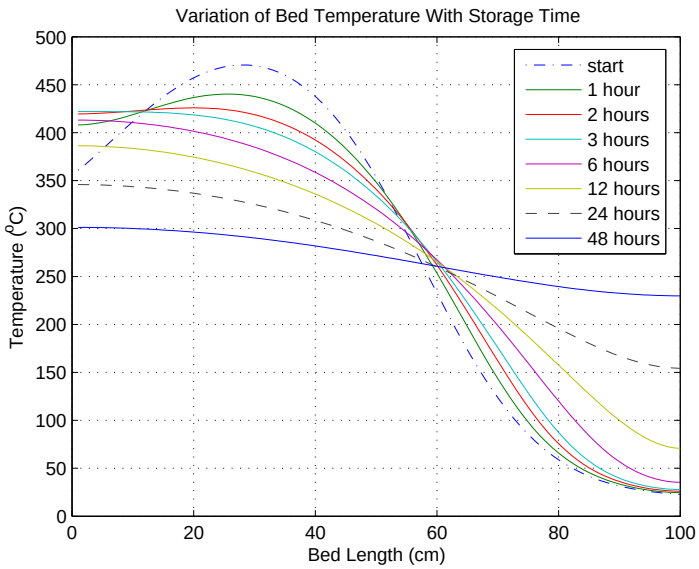

Figure 5.15: This plot shows variation of the temperature profile with storage time for the same rock bed depicted in figure 5.12.

These results reveal that to prevent thermal degradation which can lead to significant reductions in temperature, it is necessary to avoid steep temperature gradients within the bed. Therefore, storage for a home system should have two parts: a hot part for high temperature heat needs (like cooking, boiling, etc) and another part to store heat at lower temperature, probably for water and space heating. These two parts must be separated by an insulation but connected in such a way that air from the receiver enters the hot section first, the exit of which must be the entrance of the warm part. It is desirable to design and size the system in such a way the hot-section will be (approximately) fully charged by the end of the day.

5.9 Chapter Summary and Conclusions

This chapter discusses the simulation of rock bed storage using air for both energy transport and heat transfer. For modelling the bed was discretized into smaller

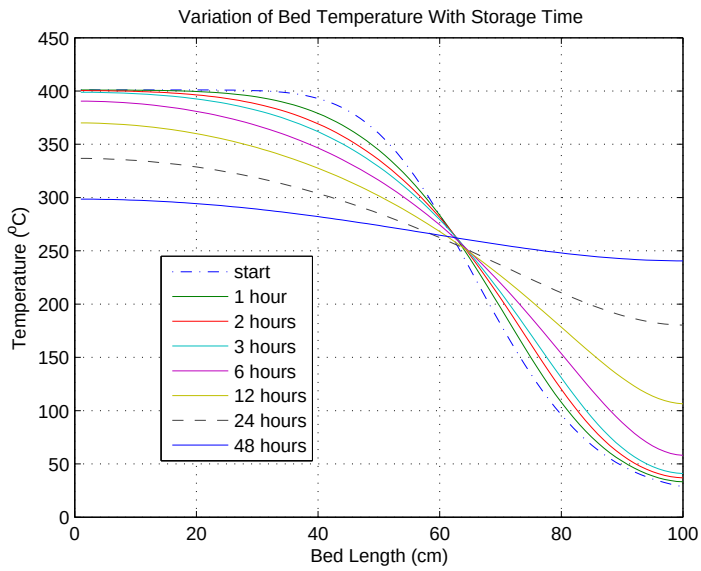

Figure 5.16: This plot shows variation of the temperature profile with storage time for the same rock bed depicted in figure 5.13.

segments assumed to be isothermal. The energy input to the storage was derived from measured and processed data in chapter 2, which essentially simulates the estimated distribution of the monthly average daily beam intensity for a given location in Zimbabwe. The reflectance of the parabolic dish collector, the transmittance of the glazing and efficiency of the receiver were taken into account. The results show that the potential for successful application in Zimbabwe is encouraging.

Two modes of charging the rock bed storage were explored: (i) one in which the mass flow rate is maintained constant and then let variation of the beam intensity as the day progresses, determine inlet air temperature to the storage, (ii) adjusting the mass flow rate such that a constant inlet air temperature is maintained throughout the day.

Simulation reveals that the first option is simple and cheap, but is not ideal for use in days with intermittent cloud cover. While the second option seem to handle such weather without problems, it requires an air pump/fan that can adjust $\dot{m}$ to ensure approximately constant inlet air temperature to the storage. A fan controlled by direct connection to a solar cell could be a good starting point in exploring this option. However, it is perceived that such a device connotates system sophistication and most probably imply significant additional costs. As a first approach in our case, it seems reasonable to adopt the simple option in which $\dot{m}$ is maintained constant.

Thermal insulation plays an important role concerning energy storage. Although an

evacuated insulation system is compact and offers better insulation quality, the rather bulk light density rock wool with Al-foils inserted within is a fairly competent and much cheaper alternative, and therefore ideal to meet the objectives under pursuit in this work. Any insulation whose U-value is to the order of 0.075 $W/m^2 \cdot K$ or better is sufficient to keep the stored thermal energy satisfactorily for almost 3 days. However, apart from insulation quality, temperature gradients within the bed, which inevitably lead to thermal degradation should be avoided wherever possible.

References

[1] Son C.H and Morehouse J.H,' Solid-state phase change materials for solar thermal storage', *Presented at the Twelfth Annual International Solar Energy Conference, ASME,* pp 183-188, 1990.

[2] Grodzka P.G, '*Solar Engineering Energy Technology Handbook*', W. C. Dickinson and P. N. Cheremisinoff', eds., Marcel Dekker, New York (1980).

[3] Stine W.B, Harrigan R.W. 'Solar Energy Fundamentals and Design'. (1985)

[4] Manzo J. P, 'Applications of solar energy storage systems', *Specifying Engineer*, vol.41, No.4, pp 106-111, 1979.

[5] Bolton J. R and Archer M. D, 'Chemical conversion and storage of solar energy - an overview', *Intersol 85: Proceedings of the Ninth Biennial Congress of the International Solar Energy Society*, pp 1843-1859, 1986.

[6] Fujii I, Tsuchiya K, and Ishino M, 'Solar heat storage by use of thermochemical reversible reactions', 1992 *ASME-JSES-KSES International Solar Energy Conference* Part 1 (of 2), pp 71-76, 1992.

[7] Edwards J. H, Do K. T, and Ashit M, 'CSIRO/pacific power R&D project on using CO_2/CH_4 reforming for solar energy storage and transmission', *Proceedings of the 1995 ASME/JSME/JSES International Solar Energy Conference,* Part 1 (of 2), pp 389-398, 1995.

[8] Imhof A, 'Cyclone reactor - An atmospheric open solar reactor', Solar Energy Materials,*Proceedings of the 5th Symposium on Solar High-Temperature Technologies*, vol.24, No.1-4, pp 733-741, 1991.

[9] Williams O. M and Carden P. O, 'Ammonia Dissociation For Solar Thermochemical Absorbers', *International Journal of Energy Research*, vol.3, No.2, pp 129-142, 1979.

[10] Steiner D, Wierse M, and Groll M, 'Development and investigation of thermal energy storage systems for the medium temperature range', *Proceedings of the*

1995 30th Intersociety Energy Conversion Engineering Conference-IECEC, pp 193-198, vol.2, 1995.

[11] Kolb G. J, Diver R. B and Siegel N, 'Central-station solar hydrogen power plant', Int Sol Energ Conf , *Solar Engineering 2005 - Proceedings of the 2005 International Solar Energy Conference*, pp 645-650, 2006.

[12] Goswami D.Y, Kreith F and Kreider J.F (1999) 'Principles of Solar Engineering'. 2*nd Edition*.

[13] Dincer I, 'Evaluation and selection of energy storage systems for solar thermal applications',*International Journal of Energy Research*, vol.23, No.12, pp 1017-1028, 1999.

[14] Tamme R, Steinmann Wolf-Dieter and Laing D, 'Thermal energy storage technology for industrial process heat applications', *Proceedings of the 2005 International Solar Energy Conference*, pp 417-422, 2006.

[15] Dincer I, Dost S and Li X, 'Thermal energy storage applications from an energy saving perspective', *International Journal of Global Energy Issues*, vol.9, No.4-6, pp 351-364, 1997.

[16] Sharma V. K, Rizzi G and Garg H. P, 'Design and development of an augmented integrated solar collector with rock storage system for heating applications', *Energy Conversion and Management*, vol.31, No.4, pp 369-377, 1991.

[17] Boulet P, et al., 'Combined Radiation and Conduction in Fibrous Insulants (from 24°C up to 400°C)', *23rd International Thermal Conductivity Conference*, 1995.

[18] de Dianous P, Pincemin F, Boulet P and Jeandel G, 'Modelling and Experimental Evaluation of Thermal Insulation Properties of Mineral Wool Products at High Temperature'. Thermal Insulation Materials: Testing and Applications, 3rd Vol, *ASTM STP* 1320, 1997.

[19] Lin E.I, Stultz J.W and Reeve R.T. 'Effective Emittance for Cassini Multilayer Insulation Blankets and Heat Loss Near Seams', *Journal of Thermophys. Heat Transfer*, Vol 10, No.2, pp 357 - 363, 1996.

[20] Siegel R and Howell J R, 'Thermal Radiation Heat Transfer', 4*th Edition*, pg 423.

[21] Hessari F. A, Parsa S, and Khashechi A. K,'Behavior of packed bed thermal storage', *International Journal of Engineering, Transactions A: Basics,* vol.17, No.2, pp 181-192, 2004.

[22] Meier A, Winkler C and Wuillemin D, 'Experiment for Modelling High-temperature Rock-bed Storage ', *Solar Energy Materials*, 24 (1-4), pp 255-264, Dec 1991.

[23] Clark J. A. and Beasley D. E, 'Dynamic response of packed bed thermal storage unit', *Prog. Solar Energy,* pp 525-530, International Solar Energy Society, 1982.

[24] Saez A. E and McCoy B. J, 'Dynamic response of a packed bed thermal storage system-A model for solar air heating', *Solar Energy* 29, No.3, 1982.

[25] Schumann T. E. W, 'Heat Transfer: A Liquid Flowing Through a Porous Prism', *J. Franklin Inst.*, **208**, 405 (1929).

[26] Hughes P.J, Klein S. A and Close D. J, 'Packed Bed Thermal Energy Storage Models For Solar air Heating and Cooling Systems', *Trans. ASME, J. Heat Transfer*, **98**, 336, 1976.

[27] Hughes P. J, 'The Development and Predicted Performance of Arlington House', *MSc. Thesis in Mechanical Eng.* - University of Wisconsin - Madison, 1975.

[28] Duffie J.A and Beckman W.A. 'Solar Engineering Of Thermal Processes', pg-382, 1991.

[29] Jeffreson C.P, 'Predictions of Breakthrough Curves in Packed Beds', *Journal of American Institute of Engineers*, **18**(2), 409 (1972).

[30] McAdams W.H, 'Heat Transmission', *3rd Edition*, 1954.

[31] Incropera F.P. and DeWitt D.P., 'Fundamentals of Heat and Mass Transfer', *5th Edition*, 2002.

[32] Chandra P and Willits D. H, 'Pressure drop and heat transfer characteristics of air-rock bed thermal storage system', *Solar Energy* 27, No.6, 1981.

[33] A.J Slavin, V. Arcas, C.A Greenhalgh, E.R Irvin and D.B Marshall, 'Theoretical model for the thermal conductivity of a packed bed of solid spheroids in the presence of a static gas, with no gdjustable parameters except at low pressure and temperature'. International Journal Of Heat and Mass Transfer, Vol. 45, pp 4151-4161, March 2002.

[34] Jianhua Zhou, Aibing Yu and Yuwen Zhang, 'A boundary Element Method for Evaluation of the Effective Thermal Conductivity of Packed Beds'. Journal Of Heat Transfer, Vol. 129, March 2007.

Additional literature not directly quoted

[35] Du J, Chow L. C and Leland Q, 'Optimization of high heat flux thermal energy storage with phase change materials', *ASME*, vol.376 HTD, No.2, Proceedings of the ASME Heat Transfer, pp 49-54, 2005.

[36] Setterwall F, 'Phase-Change Materials and Chemical Reactions for Thermal Energy Storage', *ASHRAE Winter Meetings CD Techn. Symp. Papers*,Amer. Soc. Heating, Ref. Air-Conditioning Eng. Inc., Atlanta, GA 30329, United States, pp 627-629, 2003

[37] Salyer I. O and Sircar A. K, 'Review of phase change materials research for thermal energy storage in heating and cooling applications at the University of Dayton from 1982 to 1996', *International Journal of Global Energy Issues*, vol.9, No.3, pp 183-198, 1997.

[38] Radosovich, l. G., and Wyman C. E (1983), 'Thermal Energy Storage Development for Solar Electrical Power and Process Heat Applications', *Transactions of the ASME, Journal of Solar Energy Engineering* 105, 111 .

[39] Shewen E. C, Sullivan H. F, Hollands K. G. T and Balakrishnan A. R, 'A Heat Storage System for Solar Energy', *Report STOR-6, Waterloo Research Institute*, Univ. of Waterloo, Aug 1978.

[40] Dunkle R. V and Ellul W. H. J, 'Randomly Packed Particulate Beds Regenerators and Evaporative Coolers', Trans. of the Inst. of Enginners - Australia, MC8, 117, 1972.

[41] Kuhn J.K, Von Fuchs G. F, Warren A. W and Zob A.P, 'Developing and Upgrading of Solar System Thermal Energy Simulation Models', *Report of Boeing Computer Services Company, to the U.S Dept. of Energy*, 1980.

[42] Mumma W. D and Marvin W. C, 'A Method of Simulating The Performance of a Pebble Bed Thermal Energy Storage and recovery System', *ASME paper* 76-Ht-73, 1979.

[43] Munson B.R, Young D.F and Okiishi T.H, 'Fundamentals of Fluid Mechanics'. 4th edition, 1999.

Chapter 6

Basic Applications

6.1 Introduction

The ultimate objective of the present research is to develop small multi-purpose solar concentrating systems for use in developing countries that lie within the Sunbelt. However, as a first approach, it is appropriate to develop a system whose energy output suffices to at least meet the rural-folks' most basic heat energy need: food preparation by boiling in water and pan frying. To date, most of the cooking is done using the speedily-diminishing biomass fuel. In this chapter, the last component (and perhaps the most important in regards to cooking) of our concentrating system is presented. It is in the form of hotplates that have pin-fins on one side, and are powered by convection heat transfer using hot air circulated through a charged heat storage unit as described in the previous chapter.

6.2 The Hotplates

6.2.1 Energy Extraction from a Charged Rock Bed

With high-temperature-heat now stored in the packed bed as discussed in the previous chapter, the next stage involves extracting and using this heat for cooking. The bed will be discharged either to some extent or completely during food preparation. In this case, air is again used to remove energy from the charged bed. The hot air is then transported via insulated pipes to provide power to a specially designed hotplate.

In essence, the hot air is circulated from the bed in the reverse direction (i.e opposite direction to flow during the charging mode), and then goes directly to the finned convection side of the hotplate where it cedes most of its sensible heat energy (see

the illustration in figure 6.1). It is then blown back to the bottom of the storage where it starts heating-up as circulation continues, by means of an air pump (or fan) at an appropriate mass flow rate.

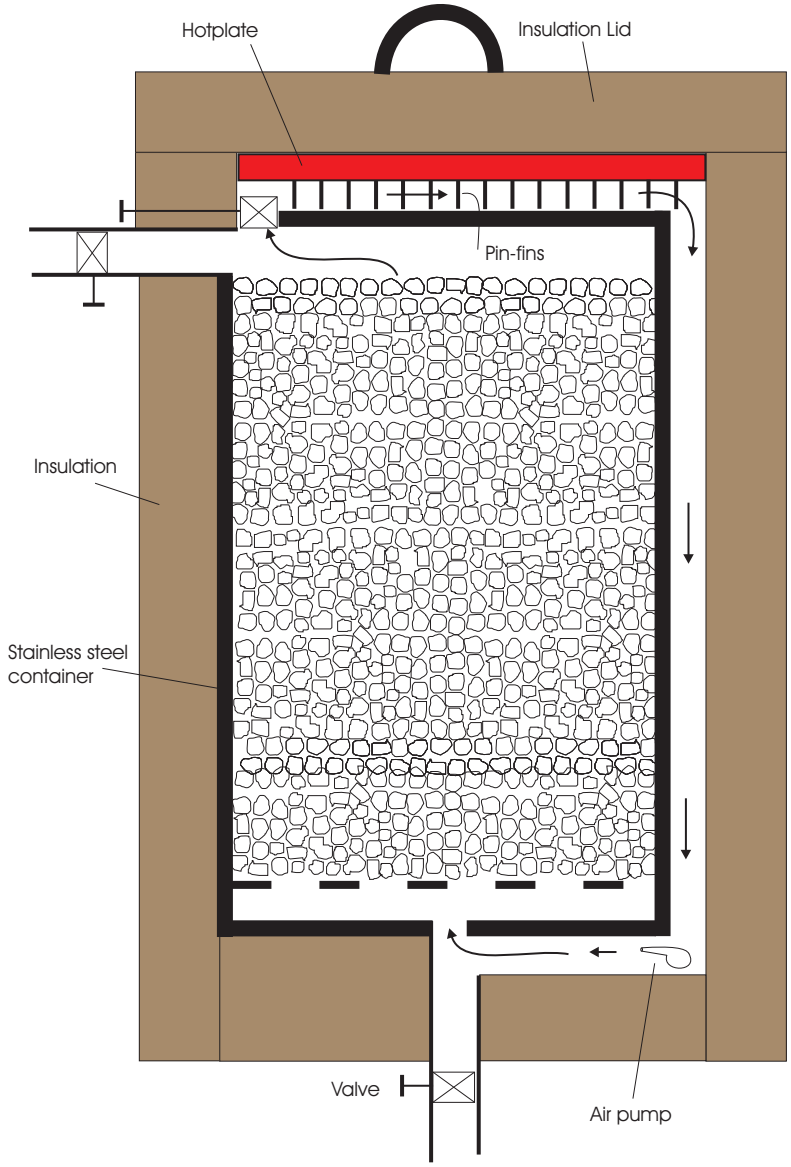

Figure 6.1: A schematic showing the cross-sectional view of the hotplate set-up and the air circuit (indicated by the arrows) that supplies heat flux for cooking and boiling.

For modelling and prediction of the transient behavior of the packed bed during discharge, the same governing equations and computational programme used for the charging process can be adapted. The only major adjustments that need attention is to note that air direction is now reversed and that the inlet air is cold or presumably lower than the bed temperature.

6.2.2 The Finned Side of the Hotplate

Since air is used for energy transport, it is imperative that cession of heat to the hotplate is by convection. Consequently, in order to enhance heat extraction from the hot air, the use of extended surfaces in the form of circular pin-fins[1] is the favoured choice. The thermal conductivity of the pin material is of fundamental importance in regards to the temperature distribution along the pin, which in turn strongly influences the degree to which heat transfer is enhanced.

In principle, the pin material should have a large thermal conductivity so as to substantially minimize temperature variations from the base to its tip. For the ideal case of infinity thermal conductivity, the entire pin would be at the temperature of the base and as such provides the maximum possible heat transfer enhancement. For practical situations, the appropriate use of copper and or aluminium usually provides an effective solution. However, although copper has a much superior thermal conductivity, aluminium is usually preferred and popularly employed in industry because of additional considerations related to lower costs and light weight.

In order to model the heat transfer to the hotplate, circular pins of uniform cross-sectional area with an adiabatic[2] pin tip are considered. Equations that characterize this type of pins are readily available in heat transfer texts, and those relevant to this study are now adopted for application. Defining the base temperature as T_{base}, the perimeter as P_{pin}, its length and cross-sectional area as L_{pin} and A_c respectively, the temperature distribution along the pin is given by:

$$T(x) = T_{air} + (T_{base} - T_{air})\frac{\cosh[\varpi(L_{pin} - x)]}{\cosh(\varpi L_{pin})} \tag{6.1}$$

where $\varpi = \sqrt{hP_{pin}/(kA_c)}$. In this case, we are basically interested in the amount heat transfered from the entire pin, i.e the pin heat transfer rate q_{pin}. This is given by

$$q_{pin} = \sqrt{hP_{pin}kA_c}\ (T_{air} - T_{base})\ \tanh(\varpi L_{pin}) \tag{6.2}$$

6.2.3 Pin-fin Performance

The performance of the pins is measured based on two concepts: effectiveness (ε_{pin}) and or efficiency (η_{pin}). Pin effectiveness is defined as the ratio of the pin heat

[1] For convenience in this work, we will simply call the pin-fins: pins.

[2] An adiabatic pin tip implies that: $\frac{d\theta}{dx}|_{x=L} = 0$, where $\theta = T_{air} - T_{base}$, known as the excess temperature

transfer rate to the heat transfer rate that would occur without the pin. For the setting and type of pins under discussion, it can be calculated as

$$\varepsilon_{pin} = \frac{q_{pin}}{hA_c(T_{air} - T_{base})} \tag{6.3}$$

Equations (6.2) and (6.3) suggest that, small convection coefficients (typical of air) and thin pins (i.e small A_c) boost pin effectiveness. On the other hand, the installation of pins obviously alters the surface convection coefficient. However, this effect is commonly ignored in heat transfer texts, and the usual practice is to assume that the convection coefficient of the finned surface is equivalent to that of the unfinned surface [1, 2].

In any rational design, the numerical value of ε_{pin} should be as large as possible. Literature [2] recommends that the use of pins can hardly be justified unless $\varepsilon_{pin} \geq 2$. If for some reason, the pin fails to pass this limit, ε_{pin} can be boosted by increasing L_{pin} and or making it thinner if possible. However, the use of very long pins is not necessary in order to achieve near maximum heat transfer enhancement. In case of pins with a uniform cross-sectional area and characterized by an adiabatic tip, 98% of the maximum possible heat transfer rate is achievable for $\varpi L_{pin} = 2.3$, i.e lengthening the pins is hardly justifiable beyond $L_{pin} = \varpi/2.3$.

As mentioned earlier, pin thermal performance can also be expressed in terms of pin efficiency. It is defined as the ratio of the pin heat transfer rate to the maximum heat transfer rate that would exist if the entire pin surface were at base temperature.

$$\eta_{pin} = \frac{q_{pin}}{hA_{pin}(T_{air} - T_{base})} \tag{6.4}$$

where A_{pin} is the surface area of the pin. Nevertheless, this an idealized definition since any pin has a finite conduction resistance at the base. Therefore, a temperature gradient along the pin will always exist. The overall pin efficiency η_o, characterizes a bank of pins and the base surface to which the pins are attached. It can be shown that

$$\eta_o = 1 - \frac{NA_{pin}}{A_t}(1 - \eta_{pin}) \tag{6.5}$$

where $A_t = NA_{pin} + A_b$, N and A_b are the number of pins in the array and the prime surface (unfinned portion of the base) respectively.

6.2.4 Arrangement of Pins

In heat transfer engineering, the arrangement of pins in the direction of the fluid velocity is commonly done in one of the two ways: *staggered* or *aligned* configuration. From the standpoint of engineering design, and in view of the low relatively small Reynolds numbers ($Re_D < 100$) involved in this study, the staggered geometrical arrangement is more appropriate. The geometry followed for finning the convection side of the hotplate under discussion is illustrated in figure 6.2

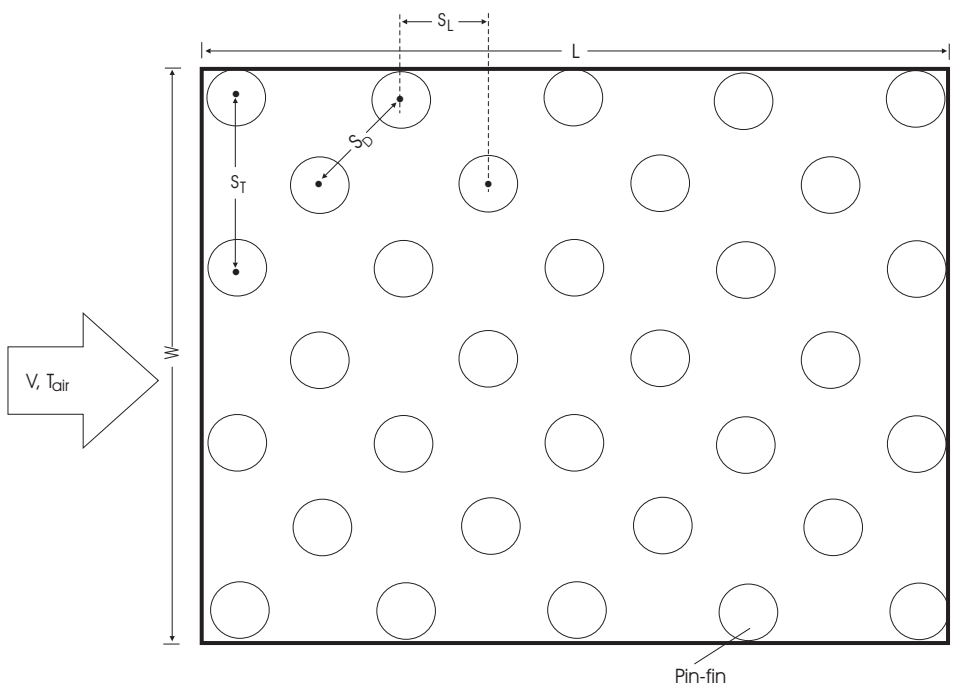

Figure 6.2: A schematic showing pins arranged in a staggered configuration.

The staggered bank of pins is characterized by pin diameter, the transverse pitch S_T and the longitudinal pitch S_L. For large Reynolds numbers, flow conditions are influenced by boundary layer separation effects and wake interactions. As such, the convection transfer coefficient associated with a pin is a function of position in the bank. The (convection) coefficient for pins in the first row can be approximated to that of a single pin in cross flow, while that of pins in the inner rows is usually higher. However in most cases (for the staggered arrangement), heat transfer conditions stabilize, such that no substantial change occurs in the convection coefficient for pins beyond the 4th row.

In our case, where flow is characterized by low velocity and small Reynolds numbers, the correlation by Churchill and Bernstein [3] was found to be appropriate. It covers the range of interest for us regarding both the Re and Pr, i.e it's valid for all the

Re for which data is available and for $Pr > 0.2$. When adapted for application to determine the average convection coefficient in this study, the equation has the form

$$\bar{h} = \frac{k_{air}}{D_{pin}}\left[0.3 + \frac{0.62\ Re_{max}^{1/2}\ Pr^{1/3}}{\{1+(0.4/Pr)^{2/3}\}}\left\{1+\left(\frac{Re_{max}}{282\ 000}\right)^{5/8}\right\}\right]^{4/5} \tag{6.6}$$

where all properties are evaluated at film temperature, and is said to allow an error margin to the order of ±20%.

The computation of the Reynolds number for similar problems in heat transfer is usually based on the maximum fluid velocity occurring within the bank of pins. With reference to the spacing and arrangement shown in figure 6.2, calculation of the maximum fluid velocity is subjective to the condition that: if $2(S_D - D_{pin}) < (S_T - D_{pin})$, then

$$V_{max} = \frac{S_T}{2(S_D - D_{pin})}\ V \tag{6.7}$$

otherwise

$$V_{max} = \frac{S_T}{2(S_T - D_{pin})}\ V \tag{6.8}$$

leading to $Re_{max} = V_{max}D_{pin}/\nu$ in our case.

6.2.5 Pressure Drop

For successful operation, the pressure drop associated with flow across the bank is of fundamental interest. It is directly proportional to the power required to move the fluid across the bank of pins. The need to comprehend the feasibility of such an undertaking, in terms of the operational costs, is therefore an essentiality from an economic perspective.

The nature of the problem at hand is such that the air experiences a substantial temperature change as it traverses the bank. Therefore, air density inevitably comes into play. With this in mind, an adaptation of the correlation proposed by Zhukauskas [5] was considered appropriate for estimating pressure drop. Applied to our case, the correlation can be expressed as

$$\Delta p = N_L\ \chi\left(\frac{\rho_{air}V_{max}^2}{2}\right)F \tag{6.9}$$

where N_L is the number of pin rows that are perpendicular to the direction of flow.

Since the original equation was developed for a staggered arrangement is the form of an equilateral triangle (i.e $S_T = S_D$ in figure 6.2), a correction factor χ that enables extension of the results to accommodate different spacing has been included. It can be estimated from figure 6.3.

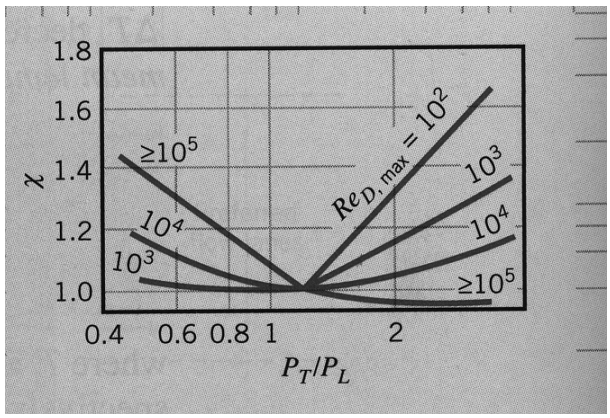

Figure 6.3: Estimation of the correction factor χ for evaluating the pressure drop across a staggered bank configuration as defined by equation (6.9). With reference to figure 6.2, $P_T = S_T/D_{pin}$ and $P_L = S_L/D_{pin}$. Adapted from [2].

For internal flow through a finned zone within a channel, a correlation developed by Koşar et al., [6] is suitable for the estimation of the friction factor F. It is basically a hybrid approach that takes into account the contribution of the aspect ratio of the pin and channel dimensions. In other words, it takes into account the fact that neither the hydraulic Reynolds number associated with pin diameter, nor that associated with channel dimensions, can single-handedly fully capture the physical parameters that govern friction factors influencing fluid flow in a finned channel. Adapting it for application in our case, the correlation has the following form:

$$F = \frac{C_1}{Re_{max}^{\kappa_1}} \left(\frac{L_{pin}/D_{pin}}{L_{pin}/D_{pin}+1} \right)^{\kappa_2} \left(\frac{S_T\ S_L}{A_{ch}} \right)^{\kappa_3} + \frac{C_2}{Re_{ch}^{\kappa_5}} \left(\frac{1}{L_{pin}/D_{pin}+1} \right)^{\kappa_4} \left(\frac{S_T\ S_L}{A_{ch}} \right)^{\kappa_3} \tag{6.10}$$

where Re_{ch} is the Reynolds number based on the hydraulic diameter[3] of the channel of cross-sectional area A_{ch}. Koşar et al. report that the margin of error for this correlation is to the order of 7.5% when applied for a staggered configuration.

The values of the other constants are now summarized:

[3]The hydraulic diameter for a channel is estimated by $D_h = \frac{4A_{ch}}{P}$, with P as the channel perimeter.

$C_1 = 1739$
$C_2 = 345$
$\kappa_1 = 1.7$
$\kappa_2 = 1.1$
$\kappa_3 = -0.3$
$\kappa_4 = 2.0$
$\kappa_5 = 1.0$

It is important to mention that, these constant are valid only for circular pins in a staggered arrangement.

6.3 Cookery

For a typical Zimbabwean rural homestead, cooking is largely boiling the food stuff in water and to a lesser extent, pan frying once in a while due to limited resources. Common foods range from vegetables, legumes, maize-meal, ground nuts, eggs, pumpkins, sweet potatoes, and to a lesser extent meat, fish, etc. The staple diet is maize-meal, which does not take that long to cook. The preparation of a moderate daily meal may last for 1 to 1.5 hours depending on the desired outcome for an average family of six members. The scope of the present discussion on boiling is therefore limited to its relevance towards this kind of cooking.

6.3.1 Pertinent Boiling Regimes

Understanding the fundamentals that characterize the different regimes of pool boiling, especially for water, is therefore imperative. Figure 7.6 in appendix B.2 shows a typical boiling curve for water at 1 atm. In the context of the type of cooking anticipated, it is evident from this plot that only *free convection* and *nucleate* boiling regimes are of interest to this study.

Free convection boiling takes place if the excess temperature[4] ΔT_e is about 5 ^{o}C or slightly less. In simpler terms, the inner surface of the container or pot in which the water is being heated should be about 105 ^{o}C at 1 atm. The heat flux necessary to maintain this mode of boiling is to the order of 10^3 W/m^2. This is equivalent to powering a modern electric hotplate of diameter 22 cm, usually the biggest plate on an ordinary cooker, with anything between 100 to 300 W. For the smaller plates, even less power is needed to maintain the same flux. Cooking techniques such as

[4]The excess temperature in this context is defined $\Delta T_e = T_s - T_{sat}$

simmering and poaching[5] fall in this category.

To meet the conditions that prompt nucleate boiling (slightly above the *Onset of Nucleate Boiling*), the heat flux should be maintained above 10^4 W/m^2 such that the excess temperature is within $5 \leq \Delta T_e \leq 30$ ^{o}C. However, for boiling in cookery, it is not necessary to come anywhere near point B (figure 7.6 in appendix B.2) at which boiling is typically characterized by jets or columns of vapour. Heat fluxes that can maintain excess temperatures just above 5 ^{o}C should be enough. In other words, the inner surface of pot with boiling water be anywhere between 106 - 110 ^{o}C. On a 22 cm diameter electric hotplate mentioned earlier, wattage to the order of 450 W would suffice to sustain nucleate boiling.

6.3.2 Frying

Deep Frying

This is a common method used in the preparation of foods. It may be defined as the process of immersing a food product in an edible oil or fat that is heated to a temperature above the boiling point of water. In principle, heat is transferred from the oil or fat to the food, and resultantly water evaporates from the latter. Therefore, frying is essentially a coupled heat and mass transfer problem.

It is common practice in food science to break the frying process into four stages: (i) initial heating, (ii) surface boiling, (iii) falling rate, and (iv) bubble end point [9]. Initial heating is described as the initial immersion of raw food into hot oil and is characterized by the absence of water vaporization. During this stage, heat is transferred from the oil to the food via free convection and through the food via conduction.

Stage two, surface boiling, is characterized by the sudden loss of free moisture at the crust formation. And thirdly, the falling rate stage parallels that of drying in which there is continued thickening of the crust region, decreased heat transfer, and a steady decrease in vapor mass transfer from the material. Lastly, the bubble end point is characterized by the apparent cessation of moisture loss from the food during frying.

Frying is in general, a unit process although it happens in stages. Heat transfer rates play a critical role in browning the crust and retaining characteristic properties of the fried product. Therefore, a sustained supply of heat flux during the frying process

[5]These are cooking methods in which foods are cooked in hot water kept at or just barely below the boiling point, to the order 95 ^{o}C.

is important in sustaining the desired frying temperature. Most foods fry properly between 149 - 191 ^oC [10], and preferably closer to the lower limit as temperature above the upper limit produce browning before the inside is completely cooked. Care must be taken with used oil as it might start smoking even at much lower temperatures depending on its quality.

Pan Frying
This is a form of frying characterized by the use of less cooking oil than deep frying; enough oil to, at most, cover the food to be cooked only half way. As a form of frying, pan frying principally depends on oil as the heat transfer medium and on correct temperature to retain the moisture in the food. The exposed top-side allows, unlike deep frying, moisture loss while contact with the bottom of the pan creates greater browning on the contact surface. Because of the partial coverage, the food must be flipped at least once to cook both sides.

The advantages of using less oil are practical: less oil is needed on hand and time spent heating the oil is much shorter. The major disadvantage of using less oil is that it is more difficult to keep the oil at an even temperature. A frying pan with a thick base, performs better than a pan with a thinner bottom since the massive base will improve temperature regulation. Based on the type of food usually available and affordable by the rural folks in Zimbabwe, pan frying is practically sufficient to satisfy the basic frying needs.

6.4 Results and Discussion

6.4.1 Determination of Hotplate Dimensions

A computer programme that simulates the simultaneous processes of discharging the bed and powering the hotplate was developed using MATLAB routines. As already mentioned in earlier sections, air is used for both heat transport and transfer (by convection). A typical air circulation circuit is shown in figure 6.1 by means of arrows.

Figure 6.4 serves to illustrate the cross-sectional view of the air channel on the finned side of the hotplate. In our simulations, the hotplate is regarded as a 10 mm thick rectangular plate made from copper. The underside is finned as shown on the diagram in question. The hotplate top surface is adapted to the conventional circular shape in order to reduce radiative heat loss by insulating the areas likely to remain exposed during operation time. An illustration of the bird's eye view is also shown.

The portion of the hotplate where the pot sits acts as a heat sink during cooking. As such, heat is expected to flow by conduction, from the insulated corners towards this

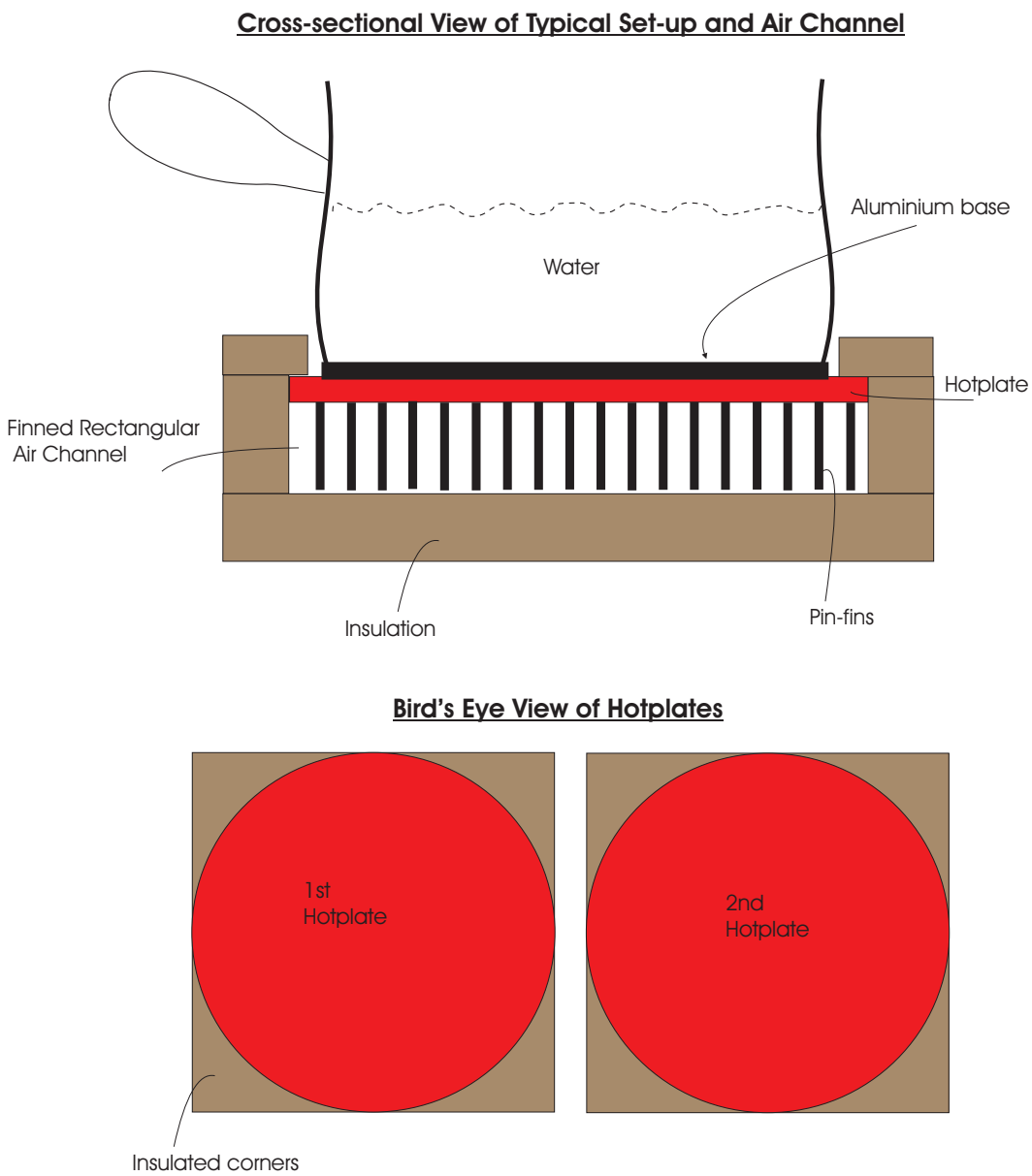

Figure 6.4: A schematic showing a typical cross-sectional view of the finned rectangular air channel and cooking set-up. The bird's eye view of the hotplates is also shown.

heat sink when operation reaches steady state. Copper has high thermal conductivity, this inherent quality will enable effective heat flow from the insulated sections towards the heat sink, and will thus prevent the insulated portions from overheating.

To facilitate comprehensive analysis in the model, the main rectangular plate has been considered in two modes: (i) as a single unit in which the circular hotplate shown in figure 6.4 are only superficially separated by the top insulation, but otherwise belong to the same underlying rectangular base plate, (ii) as two in tandem (in regards to direction of air flow) but separate hotplates, i.e without thermal interaction by conduction between them. For reference, the hot air is understood to reach the underside of the plate labelled '1st hotplate' before passing to that of the '2nd hotplate'.

The first challenge is to determine the appropriate pin dimensions that would yield to the desired heat transfer rates. Experimenting with the programme showed that mass flow rates to the order of 0.005 kg/s are ideal for the conditions an dimensions under discussion. Much higher values imply more fan power requirements while values that are too low yield to inadequate power supply. Using a mass flow rate of 0.005 kg/s, the pin height was then varied and the results are summarized in figures 6.5 and 6.6.

The criteria to determine pin height was based on finding the height that yields to maximal power delivery preferably to both plates. As can be seen on the heat-rate and -flux plots in figure 6.5, power delivery in general, increases with increasing pin height for the first plate while it has a maximum at some point for mass flow rates below 0.007 kg/s. Simulation showed that above this limit, the behavioral pattern of the power delivered to the second plate start approximating that of its counterpart for the first plate. For the conditions under discussion, maximum heat flux delivery to second plate occurs at a pin height of about 7 cm.

The pin diameter adopted for use in this work is 5 mm due to the availability of copper wires of this diameter in the commercial market. Nevertheless, it can be deduced from the results displayed in figure 6.6 that further heat transfer enhancement can be achieved by thin pins (also confirmed by Incropera [2]). By mere intuition, closely packed thin pins are preferable with the proviso that the pin gap is not too small to impede flow between pins, as this will inevitably lead to a reduction of the convection coefficient and an increase in pressure drop, see equation (6.9). The dimensions used for modelling the hotplates are summarized in table 6.1.

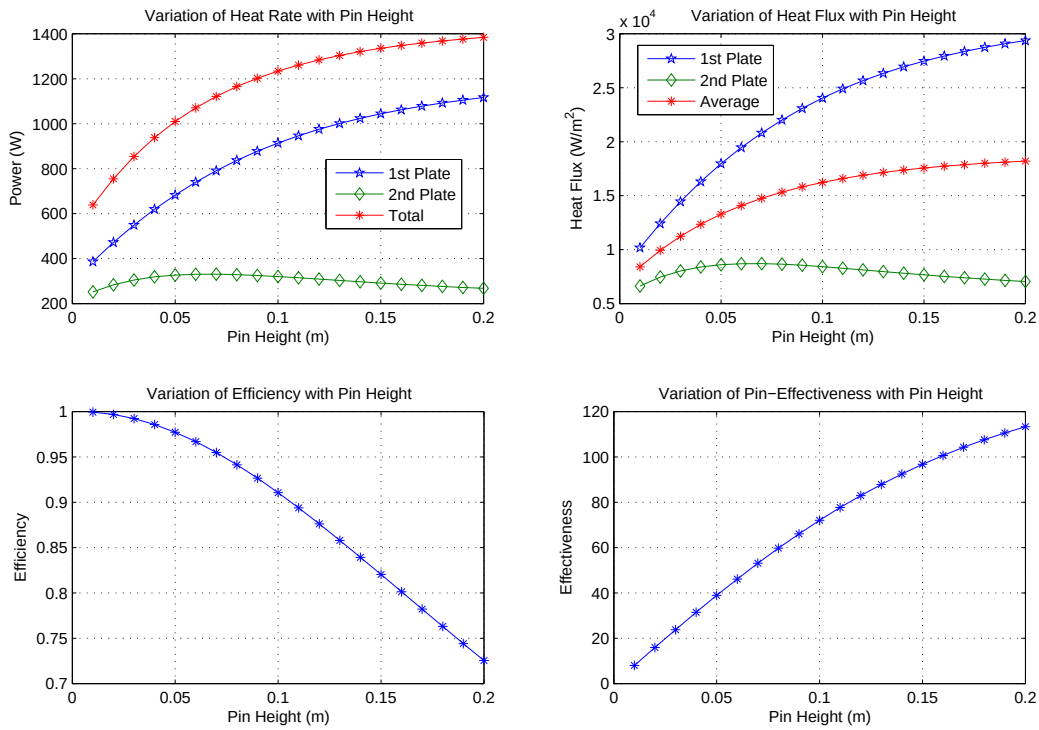

Figure 6.5: Plots summarizing the results of increasing pin height. In this case, pin diameter was assumed to be 5 mm and the mass flow rate fixed at 0.005 kg/s.

INPUT PARAMETERS FOR MODELLING THE HOTPLATE

PARAMETER	VALUE	UNIT
Hotplate		
Length	0.5	m
Width	0.25	m
Pin Dimensions		
Diameter	0.005	m
Height	0.07	m
S_T	0.03	m
S_L	0.017	m

Table 6.1: This table summarizes the parameters used to model the hotplates as explained in the text. The effective radius of the heat sink has been assumed to be 0.22 cm, just as big as a fairly large plate on an ordinary electric stove. S_L and S_T are defined in figure 6.2.

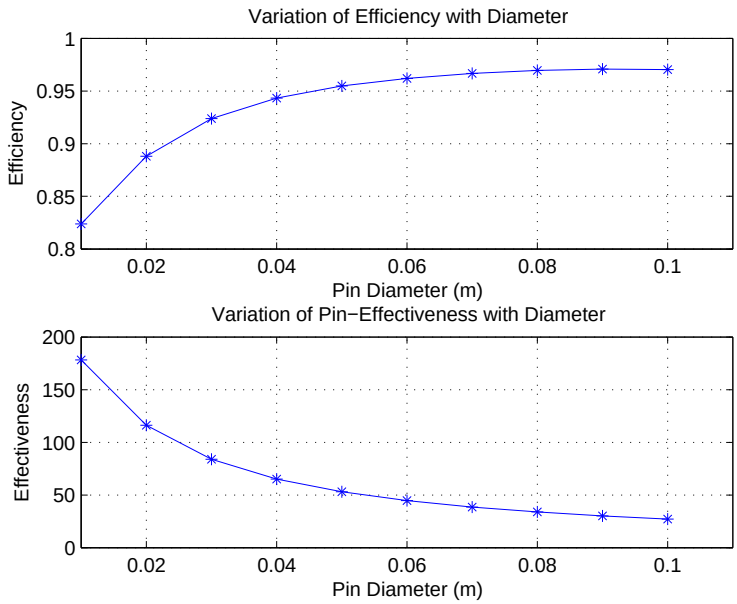

Figure 6.6: Plots summarizing the results of increasing pin Diameter. The pin height was taken to be 7 cm, derived from the results obtained in figure 6.5 while $\dot{m} = 0.005$ kg/s.

6.4.2 Determination of Mass Flow Rate

In our case, at stake is a typical engineering problem where $\dot{m}$ is of fundamental interest, because its value determines the heat rate that can power our hotplate. It is also linked to the economic aspect because its value is proportional to resultant air velocity, and therefore strongly influences the blow power that is needed to overcome pressure drop in the system.

The variation of heat flux and heat rate with $\dot{m}$ is shown in figures 6.7 and 6.8. The general trend is an exponential increase as mass flow rate increases. At low $\dot{m}$ (and therefore low air velocities), most of the heat energy is taken by the first plate, see figure 6.9 which depicts an exponential decrease of air temperature at low velocities, and resultantly, most of the energy is absorbed by the first plate. However, as $\dot{m}$ is increased, the decrease in air temperature approaches linearity, allowing more energy now to spill over to the second plate.

Nonetheless, these results suggest that there is very little, if any, to gain with using high mass flow while very low air velocities may confine cession of all the useful heat to first plate. With appropriate adjustment of mass flow rate, the advantage of using two plates in tandem is obvious in that different food stuffs may require different cooking temperatures.

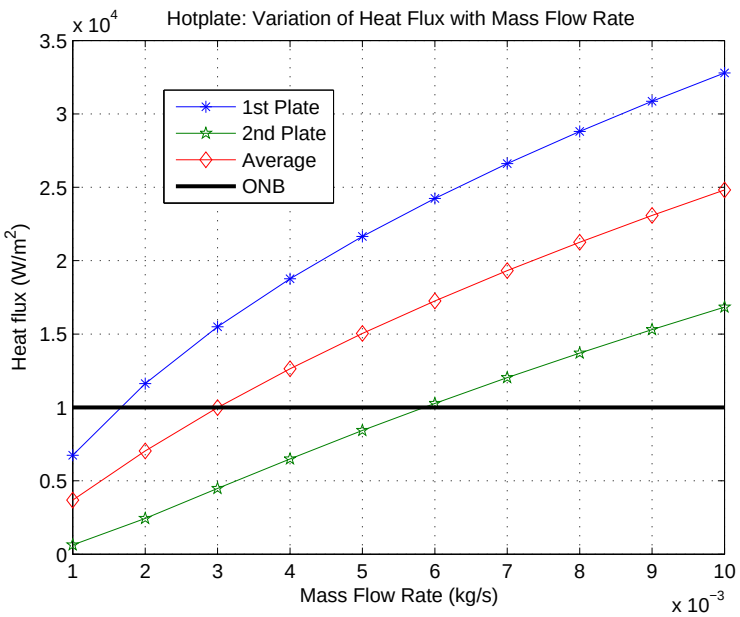

Figure 6.7: Plots showing the variation of heat flux with mass flow rate, see table 6.1 for dimensions and parameters defining the hotplate. The inlet air temperature from the storage is assumed to be 400 ^{o}C.

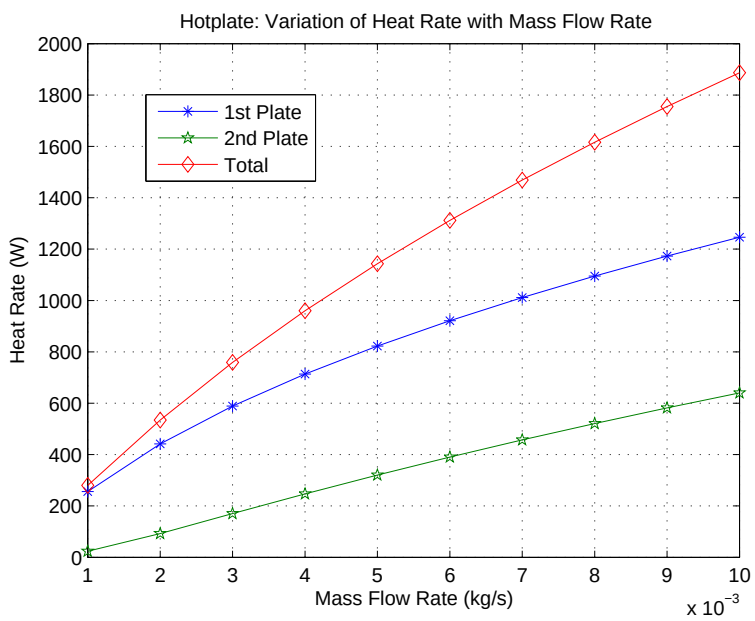

Figure 6.8: Plots showing the variation of heat rate with mass flow, see table 6.1 for details. The inlet air temperature from the storage is assumed to be 400 ^{o}C.

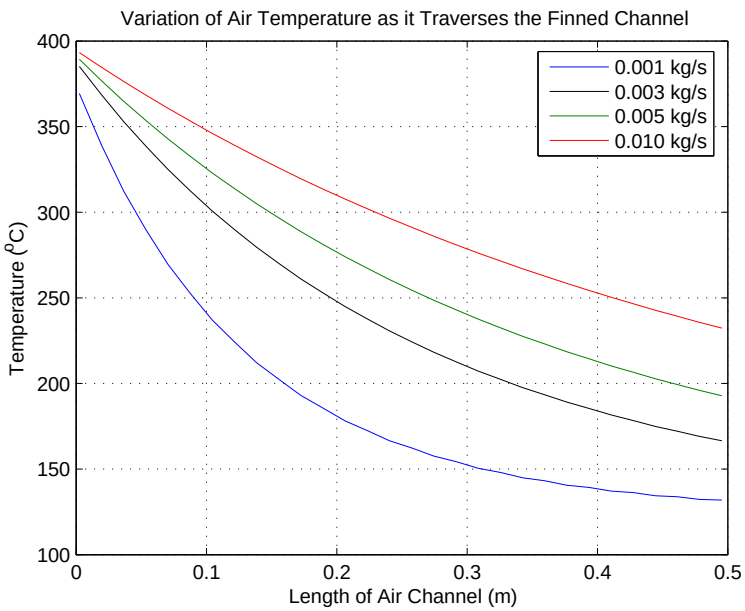

Figure 6.9: Plots showing the variation of air temperature across the channel at different mass flow rates see table 6.1 for details. The inlet air temperature from the storage is assumed to be 400 ^{o}C.

This scenario calls for a compromise between the length of the underlying rectangular plate and adjustment of the mass flow rate to a level that would achieve the desired heat fluxes in both plates, should there be need to use two. In the context of aiming to achieve the desired type of boiling in cookery, the heat flux curves in figure 6.7 provide the necessary guidance.

As discussed earlier, the heat flux supplied should be within vicinity of the ONB. With the inlet hot air 400 ^{o}C, it can be seen that, mass flow rates to the order of 0.003 kg/s is more than sufficient to offset nucleate boiling on the first hotplate. The limit can be revised upwards to 0.004 and 0.007 kg/s for the average and second plate respectively.

However, for a typical Zimbabwean family located in a rural community, it's usually not necessary to have two hotplates in the nucleate boiling mode. Just one plate of the size discussed here suffices in a normal setting. The main staple diet which consists of maize meal, needs on average 1 to 1.5 hours of nucleate boiling, for a meal that can feed a family of about 6 members. A mixture of green vegetables, which are usually part of the meal need less heating and cooking/frying time, and can thus be prepared on the 'not-so-hot' second plate.

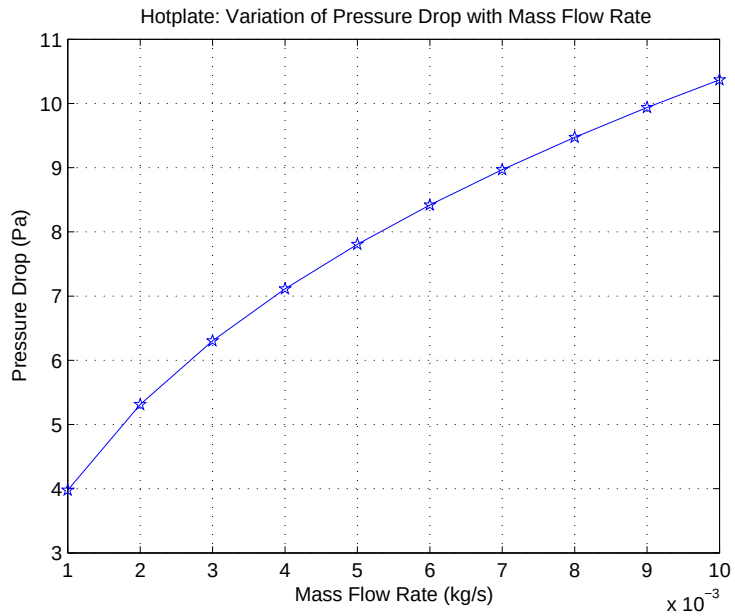

Figure 6.10: This plot shows how the pressure drop across the bank of pins varies with increase in mass flow rate, see table 6.1 for the corresponding hotplate physical system.

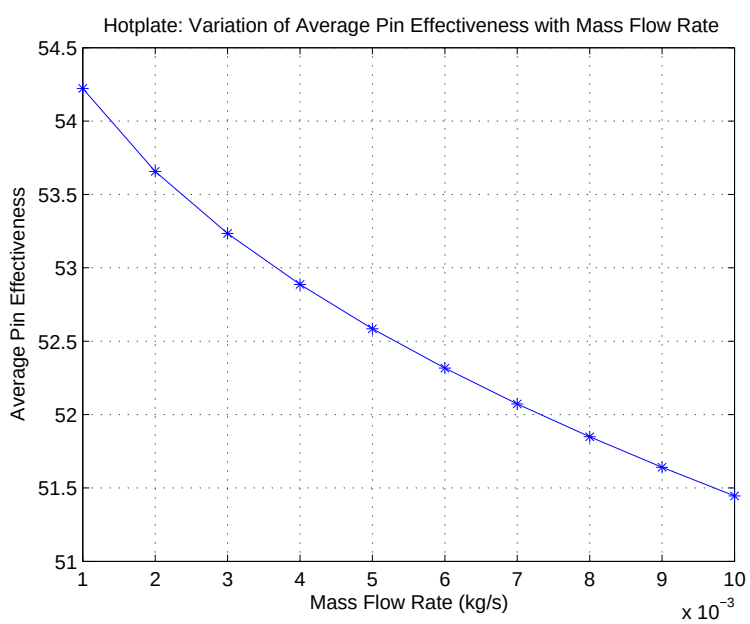

Figure 6.11: Pin effectiveness experiences a slight exponential decrease between the entrance and the exit pins. This plot is based on the average of value of pin effectiveness, see table 6.1 for the corresponding hotplate physical system.

Figures 6.10 and 6.11 show the corresponding variation of pressure drop and pin effectiveness with mass flow rate respectively. Both plots reiterate the point that high values of $\dot{m}$ are not favorable, as they tend to increase pressure drop (and therefore running costs) and decrease the effectiveness/efficiency of the pins.

In the context of the dimensions and values under discussion, a moderate value of mass flow rate within $0.003 \leq \dot{m} \leq 0.005$ kg/s would be sufficient to sustain one hotplate in the nucleate boiling mode and the other in the convection boiling mode. The corresponding pressure drop across the bank of pins is anywhere between 6 and 8 Pa. These findings are now used as guidance to simulate the process of discharging the hot-section (of the packed bed) and simultaneously supplying power to the hotplate.

6.4.3 Power Supply to the Hotplate

We now model a more practical situation in which the packed bed has been charged as described in the previous chapter. The dimensions and parameters are the same as those used in chapter 5. The inlet air temperature to the finned channel is a function of time since it basically depends on the outlet temperature from the thermal storage as the bed discharges. The total pressure drop is the sum of the pressure drop across the packed bed and its counterpart across the finned channel.

The results represented in figures 6.12 show that the high-temperature-heat stored in the bed can sustain nucleate and convection boiling modes for several hours. It is interesting to note that the option where the plates operate in tandem offers ideal conditions for the type of cookery under pursuit in this study. As mentioned earlier, for a typical rural Zimbabwean family, the staple diet cooks well in the nucleate boiling mode for about an hour or so while the accompanying vegetables will cook well by convection boiling in less time.

As can be seen, the first hotplate can last for about 3 hours above the ONB, while the second plate stays within the confines of convection boiling. If heat loss from the storage is minimized, its possible to prepare 2 or 3 moderate meals without need for refilling the storage for this particular case. So in general, proper sizing of the parabolic dish collector combined with sufficiently insulated thermal storage, can sustain cooking for about 2 days in overcast weather. Figure 6.13 belongs to the same package of conditions. It has been included to give an idea of the corresponding (to figure 6.12) power supply to the hotplates as the bed discharges.

Figure 6.14 shows the variation with time of the total pressure drop across the air circuit as the bed discharges. The general trend is a decrease, somewhat exponen-

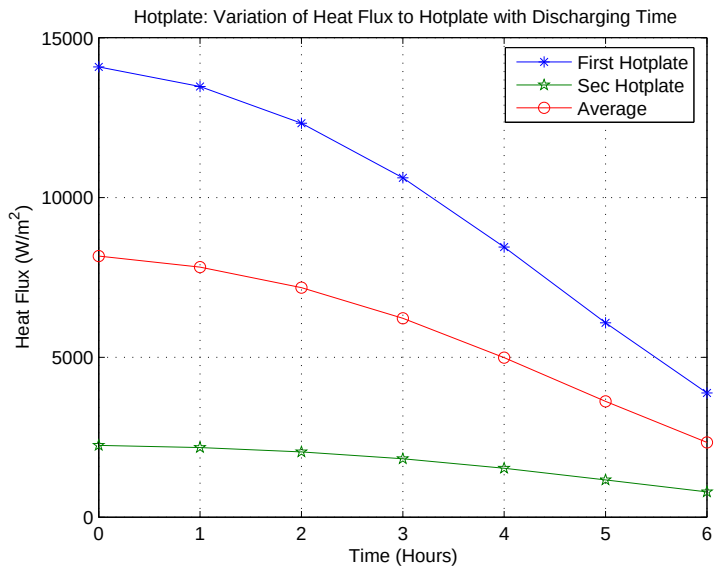

Figure 6.12: These plots show supply of heat flux (to the hotplates) from a bed of the same size and initially charged as depicted in figure 5.12, and then allowed to stay for 12 hours (storage time, see figure 5.15) before subjecting it to continuous discharge for 6 hours. In this case, the mass flow rate is maintained at 0.004 kg/s while tables 5.1 and 6.1 summarize the corresponding rock bed and hotplate physical systems respectively.

tial in this case. As the bed discharges the air density increases while its viscosity decreases. When the behavior of these thermophysical properties of air are applied to equations 5.43 and 6.9, the transient nature of the pressure drop curve becomes obvious.

Of operational importance is to understand what happens to the air temperature as it traverses the packed bed during discharge. The operating set-up is such that the air, after ceding most of its sensible heat to the hotplates, is pumped back to the bottom of the storage. The idea behind air recirculation is to take advantage of the extra sensible energy remaining after the air has been discharged in the finned channel.

Figure 6.15 depicts the variation of the air temperature profile as it moves through the bed during discharge. This analysis belongs to the same package as that referred to for heat flux, power and pressure drop in the previous paragraphs. It is evident that if the outlet temperature of air from the finned channel is higher than that of rock pebbles at the bottom of the bed, the air will start by loosing its energy as it charges this part of the bed. This is obviously not desirable because energy 'left-overs' from the finned channel are therefore of no direct benefit the process of

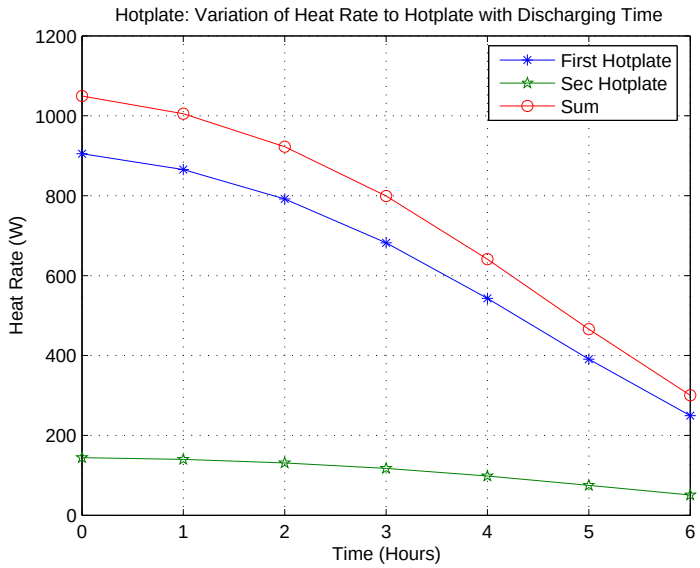

Figure 6.13: These plots show power supply (to the hotplates) from a bed of the same size and initially charged as depicted in figure 5.12, and then allowed to stay for 12 hours (storage time, see figure 5.15) before subjecting it to continuous discharge for 6 hours. In this case, the mass flow rate is maintained at 0.004 kg/s while tables 5.1 and 6.1 summarize the corresponding rock bed and hotplate physical systems respectively.

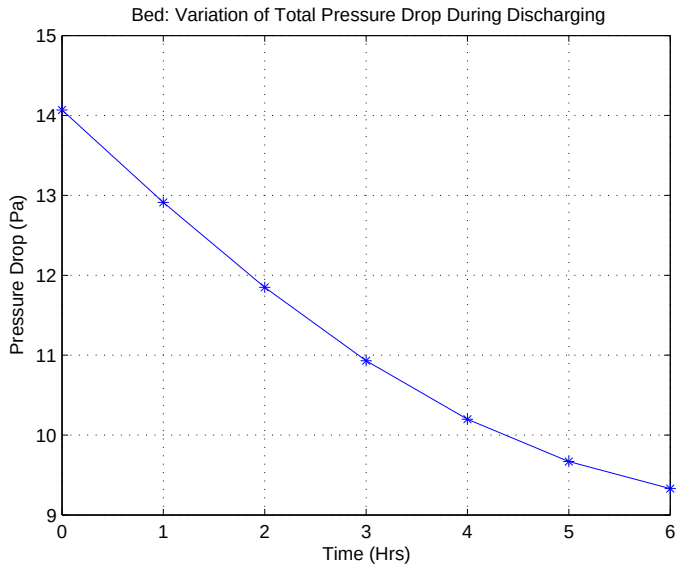

Figure 6.14: This plot illustrates the total pressure drop across the system corresponding to the situation depicted in figure 6.12 in which the 12 hours of storage are allowed before discharge. In this case, the mass flow rate is maintained at 0.004 kg/s while tables 5.1 and 6.1 summarize the corresponding rock bed and hotplate physical systems respectively.

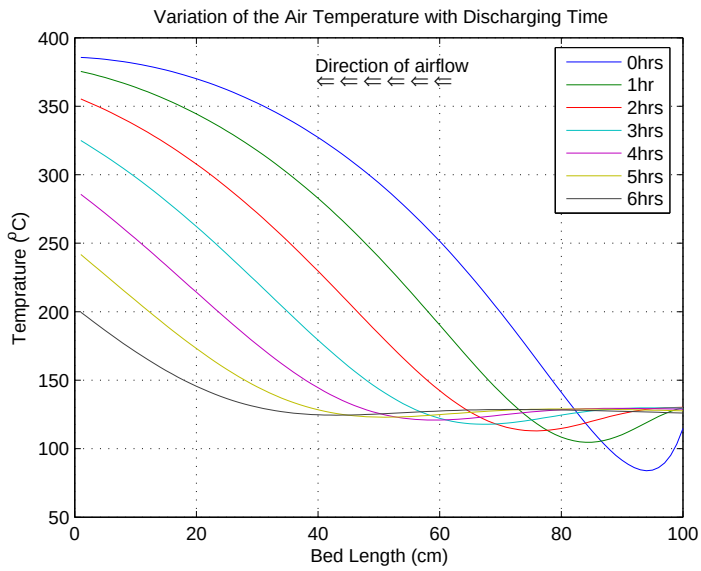

Figure 6.15: The result of circulating air continously for 6 hours, corresponding to the situation depicted in figure 6.12 in which the 12 hours of storage are allowed before discharge. The bed is then subjected to a mass flow rate of 0.004 kg/s. Tables 5.1 and 6.1 summarize the corresponding rock bed and hotplate physical systems respectively.

powering the hotplate.

In simple terms, conditions that compel the air to first discharge and then charge as it circulates through the bed, should be minimized or preferably avoided completely during operation. In essence, the temperature of the rock pebbles at the bottom of the bed should be at least equal to or greater than the temperature of the incoming air from the outlet of the finned channel. Such conditions will facilitate air recirculation to be of direct benefit to the process of supplying power to the hotplates, otherwise it will only achieve the storage of low-temperature-heat at the bottom of the bed.

The anticipated air temperature from a fully charged bed is now shown in figure 6.16. It can be seen that the situation is different from that presented in figure 6.15. In this case, the addition of heat to the air takes advantage of the sensible heat left-overs from the outlet of the finned channel. This implies the prolongation of the period during which high-temperature-heat can be available for cooking.

It is therefore commendable to divide the storage into two compartments, for reference, let's call them the 'hot' and 'not-so-hot' sections of the storage as shown in figure 6.17. The idea is to facilitate the hot-section to be fully charged. This is

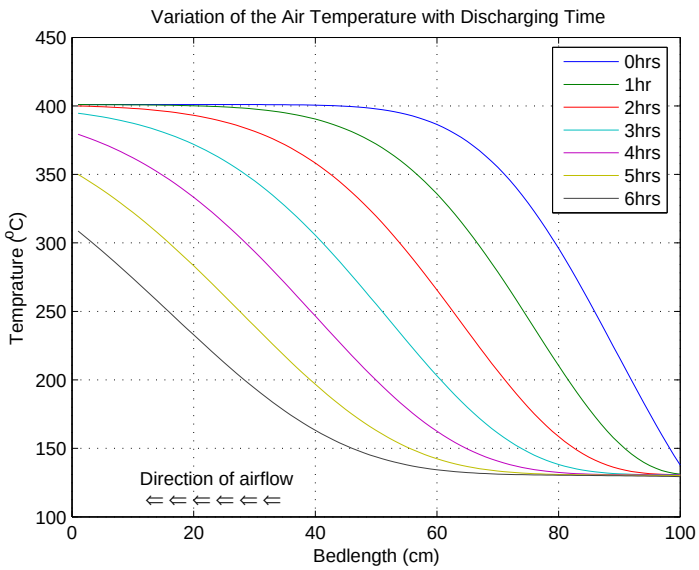

Figure 6.16: Plots showing the air temperature profile that is a result of discharging an adequately charged bed. Unlike what happens in figure 6.15, the air does not discharge before it starts heating-up enough to power the hotplates, see tables 5.1 and 6.1 that summarize the corresponding rock bed and hotplate physical systems respectively. Mass flow rate = 0.004 kg/s.

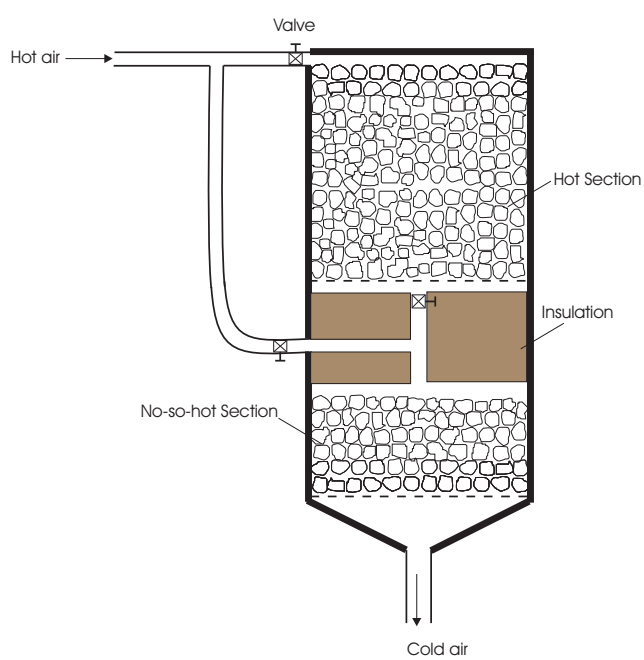

Figure 6.17: A schematic showing a packed bed divided into two compartment. Hot air flowing into or out of either of the beds is controlled by opening or closing the appropriate valve(s).

done to avoid the situation depicted in figure 6.15 where outlet air from the hotplate channel unnecessarily loses its excess heat as it enters the colder bottom of the bed before it starts heating-up again. The main function of the hot-section is therefore to supply high-temperature-heat necessary for the kind of cookery as defined earlier while heat from the second section can be used for low temperature needs like water and space heating.

With a parabolic dish of appropriate size, it is possible to fully charge the hot-section between morning and noon. Any excesses can be allowed to spill over and start charging the second section. The inlet and exit valves of the hot-section can then be closed while the valve to lower section is opened, thereby allowing the charged air to flow directly to the second compartment. This will eliminate unnecessary extra blow power requirements that will arise if the air continues to flow via the already-fully-charged upper section.

6.5 Chapter Summary and Conclusions

This chapter presents the theory and results of modelling hotplates that are powered by discharging high temperature thermal storage. Air is used as the medium for energy transport and transfer from the storage to the hotplates. Modelling shows that the proposed design of a finned air channel on the underside of the hotplates is effective in extracting energy adequate to power the hotplates with only moderate blow power needed.

Simulation results also suggest that it is feasible to have two hotplates operating at different temperatures capable of sustaining nucleate and convection boiling. This is convenient and ideal for the type of fundamental cookery (boiling and pan frying) normally needed by the targeted end-users in this project, i.e, as a first approach to measure the feasibility of this type of solar stove, rural areas located outside the electricity grid in Zimbabwe were initially chosen as the test-field.

Based on the findings of the availability and patterns of beam radiation as discussed in the second chapter, Zimbabwe has enough sunshine resources to sustain thermal energy storage for cookery (as describe in this chapter) sufficing for about 2 to 3 days without need for back up during most parts of the year. Of course, the size of the parabolic dish collector, that of the thermal storage unit, the quality of thermal insulation in terms of the U-value and the load itself, are the major determinants once the energy is available.

References

[1] Holman J.P, 'Heat Transfer', *4th Edition*, 1976.

[2] Incropera F.P. and DeWitt D.P., 'Fundamentals of Heat and Mass Transfer', *5th Edition*, 2002.

[3] Churchill S.W. and Bernstein M., 'Journal of Heat Transfer', vol. 99, 300, 1977.

[4] Rohsenow W.M., 'A Method of Correlating Heat Transfer Data for Surface Boiling Liquids', *Trans. ASME*, vol. 74, 969, 1952.

[5] Zhukauskas A., 'Heat Transfer from Tubes in Cross Flow', *Advances in Heat Transfer*, vol. 8, Academic Press, New York, 1972.

[6] Koşar A., Mishara C. and Peles Y., 'Laminar Flow Across a Bank of Aspect Ratio Micro Pin Fins', Journal of Fluids Engineering, ASME, Vol.127, pp 419-430, 2005.

[7] Lienhard J.H, Dhir V.K and Riherd D.M, 'Peak Pool Boiling Heat Flux Measurements on finite Horizontal Flat Plates', Journal of Heat Transfer, ASME, Vol.95, pp 447, 1973.

[8] Lienhard J.H and Dhir V.K, 'Extended Hydrodynamic Theory of the Peak and Minimum Pool Boiling Heat Fluxes', *NASA-CR-2270*, July 1973.

[9] Farkas B.E, Sigh R.P and Rumsey T.R, 'Modelling Heat and Mass Transfer in Immersion Frying. 1st Model Development', *J. Food Engineering*, Vol. 29, pp 211-226, 1996.

[10] Harry Lawson, 'Food Oils and Fats: Technology, Utilization and Nutrition.', *Chapman & Hall*, 1995.

[11] Cloin J, 'PV on Thatch: A Search for Opportunities of Sustainable Implementation of PV in Manicaland, Zimbabwe', *MSc. Thesis*, ECN-DE Memo-98-069, Eiven University of Technology, 1998.

Chapter 7

Conclusions and Recommendations

7.1 Conclusions

In general, the unavoidable basic energy needs for food preparation is a daily and ever-worsening challenge for the poor folks who live in the rural areas of developing economies (especially Africa), in which case, Zimbabwe was selected for case-studies pertinent to this work. Recurrent drought spells coupled with uncontrolled and continued cutting down of trees over the years, has aggravated the wood-fuel crisis to proportions that are now a major cause of concern almost across the African continent.

Hence, there is need to develop an alternative that will sustainably replace the use of the speedily-diminishing biomass resources. It is in this context that the present research seeks to contribute towards finding a solution by means of small scale solar concentrating systems with heat storage. Basically, the system is expected to function as a solar stove.

In order to asses the potential of the proposed solar stove under typical conditions, a detailed study of the solar radiation patterns over Zimbabwe, based on meteorological data collected between 1980 and 2000, was done. The results in chapter 2 show that Zimbabwe has great potential for solar energy applications, even for direct beam which is of great interest in our case.

Generally, normal-beam irradiation over Zimbabwe can be expected to average between 4 and 10 kWh/m^2 per day. The wet season (Dec-Jan-Feb) values are closer to the lower limit for a greater majority, while the upper limit for the various sites seem to vary from 7 to 10 kWh/m^2, apparently correlated to the sub-region in which the station in question lies. In general, Zimbabwe has good exposure to sunshine, with all parts of the country expected to average between 7 to 10 hours of sunshine from

march to November.

The wet season is usually characterized by intermittent overcast weather, even so, spells of sunny weather can be expected in most parts of the country especially in the western and southern regions. Therefore, it can be said that solar energy resources in Zimbabwe, have the capacity to sustain the type of concentrating systems under discussion, almost throughout the dry season and to some extent, the wet season. All the same, a back-up system (e.g wood-fuel) will be necessary to cater for intermittent overcast weather, usually at the peak of the wet season in January.

The gist of this work involved carrying out a detailed technical simulation to investigate the feasibility of concentrating systems with heat storage that can satisfy high-temperature-heat needs in off-the-grid inhabited areas lying within the Sunbelt, with Zimbabwe having been chosen as the test-case. In essence, the present research is a first approach where the main components of the anticipated solar-stove, with a heat storage facility, have been simulated in detail using MATLAB routines.

It was demonstrated in chapter 3 that; the combination of parabolic dish solar collectors with wide rim-angles ($> 55^o$) and properly sized 3-dimensional volumetric fibrous receivers permit the design of compact solar concentrating systems. Compactness is desirable in regards to safety (during operation), economic and technical reasons. For solar tracking, a clock work device based on the grandfather clock principle, seems to be feasible although an electric motor would be preferable where possible.

The receiver is a 3-dimensional volumetric type made of darkened stainless steel fibres (of diameter 0.1 mm) that can withstand temperatures of up to 1400 ^{o}C. Conical (i.e truncated section of a cone) or slightly modified hemispherical receiver shapes were found to be ideal and compatible with solar concentrating collectors that have wide rim angles. This combination yields to compact designs. The finite-element method was then applied to study what happens inside these type of receivers.

A detailed computer model discussed in chapter 4, which takes into account the heat transfer mechanisms at high temperature within a fibrous volumetric receiver was developed, and then applied to study various aspects, parameters and variables of prime importance that include: absorber efficiency, mass flow rate, the radial and sector-wise temperature profiles for both air and the fibres. In general, the simulation programme yielded valuable insights about volumetric fibrous receivers and shaded more light regarding the major issues of concern for practical considerations in both construction and during operation of such receivers.

It is reasonable to regard the efficiency of the receiver as the overall performance indicator. Under optimal conditions and for the receiver size discussed in chapter 4, a marginal variation in efficiency contained within 75 - 80% was found. As such, this type of receiver has tremendous potential for the production of the anticipated high-temperature-heat ($\simeq$ 400 ^{o}C), even when beam radiation intensity is as moderate as 400 W/m^2. Using the cheap and readily available ambient air, the energy absorbed by the receiver can be extracted by convection, then transported and effectively transferred to a rock bed storage.

Heat storage in rock beds is known technology found to yield satisfactory results for systems involving low-temperature-heat, and has been proposed for use at high temperature. The pertinent heat transfer mechanisms at high temperature as discussed in chapter 5, reveal that the performance of the heat storage system, largely depends on both the quality of the insulation and the extent of thermal degradation.

Evacuated systems, with highly reflective silver foils offer the most effective type of thermal insulation. However, although it is rather bulk, low density rock wool inserted with Al-foils is a much cheaper, albeit competent alternative. Temperature gradients, which lead to thermal degradation, can be minimized by designing the system such that the hot-compartment is almost fully charged by the end of the day. With good insulation, a fully-charged bed, say at 400 ^{o}C, can be stored for about 2 to 3 days and can still meet cooking needs although with a somewhat compromised performance.

Simulations treated in chapter 6 reveal that the proposed design of a finned air channel on the under-side of the hotplates is effective in transferring the energy from the charged air to the hotplates. The power supplied to the hotplates is dependent on the air pump and air temperature. Recirculation of discharged air from the hotplates saves energy and therefore prolongs cooking time.

Depending on system size and design, it is possible to have two hotplates simultaneously operating at different temperatures that support nucleate and convection boiling. For the case of Zimbabwe, and based on the availability of direct beam as discussed in chapter 2, it has been shown that systems that can support cooking for several hours are feasible. For the size and system-design discussed in this work, mass flow rates to order of 0.004 kg/s were found to be suitable while the corresponding pressure drop can be overcome with minimal blow power to the order 5 W or less.

The general conclusion is that: the feasibility of small-scale solar concentrating systems with heat storage, using relatively cheap materials, to meet high-temperature-heat needs for basic food preparation in rural areas (off-the-electricity-grid) in Zim-

babwe is fairly high. Although the benefits of the present project might not mean so much to the western- or urban-dweller, the relative merits of a solar-stove with heat storage are enormous to the ordinary rural folk. A successful system would, in general, upgrade their quality of life. Needless to say is that; a break through will surely revolutionize their struggle in battling the daily challenge of finding the rapidly-dwindling biomass resources to meet their basic high-temperature-heat needs for food preparation.

7.2 Recommendations and Further Work

- In order to maintain constant the inlet air temperature to the storage, the possibility of controlling the mass flow rate by means of a circuit involving direct connection to solar cell such the outcome is principally determined by beam intensity needs to be investigated.

- A detailed technical study that includes experimentation to smoothen the tracking system based the grandfather clock principle requires further work.

- A prototype of the concentrating system needs to be developed: for experimental testing and validation of the models in this work. It will be profitable to separately build and test the major components of the prototype before their incorporation to form the main system.

- The Zimbabwean energy authorities should be made conscient of the vast solar energy resources to their disposal and encouraged to exploit them for both small- and large-scale solar energy projects like: electricity generation, solar cooking, water heating, etc.

- Although Zimbabwe has been regarded as the test-case, the results of a successful system can be extented to all countries that lie within the Sunbelt.

Appendix A

A.1 Estimations of Daily Global Irradiation

This part consists of global irradiation values on a horizontal surface in kWh/m^2 per for the 30 stations covering Zimbabwe.

Estimates of the Monthly Average Daily Global Insolation Over Zimbabwe (kWh/m^2 per day)

Station	**lat**(°)	**lon** (°)	**Jan**	**Feb**	**Mar**	**Apr**	**May**	**Jun**	**Jul**	**Aug**	**Sep**	**Oct**	**Nov**	**Dec**
Gokwe*	−18.0	29.9	6.55	6.50	6.36	6.16	5.38	5.10	5.30	6.19	6.72	7.33	6.76	6.54
Chivhu*	−19.0	30.9	6.36	6.32	5.91	5.42	4.98	4.37	4.61	5.47	6.23	6.50	6.55	6.04
Kwekwe*	−18.9	29.8	6.84	6.84	6.37	6.06	5.45	4.86	5.26	6.04	6.67	7.19	6.73	6.67
Kadoma	−18.3	29.9	6.69	6.28	6.17	6.10	5.51	5.20	5.43	6.17	6.49	7.02	6.62	6.31
Gweru	−19.7	29.9	6.40	6.38	6.26	6.02	5.43	5.06	5.45	5.79	6.73	6.89	6.53	6.42
Chisumbanje*	−20.8	32.3	7.08	6.48	6.15	5.65	5.02	4.27	4.79	5.34	5.93	6.61	6.66	6.72
Makoholi	−19.8	30.8	6.93	6.27	5.81	5.88	5.30	4.90	5.19	5.71	6.32	6.58	6.44	6.50
Matopos	−20.6	28.7	6.58	6.69	6.32	5.67	5.09	4.56	4.69	5.64	6.37	6.39	6.95	6.51
Tsholotsho	−19.8	27.7	6.78	5.76	5.81	5.90	5.17	4.75	5.14	5.74	6.11	6.57	6.19	6.45
Bulawayo	−20.2	28.6	6.13	6.24	5.82	5.58	4.79	4.50	4.77	5.30	5.89	6.32	6.14	6.19
Masvingo	−20.1	30.9	6.66	6.26	6.08	5.82	5.13	4.67	4.69	5.60	6.06	6.47	6.60	6.46
Vic.Falls	−18.1	25.9	6.82	6.62	6.59	6.69	6.13	5.39	5.85	6.54	6.85	7.20	6.93	6.80
WestNic	−21.2	29.4	6.91	6.29	6.03	5.63	4.99	4.41	4.77	5.50	5.99	6.35	6.42	6.61
Buffalo	−21	31.7	7.54	7.36	6.24	5.90	5.59	5.17	5.39	5.77	6.19	6.60	6.90	7.37
Kariba	−16.5	28.9	6.52	6.20	6.22	6.27	5.73	5.20	5.54	6.25	6.52	7.28	7.00	6.59
Hwange	−18.6	27.0	6.63	6.50	6.47	6.31	5.52	5.24	5.41	6.38	6.93	7.38	7.01	6.71
Binga	−17.7	27.4	6.80	6.91	6.88	6.67	5.92	5.65	5.74	6.50	7.07	7.47	7.30	7.22
Beitbridge	−22.1	30.0	7.18	6.78	6.32	5.97	5.33	4.57	4.69	5.61	6.10	6.74	6.83	7.61

Table 7.1: Locations with data derived from sunshine hours are marked with an asteric(*), while the rest have records from pyranometer measurements. These averages are based on meteorolgical data recorded between 1981 and 2000 at thirty stations across Zimbabwe. **lat**, **lon**, **WestNic** and **Vic.Falls** are shortcuts for latitude, longitude, West-Nicholson and Victoria-Falls respectively.

Estimates of the Monthly Average Daily Global Insolation Over Zimbabwe (kWh/m^2 per day)

Station	**lat**(°)	**lon** (°)	**Jan**	**Feb**	**Mar**	**Apr**	**May**	**Jun**	**Jul**	**Aug**	**Sep**	**Oct**	**Nov**	**Dec**
Rusape*	−18.7	32.4	6.23	6.00	5.71	5.37	5.19	4.82	5.10	5.74	6.61	6.94	6.81	5.95
Chisengu*	−19.9	32.9	6.74	6.46	5.90	5.12	4.74	4.10	4.49	5.30	6.04	6.60	6.74	6.54
Chipinge*	−20.0	32.6	6.91	6.40	6.18	5.88	5.25	4.43	4.85	5.59	6.20	6.84	6.71	6.66
Nyanga	−18.4	32.7	6.18	6.32	6.25	6.00	5.27	4.97	5.20	5.96	6.55	6.67	6.32	5.77
Mukandi	−18.7	32.9	6.09	5.99	5.80	5.61	5.34	4.67	4.84	5.78	6.35	6.52	6.27	5.96
Mutare	−19.0	32.7	6.74	5.98	6.05	5.76	5.16	4.53	4.83	5.79	6.28	6.79	6.52	6.26
Karoi	−16.8	29.6	6.28	6.19	6.10	6.17	5.74	5.24	5.66	6.37	6.70	7.08	6.70	6.16
Banket*	−17.3	30.4	6.52	6.63	6.21	5.76	5.23	4.51	4.99	5.91	6.67	6.96	6.95	6.43
Harare	−17.8	31.1	5.78	5.91	5.72	5.46	4.92	4.62	4.94	5.55	6.23	6.55	6.14	5.83
Marondera	−18.3	31.5	6.35	6.04	5.97	5.90	5.37	4.89	5.31	5.97	6.30	6.57	6.32	6.19
Henderson*	−17.6	31.0	5.86	5.68	5.75	5.53	4.90	4.58	4.75	5.66	6.23	6.79	6.17	5.98
MtDarwin	−16.8	31.7	6.59	6.13	6.26	6.02	5.49	4.98	5.28	5.98	6.37	6.83	6.64	6.35

Table 7.2: Locations with data derived from sunshine hours are marked with an asteric(*), while the rest have records from pyranometer measurements. These averages are based on meteorolgical data recorded between 1981 and 2000 at thirty stations across Zimbabwe. In the 2nd and 3rd columns, **lat** and **lon** are shortcuts for latitude and longitude respectively.

Appendix B

B.1 Extrapolation of the Thermophysical Properties of Air

The following plots show how the thermophysical properties have been extrapolated for use in the modeling programmes. This was achieved by plotting data available in heat transfer texts (The Fundamentals of Heat and Mass transfer by Incropera and DeWitt) and then use the *polynomial curve fitting tool* in MATLAB to generate the desired poly-fits. In all cases for the polynomials shown on each plot, the independent variable x represents the air temperature.

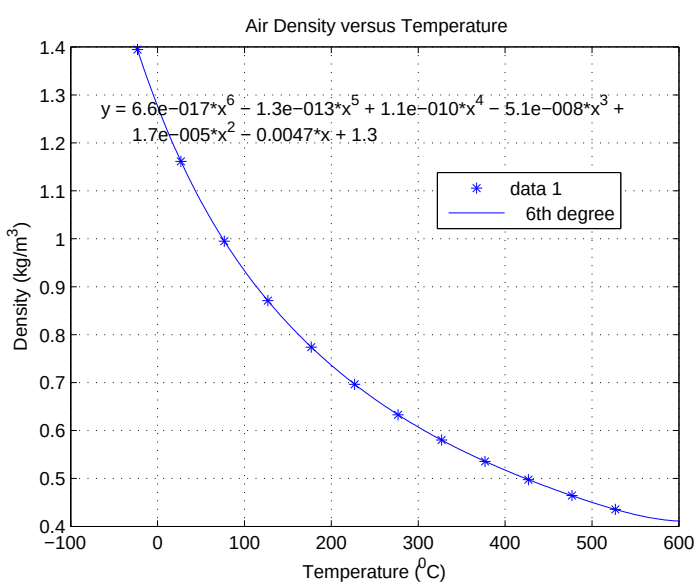

Figure 7.1: Plot illustrating a poly fit that simulates the variation of air density with temperature was generated. This is essentially an alternative to $\rho = \rho_o \frac{T_o}{T}$. For the polynomial shown on the plot, the dependent variable y represents air density.

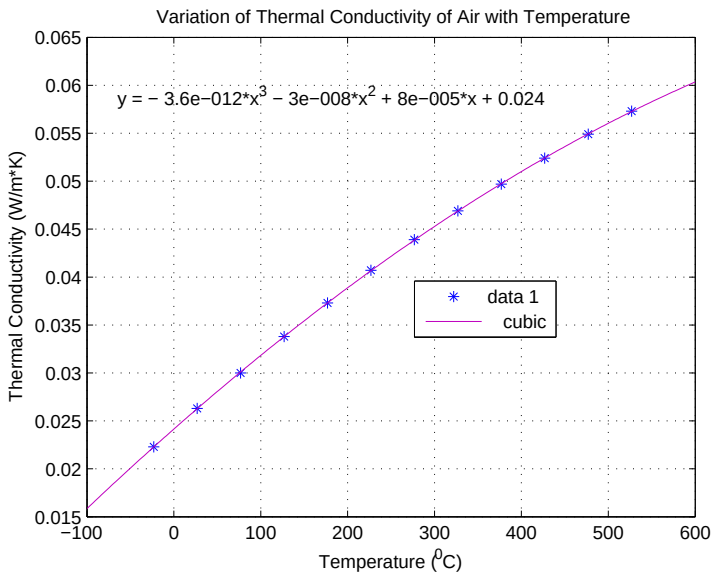

Figure 7.2: Regarding the polynomial shown on the plot, the dependent variable y represents the thermal conductivity of air.

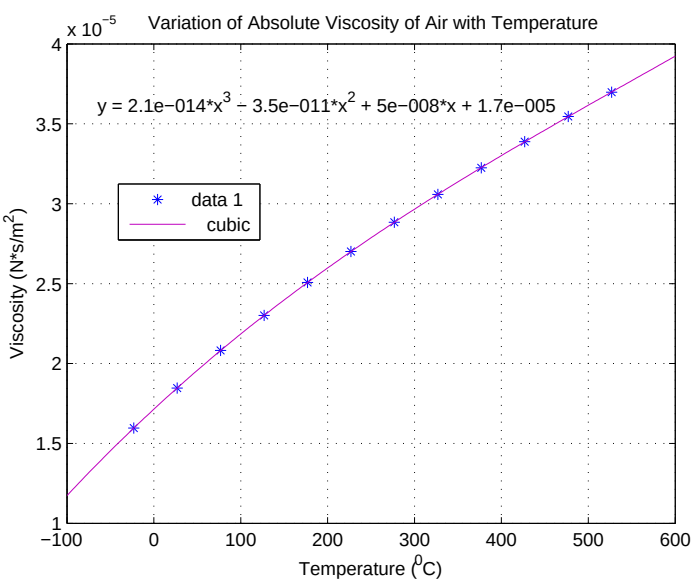

Figure 7.3: Regarding the polynomial shown on the plot, the dependent variable y represents the absolute viscosity of air.

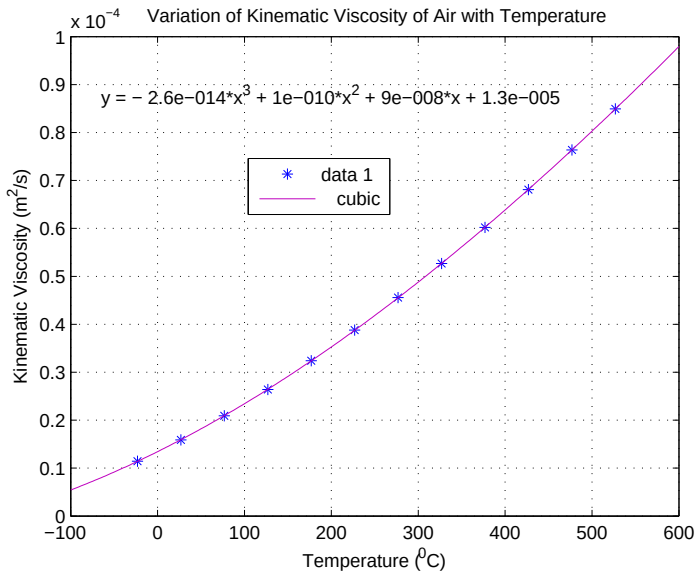

Figure 7.4: Regarding the polynomial shown on the plot, the dependent variable y represents the kinematic viscosity of air.

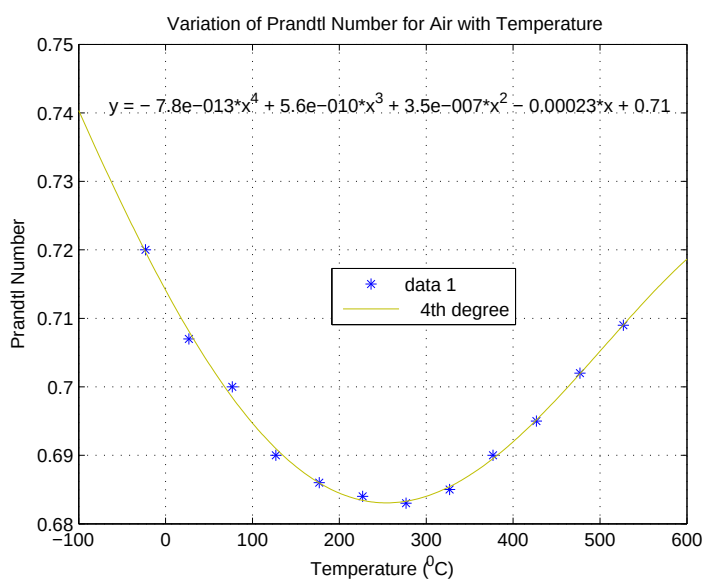

Figure 7.5: Regarding the polynomial shown on the plot, the dependent variable y represents the Prandtl number of air.

B.2 Miscellaneous Information

This section contains miscellaneous information that might be necessary (for a quick reference) to understand some sections of the main text.

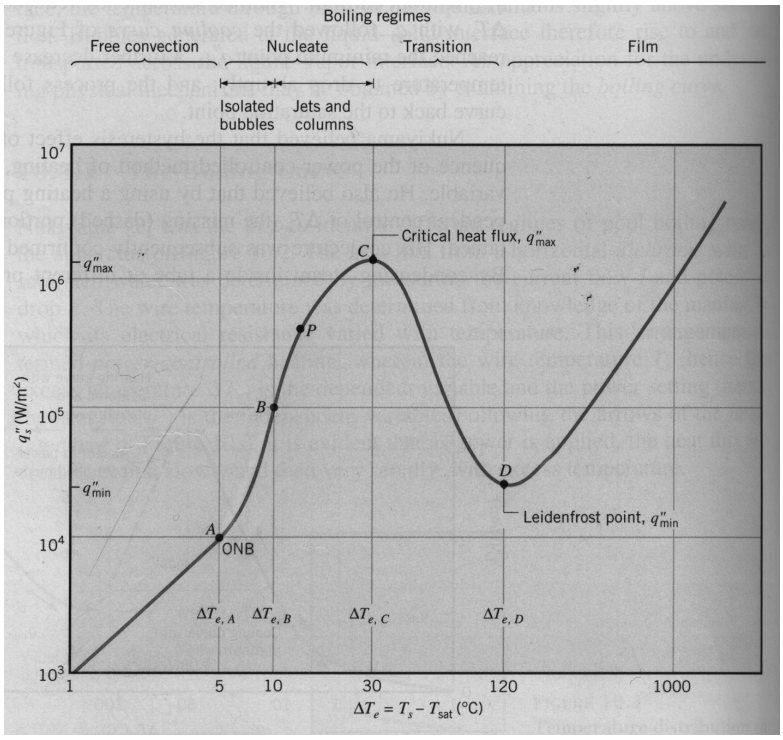

Figure 7.6: Typical Boiling curve for water at 1 atm : surface heat flux q''_s as a function of excess temperature. ONB on point A stands for the 'Onset of Nucleate Boiling'. Adapted from [31]

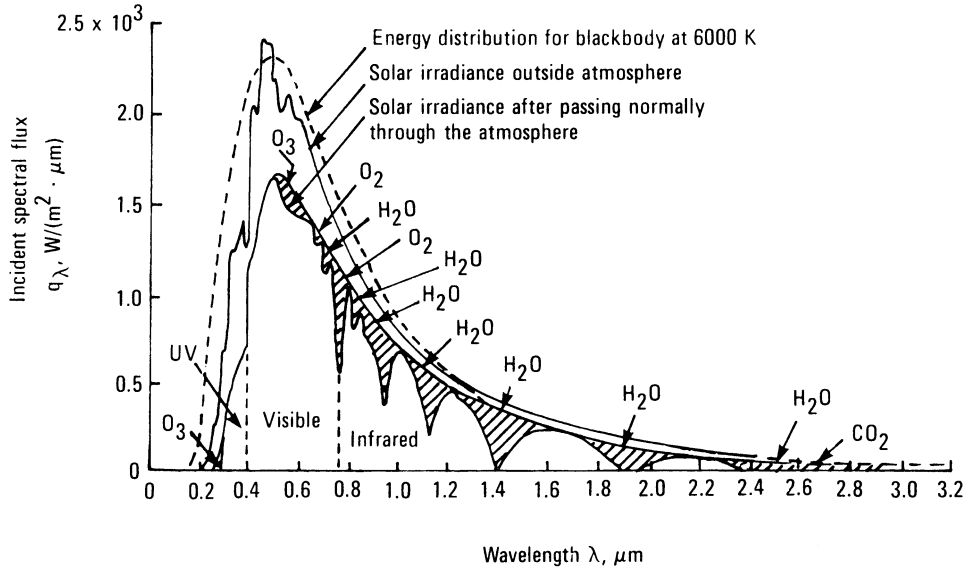

Figure 7.7: Spectral irradiance curves for direct sunlight extra terrestrially and at sea level with the sun directly overhead, airmass 1. Shaded areas indicate absorption due to atmospheric constituents, mainly H_2O, CO_2 and O_3. Adapted from [4]

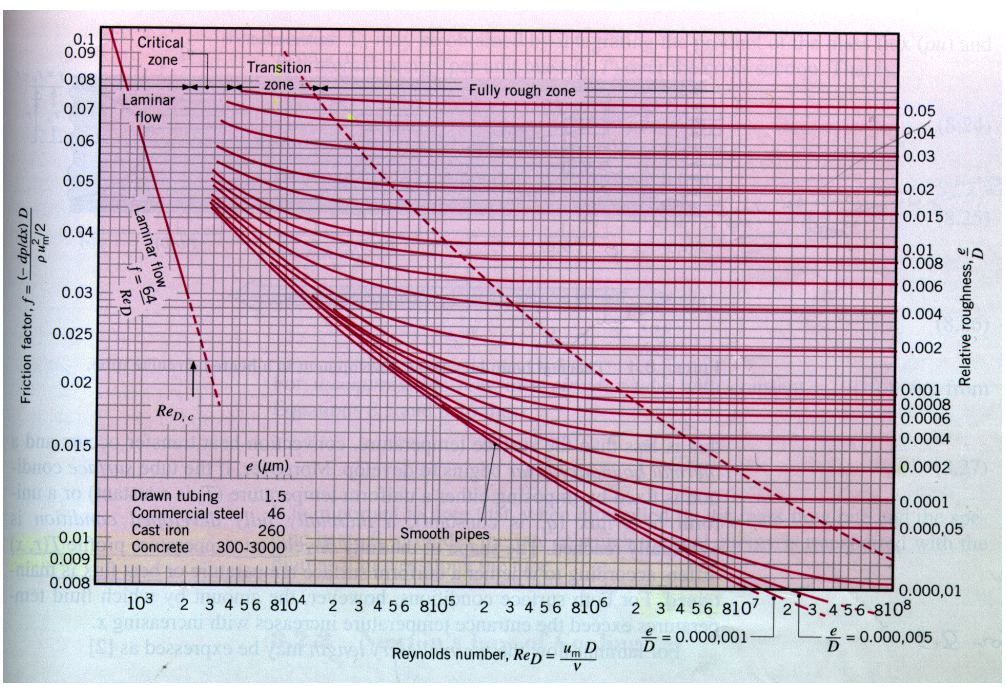

Figure 7.8: The Moody Chart: Friction factor as a function of the Reynolds number and surface roughness for round pipes. Adapted from [31].